Structural, electronic and magnetic properties of ultrathin epitaxial manganese films

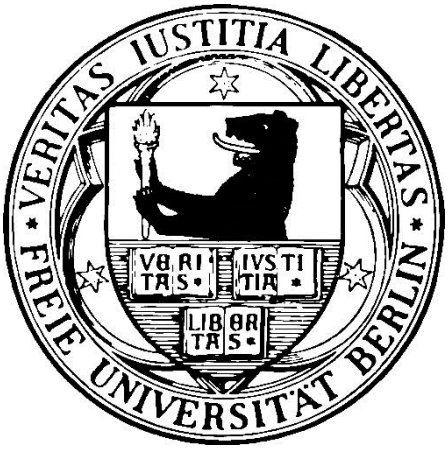

Doctoral thesis of Jiaming Song

submitted to the

Department of Physics

of

Freie Universität Berlin

25. 08. 2015

This work was completed in Prof. Dr. Wolfgang Kuch's research group at the Physics Department of Freie Universität Berlin.

First Supervisor: Prof. Dr. Wolfgang Kuch

Second Supervisor: Prof. Dr. Leonhard Grill

Date of Submission: 25. 08. 2015

Date of Disputation: 24. 09. 2015

Kurzfassung

Diese Arbeit befasst sich mit niederdimensionalen Materialien, im Speziellen mit ultradünnen Mn-Filmen und Graphen auf metallischen Substraten. Mittels Rastertunnelmikroskopie (STM) wurden die Oberflächenstruktur sowie die elektronischen und magnetischen Eigenschaften bei Raumtemperatur unter Benutzung von ringförmigen ferromagnetischen massiven Eisensonden, die eine magnetische Empfindlichkeit in der Ebene bieten, untersucht.

Die Oberfläche von wenige Atomlagen dicken antiferromagnetischen Mn-Filmen mit einer tetragonal expandierten flächenzentrierten Struktur auf Co/Cu(001) weist auf der Submikrometerskala einen rastertunnelspektroskopischen Kontrast der ortsaufgelösten differentiellen Leitfähigkeit auf. Es konnte gezeigt werden, dass der Hauptbeitrag zu dieser auf größerer Längenskala auftretenden lagenweisen Modulation des Kontrasts in Abhängigkeit von der Mn-Schichtdicke nicht spinpolarisiertes Tunneln aus einer lagenweisen antiferromagnetischen Spinanordnung, sondern eine lagenabhängige elektronischen Eigenschaft des Mn-Films, die auf Grund unterschiedlicher Co-Konzentration auftritt, ist. Auf atomarer Skala bildet sich eine strukturelle Rekonstruktion aus, die eine (12×2)-Periodizität und eine scheinbare Oberflächenkorrugation von bis zu 0.3 Å in zwei zueinander orthogonalen Domänen auf dem vierfach symmetrischen Substrat aufweist. Gleichzeitig aufgenommene Bilder der differentiellen Leitfähigkeit zeigen eine unterschiedliche Textur innerhalb der zwei orthogonalen Domänen, was auf eine Nichtkollinearität der Spinanordnung der Mn-Oberfläche schließen lässt. Diese Nichtkollinearität wird auf miteinander konkurrierende Austauschwechselwirkungen zwischen den Mn-Atomen in der magnetisch frustrierten und rekonstruierten Schichtstruktur zurückgeführt.

Bei Submonolagen-Bedeckungen von Mn bilden sich auf Cu(001) zweidimensionale (2D) Legierungsphasen auf der Oberfläche. Bei Abscheidung bei Raumtemperatur tritt bei Bedeckung von mehr als 1 Monolage (ML) ein Lagen-plus-Inselwachstum auf. 2D-Strukturen lassen sich in dickeren Mn-Schichten auf Cu(001) effizient durch Veränderung der Grenzfläche mit durch Sauerstoffadsorption hervorgerufener „missing-row“-Rekonstruktion oder durch Nano-Modifikation mit Co-Inseln erzielen. Für Mn/Ni(111) wurde lagenweises Wachstum des Mn-Films bei Raumtemperatur beobachtet. Unterhalb von 200 K weist 1 ML Mn/Ni(111) eine metastabile Gitterverzerrung auf. Die detaillierte Struktur von 8 ML dicker Mn-Filme, die unterhalb von 200 K abgeschieden wurden, wird sowohl auf Ni(111) als auch auf Cu(001) ebenfalls gezeigt.

Das Wachstum von Graphen (Gr) auf Ni(111) weist zwischen 800 K und 900 K sowohl (1×1)-epitaktische als auch rotierte Phasen auf. Abhängig von der Kohlenstoffkonzentration im Substrat führt die verglichen mit (1×1) Gr relativ schwache Bindung zwischen rotiertem Gr und Ni(111) entweder zur Bildung von Ni_2C oder einer weiteren Lage Gr, die unterhalb der ursprünglichen liegt. Das rotierte Gr wurde sowohl hinsichtlich der Bias-Abhängigkeit der Amplitude der Übergitter-Korrugation, der Ni_2C-induzierten elektronischen Modifikationen des Gr, als auch des Einflusses von Sauerstoff auf das Gr-bedeckte Ni_2C im Detail untersucht. Des Weiteren wird eine Rastertunnelspektroskopie-Untersuchung der auf der Gr/Ni_2C-Oberfläche abgeschiedenen Sub-ML Mn gezeigt.

Abstract

This thesis focuses on low-dimensional materials, namely ultrathin Mn films and graphene, on metallic substrates. Their surface structure as well as electronic and magnetic properties were investigated by scanning tunneling microscopy (STM) using a ferromagnetic ring-shaped bulk iron probe with in-plane magnetic sensitivity at room temperature.

The surface of a few atomic monolayer thick antiferromagnetic Mn films with expanded face-centered tetragonal structure on Co/Cu(001) exhibits a submicrometer-scale layerwise contrast in scanning tunneling spectroscopy (STS) differential conductance maps. The main contribution to this large-scale layerwise modulation of contrast observed as a function of Mn thickness proves to be not spin-polarized tunneling from a layered antiferromagnetic spin alignment, but layer-dependent electronic properties of the Mn film due to different levels of intermixing with Co atoms. On the atomic scale, a geometrical reconstruction with a (12×2) periodicity and an apparent surface corrugation of up to 0.3 Å exists in two orthogonal domains on the fourfold-symmetric substrate. Simultaneously recorded differential conductance maps show different textures in the two orthogonal domains, demonstrating noncollinearity in the Mn surface spin structure. This noncollinearity is attributed to competing Mn–Mn interatomic exchange interactions in the magnetically frustrated and reconstructed film structures.

In the Mn/Cu(001) system, two-dimensional (2D) alloying phases are present at surfaces with sub-monolayer (ML) coverage of Mn. A layer-plus-island growth mode is favored at coverages above 1 ML during room-temperature deposition. Effective ways to achieve a 2D structure for thicker Mn films on Cu(001) are modifying the interface by creating a "missing-row"-reconstruction by oxygen or by nano-seeding Co islands. In the Mn/Ni(111) system, a layer-by-layer growth of the Mn film was observed at room temperature. A metastable lattice distortion exists in 1 ML Mn/Ni(111) below 200 K. On both Ni(111) and Cu(001), the detailed structure of Mn films of 8 ML thickness deposited below 200 K is also investigated.

The growth of graphene (Gr) on Ni(111) between 800 K and 900 K exhibits both (1×1)-epitaxial and rotated phases. Compared to (1×1) Gr, the relatively weaker bonding between the rotated Gr and Ni(111) leads to the formation of either Ni_2C or another Gr layer underneath, depending on the bulk carbon concentration of the substrate. The rotated Gr has been studied in detail in terms of bias dependence of the amplitude of Gr superlattice corrugations, the Ni_2C-induced electronic property modification of Gr, as well as the oxygen influence of the Gr-covered Ni_2C. An STS study of sub-ML Mn deposited on the Gr/Ni_2C surface is also presented.

Contents

1 Introduction

The thin film industry plays an important role and has a very broad impact on our everyday life. It is never exaggerated to say that thin films have been revolutionizing the world. A thin film refers to a layer of material with a thickness ranging from nanometer to several micrometers. It is quite common to touch the thin-film-coating technique everywhere, like the household glass mirror, self-cleaning glass in skyscrapers, metalized films for food packaging and NASA's spacesuits, anti-reflective coating on eyeglass lenses, or a music CD with a shiny reflective side.

Among these wide-range applications, thin films in modern magnetic data storage have drawn great attention since the discovery of the giant magnetoresistance (GMR) by Albert Fert and Peter Grünberg in 1988 [1,2]. The GMR effect is the phenomenon that the electrical resistance changes significantly with the parallel or antiparallel magnetization alignment of adjacent ferromagnetic (FM) layers. The overall resistance is low for parallel alignment and high in the antiparallel case. This revolutionary discovery lead to the birth of spintronics, a portmanteau meaning of spinelectronics, in which spins are manipulated by both magnetic and electrical fields. The most common utilization of GMR is in the spin valve structures, which are layered structures with layers of only a few nanometer thickness and consist of a free magnetic layer, a conducting spacer layer, and another magnetic layer pinned by an antiferromagnet. In a spin valve structure, spin-polarized electrons undergo a spin-dependent scattering process at interfaces and within the bulk of the FM layers. The pinning of the pinned layers in most spin valves depends on the exchange anisotropy [3] which is the interaction between a ferromagnet and an adjacent antiferromagnet. Spins in the FM layer can be pinned by spins with an antiferromagnetic (AFM) arrangement, but the phenomenon is still poorly understood. Accordingly, the interface between a ferro- and AFM layers has been attracting lots of researchers to explore [4–6]. After the discovery of GMR, the spin transfer torque (STT) subsequently discovered by Slonczewski [7] and

Berger [8] gave a new impetus to the development of spintronics and lead to the new generation of high-speed spintronic devices only controlled by current [9]. In real applications, to have a reliable and stable pinning effect, the requirements for an AFM material are that the exchange field associated with the effect be large (> 500 Oe), that the blocking temperature be high (> 200 ℃), and that the effect remain strong over long times (> 10 years) [10].

Up to date, the conventional FM spintronics has been widely studied [11–13], however, an increasing interest on AFM spintronics is arising these days [14]. The application of antiferromagnets is more advantageous than ferromagnets [14]. Firstly, antiferromagnets do not create stray field and weakly interact with each other. Secondly, the characteristic resonance frequencies between different AFM states are sevearal orders of magnitude higher than those of typical ferromagnets, which facilitates the operation of high-speed devices in the terahertz range rather than in the gigahertz range as for ferromagnets. Thirdly, in semiconductors the AFM ordering exists more often than FM ordering, and thus makes highly sensitive and low-energy consuming spintronic devices possible.

Although AFM materials are widely used in spintronic applications, their actual spin arrangement is still poorly understood because the zero net magnetic moment makes it difficult to measure. Scientists attempted to study the AFM spin configuration by utilizing the exchange coupling between FM and AFM layers, as introduced in section 3.1. Nevertheless, these previous indirect observations still lack a direct proof. Chapter 3 aims to further reveal the surface spin configuration of AFM Mn thin films pinned by FM Co layers and to supply direct real-space observation of AFM spin texture by using high-resolution spin-polarized scanning tunneling microscopy.

Technically, the tremendous magnetic information technology industry advances the research in magnetism at surfaces/interfaces and in the thin films. The local environment at a surface/interface or in a thin film, such as symmetry, the number and the type of nearest-neighbor atoms, the lattice parameters, can have drastic influence on the magnetic properties (e.g., magnetic moment, critical temperature, magnetic anisotropy, magnetoelastic coupling, etc.). Thus the quality of magnetic thin films becomes a first important issue. Molecular beam epitaxy (MBE) enables high-quality epitaxial crystalline magnetic thin films and well-defined surfaces/interfaces. Epitaxial ultrathin Mn films on a

nonmagnetic Cu(001) and a FM Ni(111) substrate are investigated in chapter 4 and chapter 5, respectively, with respect to film structure and growth mode.

Low-dimensional materials demonstrate unique properties influenced by the quantum size effect. One of the most representative materials is the 2D single-atomic-carbon-layer crystal, graphene, with a honey-comb lattice. The name of "graphene" was given in 1994 by Hanns-Peter Boehm who described this single-layer carbon foil in "Zeitschrift für anorganische und allgemeine Chemie" in 1962 [15]. Graphene is not a mysterious thing that only exist in scientific labs. Using a pencil and simply draw some lines on a piece of paper, a few atomic-layer-thick graphite or even graphene may be created unconciously. Until 2003, Andre Geim and Konstantin Novoselov isolated this one atomic thick layer from bulk graphite successfully by a scotch tape technique (mechanical exfoliation) [16] and broke the presumption that 2D materials cannot exist due to the thermal instability [17,18]. Their success is another revolutionary anchor for modern nanotechnology and has triggered the era of 2D crystals, e.g. 2D allotropes (graphene, graphyne, germanene, silicene, phosphorene), transition metal dichalcogenides ($NbSe_2$, $TaSe_2$, WSe_2, MoS_2, TaS_2), hexagonal boron nitride, etc.

In the past decade, graphene has attracted great attention because of its extraordinary properties. Its mechanical strength is more than 100 times stronger than steels of one atomic layer thickness [19]. It is nearly transparent for heat and electricity [20]. Very high transmittance [21] makes graphene a promising alternative choice for silicon or ITO in photovoltaic industry. Due to its extremely small spin-orbit interaction and almost zero nuclear magnetic moments (hyperfine interaction) in carbon atoms, room-temperature spin current injection and detection become possible in graphene, which enables such material to be an excellent candidate for spin qubits and opens a door of the quantum computing. Graphene-based spintronics has a great potential in spintronic device applications and is becoming more and more attractive [22–26]. Spin-filtering at the interface between graphite and close-packed fcc Ni(111) or hcp Co(0001) has been predicted by Karpan et. al [23,27]. The spin-valve effect for a FM transition metal in contact with Gr has also been reported [28–30]. Moreover, besides the 2D sheet, graphene can be wrapped up into 0D buckyballs, rolled into 2D nanotubes, or stacked into 3D graphites [31]. Each different form outstretches diverse properties and thus applications. All in all, graphene is becoming more

and more important and permeating various aspects in our lives, as Andre Geim said, “graphene is not a fleeting fashion but is here to stay” [31].

There are several ways for graphene preparation. Besides the exfoliation technique, chemical vapor deposition is another important method, in which a substrate is necessary. In order to minimize the lattice mismatch and have a reactive surface for carbon-containing precursor molecules, Ni(111) is chosen for graphene deposition. As introduced in sections 6.1, 6.2, and 6.3, the preparation condition influences the graphene quality greatly on Ni(111). On Ni(111), graphene can be tightly adsorbed on the metal substrate, or can exhibit weaker bonding and form superlattices due to rotation by a few degrees. The rotated graphene in chapter 6 is the main issue of intest because it exhibits diverse structural and electronic properties. The highlights of this chapter are about nickel-carbide-induced electronic property modifications of rotated graphene in sections 6.4 and 6.5, which have not been deeply explored before.

In the body of this thesis, the following chapters are included:

Chapter 2 illustrates the theoretical background of thin film growth, magnetic properties and relevant characterization techniques.

Chapter 3 discusses electronic and magnetic properties of AFM Mn films on Co/Cu(001).

Chapter 4 and 5 are about Mn epitaxy on Cu(001) and Ni(111) substrates, respectively.

Chapter 6 focuses on the growth of ultrahigh-vacuum-deposited graphene on Ni(111) and its diverse structural and electronic properties investigated by scanning tunneling microscopy and spectroscopy.

Chapter 7 summarizes the main conclusions of the above chapters.

2 Theoretical background and experimental details

2.1 Surfaces and interfaces of thin films

In solid state physics, an interface refers to a few atomic layers between two solids that contact with each other intimately. A solid surface is a type of interface which could be surrounded with either atmosphere or vacuum. Differently from atomic physics, a solid surface or interface focuses on a vast number of atoms with high condensation which could be about 10^{15} cm^{-2} atoms in the topmost layer of a surface. On a solid-crystalline surface, due to the broken-infinite-translational symmetry, the properties of the few atomic layers differ from the bulk crystal that initially treated assuming infinite extension. When probes, e.g. low-energy electrons, atomic or molecular beams, with strong interaction with solid matter are used, the penetration depth into the solid could be only a few atomic layers. Thus, technically, the probed properties of the surface atomic layers differ greatly from the bulk material. Besides the technique-related properties of surfaces and interfaces, the properties of a solid thin film on a substrate also differ from the bulk because the thin-film system contains one solid-solid interface and one surface. The properties of a thin film are thus determined by the properties of the two interfaces and the bulk solid-state-physics concepts no longer apply to such a system [32]. Due to the quantum-size effect in the direction perpendicular to the surface, the thin-film system demonstrates various unique properties compared to the bulk [33,34]. The surface and interface of a solid thin film on substrate thus become interesting targets for studies.

2.2 Growth of thin films

Morphology and structure are two concepts that are often used in the description of thin-film surface or interfaces. Morphology is a macroscopic concept for describing the form or

shape which depends on the type of property being considered and on the resolution of the technique used for its observation [32]. Structure, on the other hand, is connected to a microscopic, atomic picture and is devoted to the detailed geometrical arrangement of atoms and their relative positions [32]. The atomic structure influences significantly the morphology of an interface or a surface. The corresponding properties of thin films could be modified by the surface and interface structures and thus controlling the growth of thin films on substrates is very important in modern surface nanotechnology [6,35].

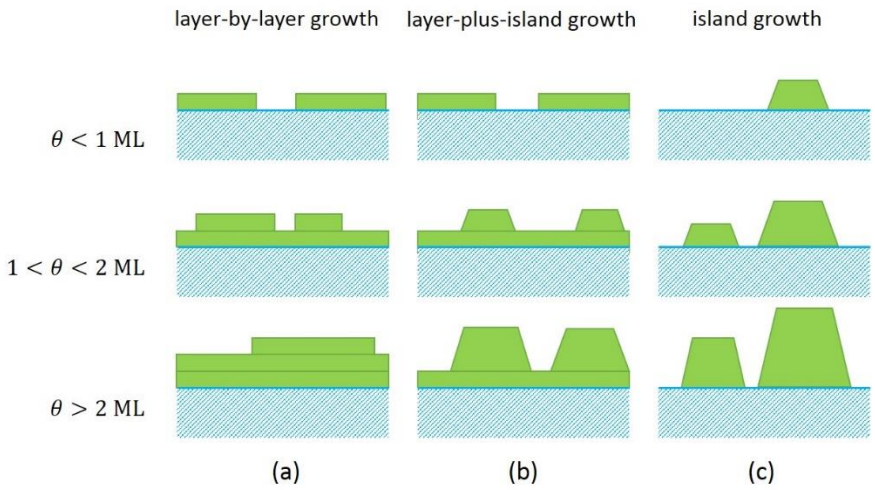

Figure 2-1 From Ref. [32]. A sketch of three main growth modes for thin films at different coverages (θ). ML is the abbreviation of monolayer. (a), (b), (c) show layer-by-layer growth, layer-plus-island growth and island growth, respectively.

In thermodynamic equilibrium, all processes in two opposite directions are proceeded equally, e.g., condensation and re-evaporation, decay and formation of clusters must have the same rate, such that there is no net growth of a film [32]. In order to form a thin film on a substrate, a non-equilibrium kinetic process during the growth is required. To consider the thin-film growth phenomenologically, three types of growth mode are shown in Figure 2-1. In the layer-by-layer growth mode (Frank-van der Merve, FM), a new layers start to grow after the completion of the last one and a 2D growth of the film with smooth surfaces is favored. In contrast, the island-growth mode (Vollmer-Weber, VW) proceeds by forming nucleation, island, and merger of islands, giving rise to rough surfaces. The layer-plus-island growth (Stransky-Krastanov, SK) mode is between the two extremes mentioned

above. The film atoms firstly forms one or a few complete layers and then switches to island growth.

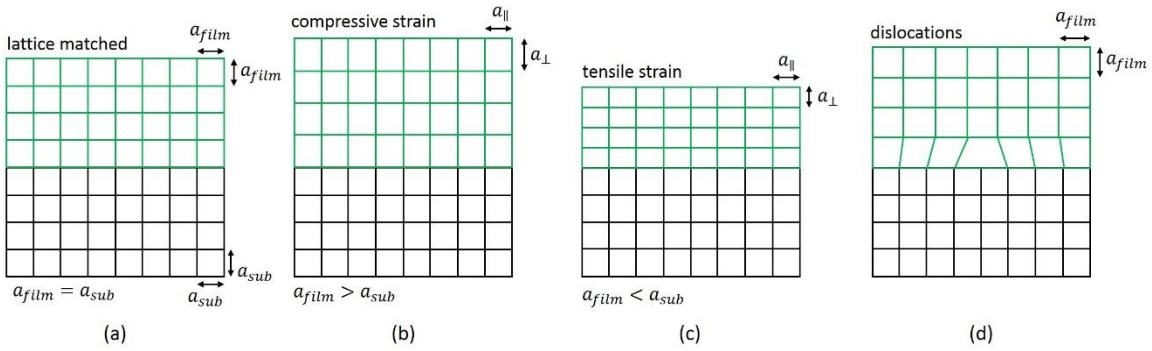

Figure 2-2 Film deposited on a substrate in the epitaxy (a), (b), (c) and dislocation (d) cases. Green and black grids represent the film and substrate lattices, respectively.

A freshly prepared clean surface is quite reactive towards particles, atoms, and molecules. To achieve a well-defined clean surface and avoid contaminations, ultrahigh vacuum is required for thin-film preparations.

To epitaxially grow a film on a crystalline substrate, a perfect lattice match as shown in Figure 2-2 (a) is difficult to achieve for two different materials. In most cases, a slight lattice mismatch may exist in thin-film systems. As Figure 2-2 (b) and (c) show, when the film lattice parameter is larger than the substrate, a compressive strain will be present in the film, otherwise, a tensile strain will occur. As the film thickness increases to a certain degree, the film can no longer be strained to fit the substrate and will get relaxed, introducing inevitable dislocations due to the physical mismatch of terminating bonds at the interface, which is schematically shown in Figure 2-2 (d).

2.3 A novel single atomic layer film: Graphene

Graphene is a unique film composed of a single atomic layer of carbon in a 2D-honeycomb lattice. In such a lattice, each carbon atom has four bonds, three σ bonds (a combination of s, p_x and p_y orbitals) hybridizing with three neighbors (sp^2 hybridization) and one π bond (p_x orbital with an out-of-plane orientation). The unit cell of the graphene 2D lattice consists of two carbon atoms and the lattice constant is 1.42 Å. The hexagonal shaped graphene 2D lattice can be considered as two nonequivalent interleaving triangular sublattices, as shown

in Figure 2-3 (a). In the band structure of graphene illustrated in Figure 2-3 (b), the conduction and valence bands meet at the Dirac points which are on the edge of the Brillouin zone in the momentum space, making graphene a zero-gap semiconductor. Two nonequivalent sets of three Dirac points are present in the Brillouin zone, as marked with K and K' which are primary points of interests for studying the electronic properties of graphene. Compared with graphene, the primary point of interest in traditional semiconductors is generally Γ point where the electron momentum vanishes. In the regions near one of the Dirac point, the electronic band exhibits a cone-like linear dispersion and the Fermi energy of an ideally freestanding graphene is at the Dirac energy. Such linear dispersion can be describes by the Dirac equation for massless fermions. At the Dirac point, the effective mass for electrons becomes zero and the Fermi velocity v_F reaches about 10^6 m/s, which makes charge carriers in graphene behaves like relativistic particles with an effective speed of light.

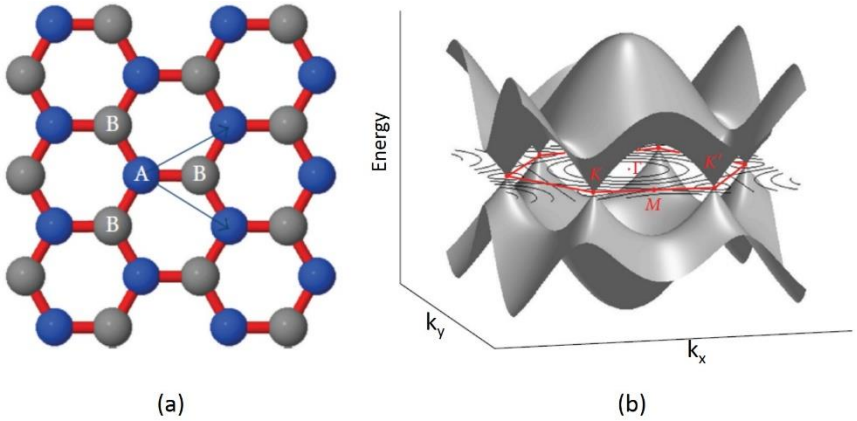

Figure 2-3 From Ref. [36]. (a) Triangular sublattices of graphene. Each atom A has three nearest neighbor of sublattice B, and vice versa. Blue and grey balls represent two sets of interleaving triangular lattices. (b) First Brillouin zone (red hexagon) and band structure of graphene. Z axis and xy plane are energy and momentum space, respectively. K and K' are two nonequivalent corners of the first Brillouin zone and known as the Dirac points. M is the midpoint between adjacent K and K' points and Γ is the zone center.

When graphene is epitaxially grown on a crystalline substrate, there is a registry between the two. Depending on the substrate, the properties of graphene are changed compared to ideal free-standing graphene. For transition metal substrates, a strong hybridization

between the graphene π band and the metal *d* bands can introduce charge transfer from the substrate and modify the electronic properties of graphene greatly [37–39]. Under this circumstance, the Fermi energy may not be necessarily at the Dirac point and can be tuned by intercalations of other atoms [40–42] or small molecules [43,44]. Moreover, different adsorption geometries for graphene on the metal substrate can coexist. Figure 2-4 shows an example of graphene on Ni(111). According to DFT calculations, the bridge-top and top-fcc geometries are two favored structures in this system [45].

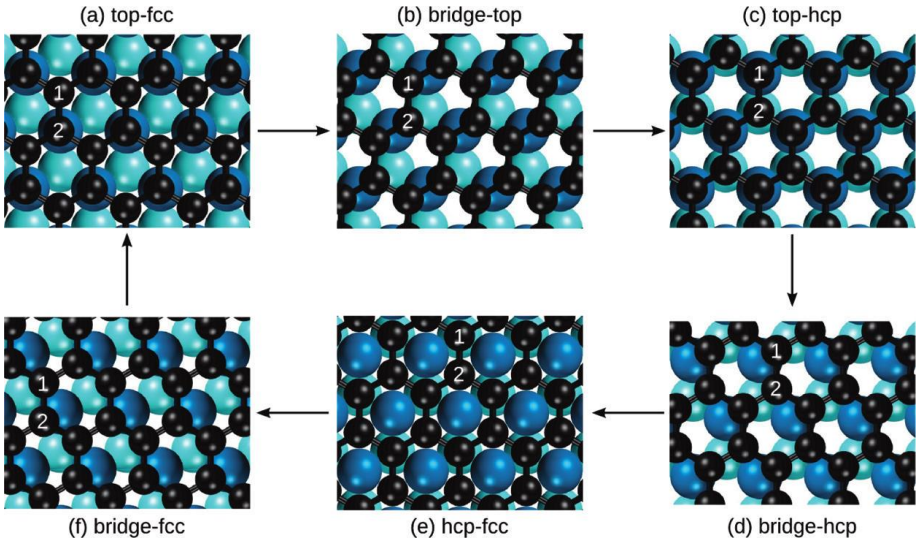

Figure 2-4 From Ref. [45]. Graphene on a Ni(111) surface with different adsorption geometries. The geometries evolve from each other by a shift of the graphene layer against the (111) surface in a direction along a carbon-carbon bond. Carbon atoms are represented by black balls. The first and second metal layers are marked by blue and cyan balls, respectively.

2.4 Magnetic thin films

2.4.1 Magnetic anisotropy in magnetic thin films

Anisotropy generally means that some property is directionally dependent and is the opposite of isotropy. In magnetism, magnetic anisotropy describes the magnetization-direction dependence of the ground state energy and defines the preferential (easy), intermediate and hard directions of the magnetization. In thin films or layered systems, the magnetic anisotropy can differ remarkably from that in bulk materials. The magnetic

anisotropy for thin films or layered systems originates mainly from two sources, i.e., magnetic dipolar interaction (magnetic origin) and spin-orbit interaction (electronic origin). The long-range magnetic dipolar interaction in finite samples does not cancel and thus contributes to the shape-dependent anisotropy, i.e., shape anisotropy, which favors an in-plane magnetization direction. The spin-orbit coupling is the dipole interaction between an electron spin and the magnetic field created by the electron's own orbital motion [46]. Without considering the orbital moment, the electron-spin system is magnetically isotropic. Taking the spin-orbit interaction into account, because of the introduction of a small orbital momentum, the total magnetic moment is coupled to the crystalline lattice, such that the anisotropy energy exhibits a crystalline-axis-dependent property and reflects the overall crystalline symmetry. It is thus called "magnetocrystalline anisotropy". In solids, spin-orbit coupling and crystal-field interaction are key requirements for magnetocrystalline anisotropy and are competing against each other. The latter favors the quenching of the orbital moment and the quenched orbitals demonstrate a standing-wave character and adapt more easily to the crystal field than unquenched or running-wave orbitals. The competition determines the degree of quenching and magnitude of magnetic anisotropy [46].

The Heisenberg exchange interaction between electron spins [47] and magnetic dipolar interaction could also be considered for contributing to the magnetocrystalline anisotropy. But since the exchange interaction is proportional to the scalar product of the spin vectors which are independent of the crystal axes, the exchange interaction turns out to be isotropic and does not contribute to the magnetocrystalline anisotropy. Depending on the symmetry of the crystal, the magnetic dipolar interaction may contribute to the magnetocrystalline anisotropy. If the sum of magnetic dipole-dipole energies cancels, there is no dipolar contribution. For hexagonal crystals with a relatively lower symmetry, the magnetic orbital moment is not fully quenched and the dipolar contribution to the magnetocrystalline anisotropy could also exist, but is too small and can be neglected [48]. Accordingly, the spin-orbit interaction is the main origin of magnetocrystalline anisotropy and will yield the bulk anisotropy, as well as surface and interface anisotropies [49] especially at surfaces and interfaces with a broken crystalline-lattice symmetry. The key feature for surface and interface anisotropies is that the strengths and symmetries depend on the indexing of the surfaces.

In 3*d* transition metals, 3*d* electrons tend to have strong quenching of orbital moment in a crystal field and thus spin-orbit interaction is too weak that the magnetic moment originates almost purely from the spins of 3*d* electrons. In rare-earth metals, in contrast, because of the high effective nuclear charge of inner electrons, the spin-orbit coupling is enhanced. Therefore, typically, the 3*d* anisotropy is much smaller than rare-earth anisotropies, but some non-cubic or strained-3*d* magnets exhibit high room-temperature anisotropies, e.g., YCo_5 (5 MJ/m^3) and $SmCo_5$ (14 MJ/m^3).

When a uniaxial strain is present in a system, e.g., in epitaxial thin films on a mismatched substrate, the spin-orbit interaction may introduce uniaxial magnetoelastic anisotropy. The magnetoelasticity is closely related to magnetostriction, in which a mechanical strain is created by a rotation of the magnetization direction [46]. To describe the magnetic anisotropy energy E for a magnetic thin film system, a uniaxial anisotropy is expressed as [48]

$$E = -K\cos^2\theta \tag{2-1}$$

where K is the magnetic anisotropy constant describing the anisotropy strength, and θ is the angle between the magnetization direction and the surface normal. A second-order uniaxial term $K_2\cos^4\theta$ and the ones with even higher orders are not included in this equation because they are usually very small (the magnitude decreases strongly with increasing the order). However, higher order terms need to be considered in some experimental cases [46]. In magnetic thin films, contributions from the surface or interface and from volume or bulk need to be taken into account. The anisotropy K is thus a sum of all the anisotropy contributions from different sources and can be interpreted as an effective anisotropy K_{eff} expressed phenomenologically as [48]

$$K = K_{eff} = K_V + 2K_S/t \tag{2-2}$$

in which K_S and K_V indicate the surface (or interface) anisotropy per unit cell and volume (or bulk) anisotropy per unit cell, respectively. The film thickness is represented by t. The factor 2 in the equation is based on the assumption of a magnetic layer bounded by two identical interfaces. Depending on the film thickness, the volume and surface anisotropy may have different weights. However, in a film with just a few atomic layers, simply separating the total anisotropy in terms of volume and shape anisotropy is somehow

questionable. Roughness and interdiffusion at interfaces may vary the surface anisotropy and the volume anisotropy is not necessarily independent of film thickness, for instance, K_V could demonstrate a thickness dependence when a stress is induced in the film [48].

2.4.2 Noncollinear spin structures at surfaces of magnetic thin films

Noncollinear spin structures can arise from different reasons, such as competing interatomic exchange interaction between nearest neighbors and second-nearest neighbors, magnetostatic self-interaction, and Dzyaloshinskii-Moriya interaction [50–52] (DMI). The magnetostatic self-interaction favors magnetic domains with partial or complete flux closure. It has a long-range character and is often considered in micromagnetics, which is not the issue in this thesis. The following part in this section will thus focus on the influence of the other two reasons for noncollinear spin structures at surfaces or interfaces.

In the isotropic simple Heisenberg exchange model

$$E_H = -\sum_{i<j} J_{ij} \vec{S}_i \cdot \vec{S}_j, \tag{2-3}$$

a positive (negative) exchange constant J_{ij} favors parallel (antiparallel) electron spins in ferromagnets (antiferromagnets). Typical antiferromagnets have crystallographically equivalent but magnetically nonequivalent sites. The competition between the nearest-neighbor and the second-nearest-neighbor, between the linear and quadratic or higher-order interactions in magnetic nanostructures may give rise to noncollinear spin structures. Moreover, in a fcc lattice, even only nearest-neighbor Heisenberg interaction is frustrated and may lead to 1Q, 2Q, or 3Q spin structure (or any linear combination of them). An example for the competing exchange-interaction caused noncollinear spin structure is given in Figure 2-5, which is from a spin-polarized scanning tunneling microscopy (Sp-STM) study (refer to section 2.5). A bilayer Fe island on Cu(111) is shown in Figure 2-5 (a). A stripe pattern is present on the island at a magnetic field of 3 T, in contrast to 0 T, where no stripe are seen. The pure magnetic signal in Figure 2-5 (d) obtained by subtracting the zero-magnetic-field map in Figure 2-5 (b) from (c) exhibits a clear stripe-shape corrugation, which corresponds to a noncollinear helical spin alignment. The presence of such a noncollinear spin texture is driven by sizeable exchange interactions between long-distance neighbors within the island of reduced dimensionality [53]. Additionally, at surfaces, when the crystalline lattice exhibits some degree of reconstruction, the competing interatomic

exchange interaction will lead to distinct noncollinear spin configurations, as discussed in section 3.3.2.

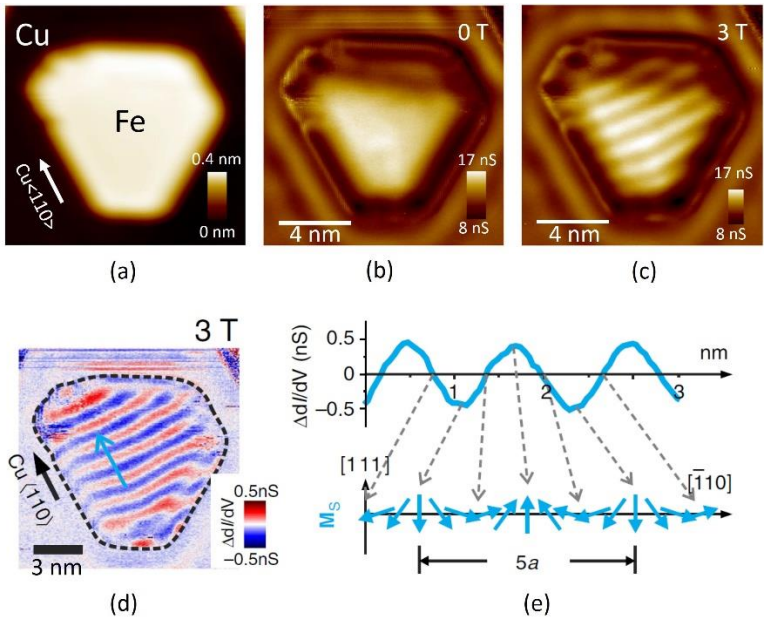

Figure 2-5 From Ref. [53]. (a) Constant-current STM topography image of a bilayer Fe island on Cu(111). (b), (c) Differential conductance maps of the same area in (a) at an external magnetic field of 0 T and 3 T, respectively. (d) Differential-conductance-map difference between (b) and (c) and pure magnetic signal is presented in this map. The Fe island edge is marked by a black dashed line. The STM tip is sensitive to both in-plane and out-of-plane magnetization alignment at 0 T, while only sensitive to the out-of-plane component at 3 T. (e) Sketch of the position dependence of local spin alignment (bottom) along the profile (top) indicated by a blue arrow in (d). Feedback parameters: -0.3 V, 3 nA.

Different from the crystalline bulk with inversion symmetry, a crystal surface loses the inversion symmetry due to reduced dimensionality. In such a case, because of the spin-orbit interaction that connects the crystal field and the spin symmetry, the broken parity of the lattice results in an unconventional anisotropy contribution of relativistic exchange interactions at the surface. This interaction is the DMI and can be expressed as

$$E_{DM} = -\frac{1}{2}\sum_{ij} \vec{D}_{ij} \cdot (\vec{S}_i \times \vec{S}_j) \tag{2-4}$$

where $\vec{D}_{ij}$ is the Dzyaloshinskii vector, which reflects the local environment of the magnetic atoms [46]. $\vec{S}_i$ and $\vec{S}_j$ are electron spin vectors at sites i and j, respectively. The Dzyaloshinskii vector is determined by a simple relation shown in Figure 2-6 and can be expressed as [54]

$$\vec{D}_{ij} \propto \vec{R}_i \times \vec{R}_j = \vec{R}_{ij} \times \vec{r} \tag{2-5}$$

where $\vec{R}_i$, $\vec{R}_j$, $\vec{R}_{ij}$, and $\vec{r}$ are distance vectors. For surfaces, $\vec{r}$ is always pointing in the surface normal direction. If the three atoms shown in Figure 2-6 are aligned in one line, $\vec{r}$ becomes zero and no symmetry breaking occurs, thus no DMI is present.

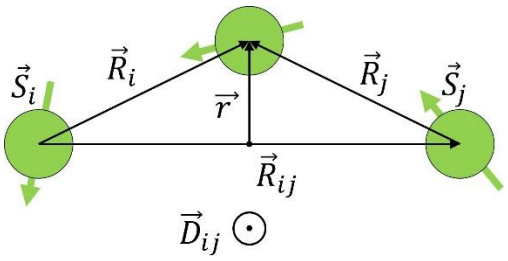

Figure 2-6 A sketch of determining the Dzyaloshinskii vector $\vec{D}_{ij}$ by the local geometry of near-neighbor superexchange interactions [50,51,54]. Green balls and green arrows indicate atom positions and the respective spin vectors.

The DMI arises from spin-orbit scattering of hopping electrons in an inversion-asymmetric crystal field and the scattering sequence of spin-polarized electrons, for instance, $i \to j \to i$ does not commute $j \to i \to j$, i.e., $\vec{D}_{ij} = -\vec{D}_{ji}$. The crystal-field interaction depends on the spin direction, and electrons on sites with a broken inversion symmetry may no longer maintain a uniaxial ferromagnetic or antiferromagnetic structure, instead, a directional noncollinear surface spin structure can be formed for the purpose of minimizing the crystal-field energy. Such a noncollinear surface spin structure possesses a specific chirality, i.e., $\vec{C}_i = \vec{S}_i \times \vec{S}_{i+1}$, either right-handed ($\vec{C}_i > 0$) or left handed ($\vec{C}_i < 0$) [55]. In magnetically ordered systems, DMI favors a spin canting of parallel- or antiparallel-aligned spin moments while competing with the Heisenberg exchange, and thus a weak net ferromagnetic behavior can be present in an antiferromagnet. Figure 2-7 is an example of a simulated noncollinear spin texture caused by DMI in1 ML Mn/W(001) [53]. The simulation is consistent to the real experimental result. The stripe pattern on the left

corresponds to the magnetic structure of the sample and the special spin arrangement is illustrated on the right. In this model, a left-handed cycloidal spin spiral with 36° angle between neighboring moments is present.

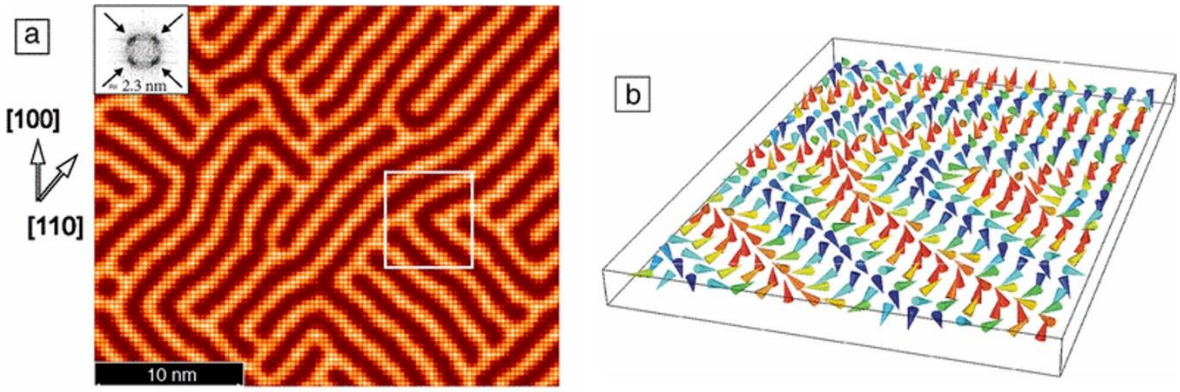

Figure 2-7 From Ref. [56]. (a) A Monte Carlo simulation of an Sp-STM image of the noncollinear spin texture of 1 ML Mn/W(001) at 13 K. The inset shows the Fourier transform. This simulation is performed according to the experimental data. (b) Perspective view of electron spins illustrated by cones for the area marked by a white rectangle in (a). Colors of cones represent vertical components of spins. Red and dark blue colors mean completely up and down, respectively. The others are canted spins with canting angles between up and down.

2.4.3 Layered antiferromagnets in ferromagnetic/antiferromagnetic heterostructures

Ferromagnetic/antiferromagnetic heterostructure have been playing an important role in modern magnetic data storage. An AFM thin film could be employed as the pinning layer for ferromagnetic layers in spin-valve structures, e.g., in hard drive read heads, magnetic sensors, MRAM, etc. At the interface of ferromagnetic/antiferromagnetic heterostructures [57], the magnetic moments of both materials are exchange coupled. The interaction with the ferromagnetic layer could introduce some long-range ferromagnetic order in the antiferromagnetic layer that does not show any ferromagnetic order in the bulk phase (nonmagnetic or antiferromagnetic) [58–60], such that the antiferromagnetic layer may be either parallel or antiparallel to the magnetization direction of the ferromagnet. Within a certain thickness range, when the antiferromagnetic layer is exchange coupled to a

ferromagnetic layer, its ordering temperature may be significantly influenced by the presence of the ferromagnet and also by the magnetization direction [5]. For a thick antiferromagnetic film exchange coupled to the ferromagnet at the interface, its property is close to the bulk material, which does not depend on the ferromagnet in the heterostructure. In layered systems composed of ferromagnetic/antiferromagnetic materials, the exchange interaction at the interface of the two materials can modify the magnetic behavior of the system by the "exchange anisotropy" ("exchange bias") [3]. Phenomenologically, the exchange anisotropoy describes a hysteresis loop shift phenomenon when cooling the sample from above the Néel temperature (needs to be higher than the Curie temperature of the ferromagnet) in an external field. In antiferromagnets, the net magnetization is zero and the antiferromagnetic spin configuration is difficult to probe. The discovery of the magnetic exchange anisotropy opens an indirect way of measuring the antiferromagnetic ordering. Techniques, such as magneto-optical Kerr effect (MOKE) or x-ray magnetic circular dichroism (XMCD) can probe the magnetic behavior of the ferromagnetic material under the influence of the exchange-coupled antiferromagnetic layers in the heterostructure system. Thus possible spin arrangements in the antiferromagnetic layers could be predicted. There are also direct methods for observing the antiferromagnetic surface spin structures, like x-ray magnetic linear dichroism (XMLD) and Sp-STM. The latter could present a much higher magnetic resolution reaching the atomic scale. Details about these techniques are introduced in the next section.

2.5 Spin-polarized scanning tunneling microscopy and spectroscopy

2.5.1 Theory of scanning tunneling microscopy

The tunneling effect is a quantum mechanical phenomenon in which a particle, e.g., an electron, is described by a wave function and may tunnel through a potential energy barrier existing between two classically allowed regions. Since the probability for quantum tunneling was found to decreases exponentially with the barrier width, a small enough barrier width is necessary to observe the tunneling phenomenon experimentally. The discovery of electron tunneling phenomena in semiconductors [61,62] and superconductors [63–66] resulted in the Nobel Prize in Physics in 1973 and had a long-term impact in the

following couple of decades. The tunneling through a vacuum barrier between two metal electrodes was firstly reported by Young et al. [67,68]. Not until the invention of the scanning tunneling microscope (STM) [69,70] by Binnig and Rohrer with coworkers in 1981, the vacuum tunneling was successfully combined with a piezoelectric drive system and a new era of science with lateral resolution on the Angstrom level started. A sketch for the basic mechanism of an STM setup is shown in Figure 2-8 (a). When a metal tip is brought close to a conducting sample surface within a distance of a few Å, the electronic wave functions for both will overlap significantly. By applying an external electric field, i.e., a bias voltage, between the tip and sample, a tunneling current can flow from the occupied electronic states near the Fermi level of one electrode into the unoccupied states of the other electrode, as shown in Figure 2-8 (b). At positive bias voltages, electrons tunnel from tip to sample, and vice versa for negative voltages. Combining the tip with a piezoelectric drive system and a feedback loop, the surface topography can be measured.

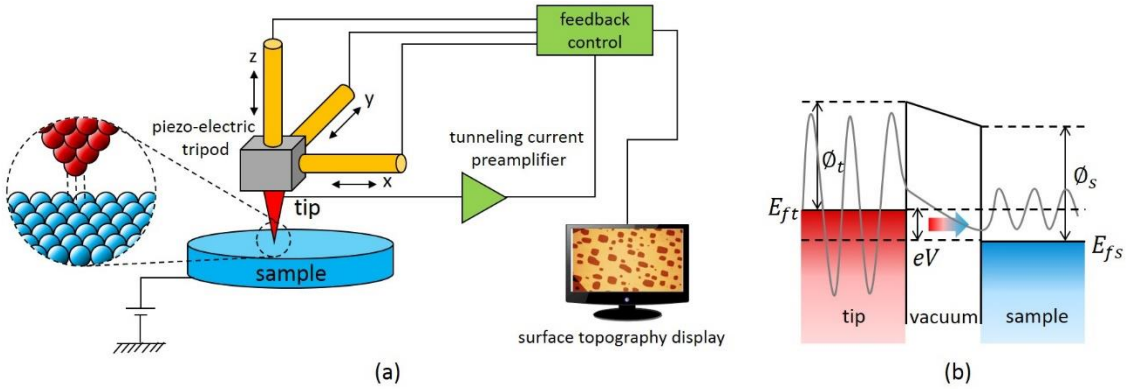

Figure 2-8 (a) A sketch of the operating mechanism of STM. A small bias voltage is applied between the tip and the sample. Inside the circle, a tunneling process between the tip apex and the sample surface is sketched. (b) A sketch of the electron tunneling process between STM tip (grounded) and sample at a positive bias voltage V. $\emptyset_t$ and $\emptyset_s$ indicate work functions of the tip and the sample, respectively. E_{ft} and E_{fs} are the Fermi energies of the tip and the sample, respectively. The gray line indicates an electronic wave function at the Fermi energy of the tip.

The STM tunneling process is based on a three-dimensional variation of charge density at a surface. At low bias voltage V and small vacuum gap, the electron tunneling current I in an STM measurement decays exponentially with the barrier width d, as illustrated by [71]

$$I \propto \frac{V}{d}\exp(-A\sqrt{\emptyset}d), \tag{2-6}$$

where A is a constant and $\emptyset = (\emptyset_t + \emptyset_s)/2$ is the average work function of tip and sample. To analyze the tunneling current between tip and sample in an STM measurement quantitatively by first-order perturbation theory and Fermi's golden rule, the tunneling current can be illustrated in the Bardeen approach [72] by

$$I = (2\pi e/\hbar)\sum_{ts}\{f(E_t)[1 - f(E_s + eV)] \times |M_{ts}|^2\delta(E_t - E_s)\}, \tag{2-7}$$

in which $f(E) = \{\exp[(E - E_f)/(k_B T)] + 1\}^{-1}$ is the Fermi-Dirac distribution function, M_{ts} is the tunneling matrix element of the perturbation potential between states ψ_t of the tip and ψ_s of the surface. V is the bias voltage. E_t is the energy of state ψ_t in the absence of tunneling. The δ-function ensures energy conservation. The Tersoff-Hamann model [73,74] assumes the tip as a locally spherical potential well where it approaches nearest to the surface. In this model, taking the limits of small voltage and low temperature, the tunneling current can be expressed as [73]

$$I = (2\pi e/\hbar)e^2 V\sum_{ts}|M_{ts}|^2\delta(E_s - E_f)\,\delta(E_t - E_f). \tag{2-8}$$

To calculate M_{ts}, the WKB (Wentzel-Kramers-Brillouin) approximation for free electrons [72] is applied to equation (2-8), giving rise to [73]

$$M_{ts} = -(\hbar^2/2m)\int d\vec{S}\,(\psi_t^*\nabla\psi_s - \psi_s\nabla\psi_t^*) \tag{2-9}$$

where m represents the electron effective mass. Substituting the *s*-wave tip wave function, the tunneling matrix element can be expressed as [73]

$$M_{ts} = (\hbar^2/2m)4\pi k^{-1}\Omega_t^{-\frac{1}{2}}kRe^{kR}\psi_s(\vec{r}_0) \tag{2-10}$$

where $k = \hbar^{-1}(2m\emptyset)^{1/2}$ is the inverse decay length for the wave functions in vacuum, Ω_t the tip volume, R the radius of curvature. $\vec{r}_0$ is the center of the tip curvature. The tunneling current can therefore be expressed as [73]

$$I = 32\pi^3\hbar^{-1}e^2V\emptyset^2\rho_t(E_f)R^2k^{-4}e^{2kR}\sum_s|\psi_s(\vec{r}_0)|^2\delta(E_s - E_f) \tag{2-11}$$

where ρ_t is the density of states per volume of the tip. Assuming a constant tip density of states near the Fermi level, this equation illustrates that the tunneling current is proportional to the local density of states of the sample surface at the place of the tip. Nevertheless, this

Tersoff and Hamann theory for STM is based on small bias voltage (about 10 meV) and low temperatures. The actual bias voltage in STM measurements varies in a range of a few volts. At large bias voltages, the Tersoff-Hamann model does not apply.

2.5.2 Theory of spin-polarized scanning tunneling microscopy and spectroscopy

The Bardeen summation form of the tunneling current in equation (2-7) can be illustrated in the integration form as [75]

$$I = I_{t\to s} - I_{s\to t} = \frac{2\pi e}{\hbar}\int_{-\infty}^{+\infty}|M_{ts}(E)|^2\,\rho_t(E-eV)\rho_s(E)f_t(E-eV)[1-f_s(E)]dE - \frac{2\pi e}{\hbar}\int_{-\infty}^{+\infty}|M_{ts}(E)|^2\,\rho_t(E-eV)\rho_s(E)f_s(E)[1-f_t(E-eV)]dE = -\frac{2\pi e}{\hbar}\int_{-\infty}^{+\infty}|M_{ts}(E)|^2\,\rho_t(E-eV)\rho_s(E)[f_s(E)-f_t(E-eV)]dE. \quad (2\text{-}12)$$

The differential conductance at zero-bias of the tunneling junction between tip and sample is thus given by [75]

$$\frac{dI}{dV} \propto |M_{ts}(E)|^2\rho_t(E)\rho_s(E). \quad (2\text{-}13)$$

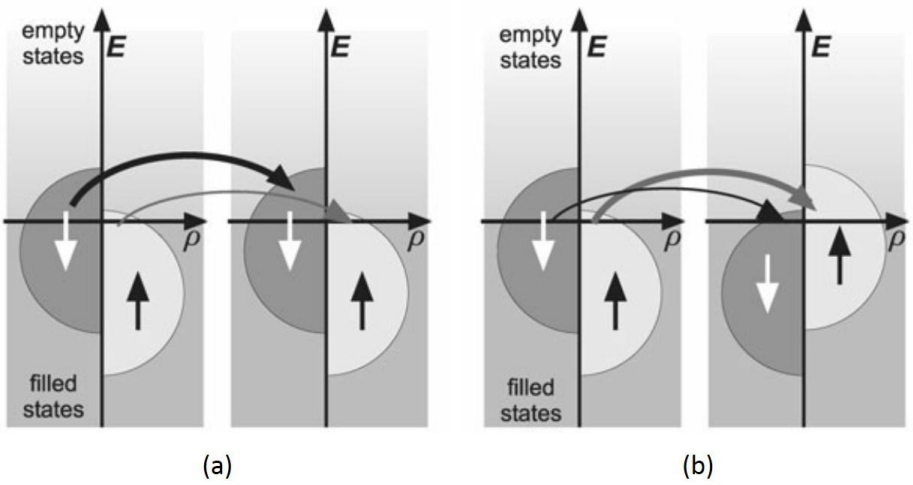

Figure 2-9 From Ref. [75]. Sketch of spin-polarized tunneling between magnetic tip and sample in case of (a) parallel and (b) antiparallel magnetization. The electron spin is conserved and the tunneling process is elastic. The spin-up (spin-down) electrons can only tunnel from occupied states of the tip to the spin-up (spin-down) unoccupied states of the sample. The small black and white arrows illustrate spin-up and spin-down electrons, respectively.

In ferro- or antiferromagnetic materials, owing to the quantum mechanical exchange interaction between electrons, the density of states splits up into majority and minority states. This imbalance causes a spin polarization which is different from paramagnetic substances with identical spin-up and spin-down electron distributions [76]. When spin-polarized tip and sample are used, the tunneling current should depend on the relative spin direction of both electrodes [75]. A simplified Stoner model shown in Figure 2-9 illustrates the tunneling process at a positive bias voltage V applied between the tip and the sample. The spin-up and spin-down bands are both shifted, giving rise to a spin polarization near the Fermi level [76], i.e.,

$$P_{ts}(E_f) = \frac{\rho_{ts}^{\uparrow}(E_f) - \rho_{ts}^{\downarrow}(E_f)}{\rho_{ts}^{\uparrow}(E_f) + \rho_{ts}^{\downarrow}(E_f)} \tag{2-14}$$

At small bias, the tunneling is elastic. The electron spins are preserved when tunneling through the vacuum barrier and spin-up electrons from one electrode are forbidden to tunnel into the spin down bands of the other. Accordingly, at zero-bias voltage, the parallel electron spin conductivity is expressed as [76]

$$\left(\frac{dI}{dV}\right)^{\uparrow\uparrow} = G^{\uparrow\uparrow} \propto \rho_t^{\uparrow}(E_f)\rho_s^{\uparrow}(E_f) + \rho_t^{\downarrow}(E_f)\rho_s^{\downarrow}(E_f), \tag{2-15}$$

and the antiparallel electron spin conductivity is [76]

$$\left(\frac{dI}{dV}\right)^{\uparrow\downarrow} = G^{\uparrow\downarrow} \propto \rho_t^{\uparrow}(E_f)\rho_s^{\downarrow}(E_f) + \rho_t^{\downarrow}(E_f)\rho_s^{\uparrow}(E_f). \tag{2-16}$$

Inelastic tunneling is also likely to happen, e.g., spin-flip scattering, but compared to the elastic tunneling, it can be neglected in a first approximation [75]. The parallel and antiparallel conductivities are generally not equivalent, leading to a tunneling-current difference with respect to the magnetic configuration of both electrodes. Slonczewski calculated the dependence of conductivity on the relative angle θ between spin vectors of the two electrodes for spin-polarized tunneling [77], that is,

$$G = G_0(1 + P_t P_s cos\theta) \tag{2-17}$$

where G_0 is the conductivity at zero bias, P_t and P_s are spin polarizations of tip and sample, respectively. This equation predicts the angular dependence of tunneling magnetoresistance (TMR) effect [78,79].

2.5.3 Operation modes of Sp-STM

Before discussing the magnetic imaging of Sp-STM, two operating modes of an STM will be introduced briefly, i.e., constant current mode and constant height mode. The former means that while an STM tip is scanning over different areas continuously on the sample surface, the feedback loop will maintain a constant tunneling current by adjusting the tip-sample distance. The constant height mode is somehow different, that is, during the tunneling process, the feedback loop will be open. The drawback of this mode is that, when on a surface with large corrugations, the tip may crash into the surface easily when the imaging is performed with a small tip-sample distance.

To extract the magnetic signal by Sp-STM method, there are mainly two imaging modes, the spectroscopic mode and the differential magnetic mode [76]. The spectroscopic mode is also named as spin-polarized scanning tunneling spectroscopy (Sp-STS). At a constant current mode, any variation of the tunneling conductance will be compensated by a change in the tip-sample distance. The obtained topography contains both electronic and magnetic information. In Sp-STS mode, the feedback loop is open while regulating the bias voltage, leading to a change in the tunneling current. If the spin polarization of the sample changes with the energy, the tunneling current for a parallel spin alignment of tip and sample will be higher than the antiparallel case. In this mode, an AC-voltage modulation generated by a lock-in amplifier is superimposed to the DC-bias voltage. If the modulation added to the bias voltage is low, according to the Tersoff-Hamann model of STM, the spin-polarized tunneling current does not depend on the electron energy. Then the first harmonic signal of the corresponding tunneling current expanded in Taylor series will correspond to the differential conductance (dI/dV) which contains the magnetic information [80]. Nevertheless, such mode depends strongly on the variations of the local density of states and the differential conductance signal depends usually only weakly on the spin. Therefore, the Sp-STS approach is limited to surfaces with homogeneous electronic configurations.

In the differential magnetic mode, a magnetically bistable tip is used and its magnetization can be switched periodically between two opposite magnetization directions, which is identical to changing the sign of the spin-polarization of the tip. With a phase-sensitive lock-in amplifier, the differential conductance is proportional to $P_t P_s cos\theta$ and pure spin signal can be separated from the topography [81]. The disadvantage for this mode is that

the sample cannot be magnetized by an external magnetic field during imaging because the tip magnetization will be influenced.

2.6 Other techniques for thin-film characterization

2.6.1 Low-energy electron diffraction

Scattering experiments are important and can provide information in surface and thin-film research. Elastic scattering (the energy of a scattered particle is conserved before and after scattering) can reflect the symmetry and geometric arrangement of atoms near the surface, while inelastic scattering (some energy is transferred to or from the topmost layer of a solid) tells both electronic and vibronic excitations of a surface or interface. In surface and interface studies, surface sensitivity of probing particles is required. Neutrons are not favored in the scattering experiment for probing the information of surface atoms because they weakly interact with the solid material. Neither are *x* rays, because they can even penetrate the whole sample and thus carry negligible information of the surface atoms. To employ *x* rays for surface studies, a special geometry and experimental arrangement are required, which is beyond the discussion here. Low-energy atoms, ions, and molecules only interact with the outmost atoms of a solid, while low-energy electrons can penetrate a few atomic layers into the material and have a strong interaction with the valence band electrons of the material. The inelastic mean-free path $\boldsymbol{\lambda}$ (IMFP) of electrons in solids is energy dependent and can be seen from a universal curve in Figure 2-10. This quasi-universal dependence of different materials is because the main interaction mechanism between electrons and the solid is the excitations of plasmon waves whose energy depends on the electron density in the solid. The intensity of the primary electron beam I_0 decays exponentially in the propagating direction in the solid, as expressed by

$$I(d) = I_0 e^{-d/\lambda} \tag{2-18}$$

in which d is the penetration depth.

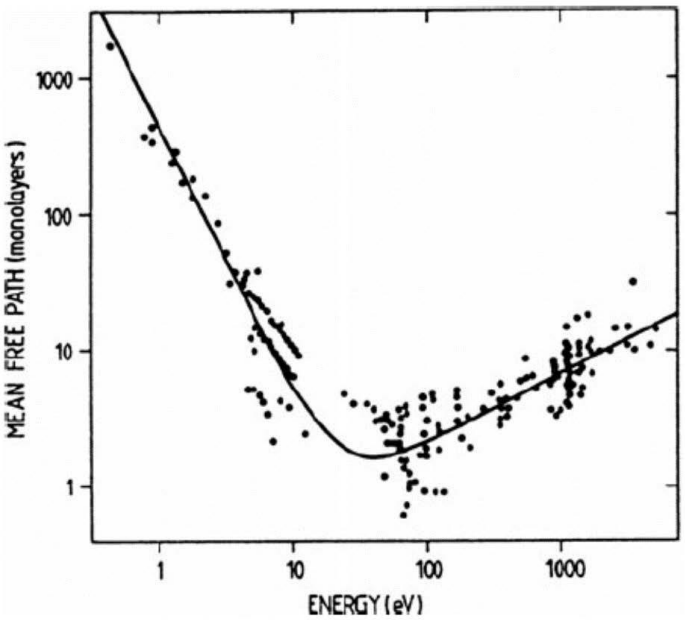

Figure 2-10 From Ref. [82]. Universal curve for the electron mean-free path in solids as a function of their energy.

Low-energy electron diffraction (LEED) is a standard technique for checking the crystallographic quality of a surface nowadays and this technique is based on the wavelike nature of electrons. The typical primary-electron beam energy for LEED experiments is between 20 and 500 eV and elastically backscattered electrons form diffraction (Bragg) spots are made visible on a fluorescent screen. In a kinematic description, electrons imping on a well ordered crystal surface are elastically scattered only once. In this case, the Laue condition is fulfilled for incident and scattered electron plane waves, i.e.,

$$\vec{k} - \vec{k}_0 = \vec{G}_{hkl} \tag{2-19}$$

where $\vec{k}_0$ and $\vec{k}$ are incident and scattered wave vectors having the same magnitude, $|\vec{k}| = |\vec{k}_0|$. $\vec{G}_{hkl}$ is a 3D vector of the reciprocal lattice and h, k, l are Miller indices. According to the universal curve shown in Figure 2-10, in the low energy electron range, only the first few atomic layers contribute to the diffraction. In other words, there are no diffraction conditions normal to the surface, such that in reciprocal space, a surface is a 2D lattice with truncation rods extending perpendicularly from each lattice point. Then the 3D Laue condition can be written in a 2D form:

$$\vec{k}^{\parallel} - \vec{k}_0^{\parallel} = \vec{G}_{hk} \tag{2-20}$$

where $\vec{k}_0^{\parallel}$ and $\vec{k}^{\parallel}$ represent the in-plane components of the incident and scattered electron waves. This 2D Laue condition can be visualized by the Ewald sphere construction shown in Figure 2-11. According to the de Broglie relation $p = h/\lambda$, in which p is the electron momentum and h is the Planck constant, the electron wavelength will be $\lambda = (2mE/h^2)^{-1/2} = \sqrt{150.4/E}$ (λ in Å and E in eV). Thus the typical LEED wavelengths are in the Angstrom range which is of the same magnitude as the interatomic distances.

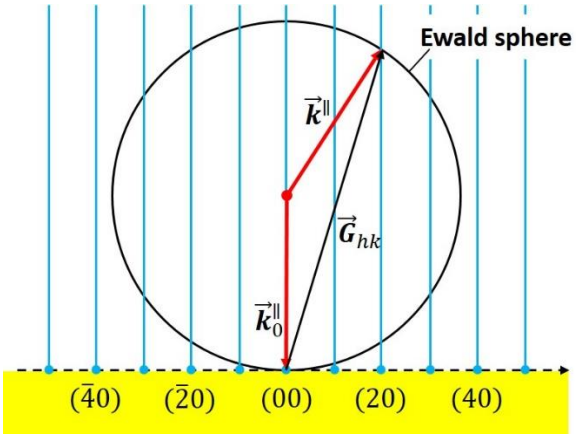

Figure 2-11 Ewald sphere construction for normal incidence of the primary electron beam. The diffracted beams are indexed by h and k. Blue lines indicate the truncation rods in a 2D lattice in reciprocal space and blue dots show the lattice points of the reciprocal lattice.

2.6.2 Medium-energy electron diffraction

The medium-energy electron diffraction (MEED) has a much higher energy for the primary electron beams, typically in the range of 2−5 keV. Because of the higher electron energy, grazing incidence is necessary for minimizing the penetration depth into the sample and increasing the surface sensitivity. Moreover, the diameter of the Ewald sphere is much larger than a reciprocal lattice vector and the reciprocal truncation rods are cut at grazing angles in the region corresponding to a diffracted beam appearing near the surface. The Ewald sphere construction for MEED scattering is schematically shown in Figure 2-12. The Ewald sphere "touches" the rods of the truncation rods, such that both Ewald sphere and the truncation rods are smeared out, due to the angular and energy spread of the primary beam, respectively, and to deviations from ideal translational symmetry in the surface

(phonons, defects, etc.) [32]. Accordingly, the diffraction pattern usually consists not spots, but streaks corresponding to the sections of reciprocal truncation rod intersected.

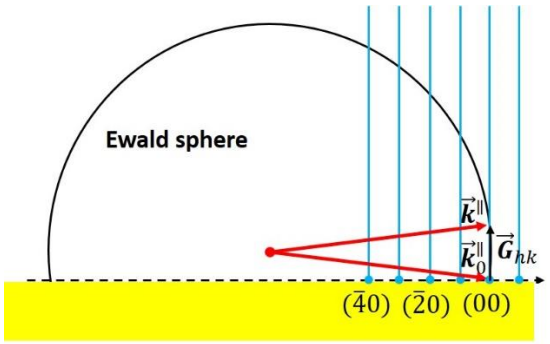

Figure 2-12 Ewald sphere construction for the grazing incidence of primary electron beam. The diffracted beams are indexed by h and k. Blue lines indicate the truncation rods in a 2D lattice in the reciprocal space and blue dots show the lattice points of the reciprocal lattice.

The MEED technique is quite similar to reflection high-energy electron diffraction (RHEED) and both require grazing incidence of primary electron beams, as shown in Figure 2-13. The latter has an even higher energy in a range of 10−100 keV and the grazing incident angle is 3°−5°. They both have equivalent surface sensitivity as LEED and can be employed for *in-situ* thickness monitoring during the layer-by-layer thin-film deposition. Figure 2-14 is a typical MEED curve achieved by monitoring the (00) diffraction spot intensity during room-temperature cobalt (Co) deposition on a Cu(001) substrate. In this curve, there are oscillations with a regular periodicity as a function of time, which is based on the layer-by-layer growth mechanism of Co. When a full atomic layer is completed, the 2D periodicity of the topmost layer is ideal and the diffraction on such atom array causes a maximum spot intensity. Between two complete layers, the surface roughness caused by the presence of islands and steps is higher than the surface with a complete layer, leading to a decrease in the intensity of the diffraction spots. Thus the peak maximum indicates that the growth of the topmost layer is completed and the peak numbers tells the actual thickness (ML) of the film. By this means, an accurate thickness control for the thin film deposition is realized.

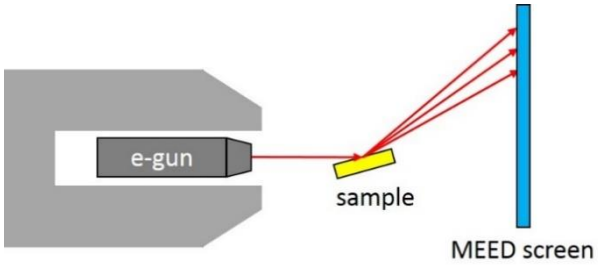

Figure 2-13 Schematic of a MEED setup. The primary electron beams are incident under grazing angles onto the sample surface.

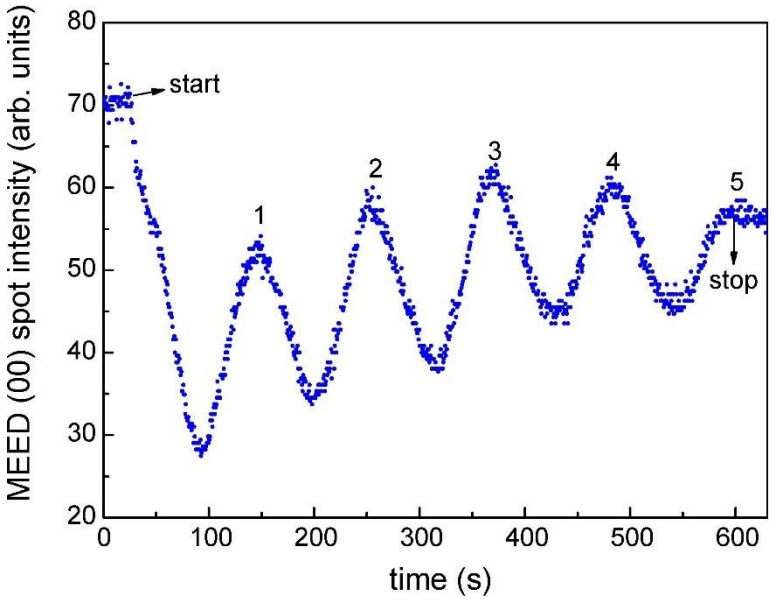

Figure 2-14 A typical MEED curve for (00) spot intensity during cobalt deposition up to 5 ML on Cu(001) substrate at room temperature. “Start” and “stop” mean opening and closing the shutter in the evaporator.

In both LEED and MEED (or RHEED), the primary electron beam is actually not an ideal plane wave, but a mixture of waves with some energy and direction deviations. These deviations from the ideal plane wave direction and energy are due to the finite energetic width with a thermal width of about 500 meV and the angular spread of the beam. The electrons exhibit some random phase variations when reaching the sample surface. If two spots on the surface are separated by a large distance, the incident waves cannot be treated as coherent waves, such that the phases are not correlated and the scattered waves cannot interfere to produce any diffraction pattern. Therefore, there is a coherence length (radius) used for describing the maximum size that can be considered as illuminated by a coherent

plane wave on the sample. Thus waves that are scattered from points with separations larger than the coherence length can only contribute to the background intensity. Therefore no diffraction pattern can be formed for surface structures with periodicities larger than the coherence length [32].

2.6.3 Auger electron spectroscopy

The Auger effect was discovered by Lise Meitner and Pierre Auger independently in the 1920s. Nowadays, the Auger electron spectroscopy (AES) is a standard analytical technique for surface and interface studies in UHV. This technique can be used as a cleanliness check of a surface, for elemental analysis, film thickness determination, and also the depth profiling of the concentration of specific elements.

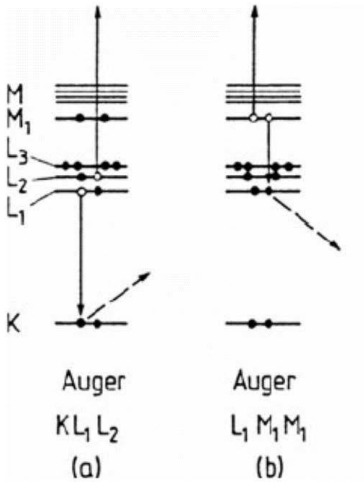

Figure 2-15 From Ref. [32]. Schematic explanation of the Auger process. K, L_1, L_2, L_3, M_1, and M indicate different shell numbers. The emitted Auger electrons are named by KL_1L_2 and $L_1M_1M_2$ in (a) and (b), respectively. The left shell number is for the core-shell escaping electron, the middle one is for the first-outer shell electron, and the right one is for the second-outer shell electron.

AES is an electron core-level spectroscopy. In an Auger process, a primary electron reaching the sample generates a core-level escaping electron, as indicated by a dashed arrow in Figure 2-15. This core-hole vacancy can be filled by an outer-shell electron, thus the electron loses an amount of energy equal to the energy difference between the two orbitals. This part of energy can be transferred to a second outer-shell electron which will

be emitted from the atom if the transferred energy is larger than the orbital binding energy. This latter emitted second outer-shell electron is the Auger electron which has the characteristic element-specific property and carries a well-defined kinetic energy related to differences in core-level energies. In a simplified model without considering complex many-body effects, the kinetic energy E_{kin} for an Auger electron can be calculated by [32]

$$E_{kin} = E_{core} - E_{fo} - E_{so}^{*} \tag{2-21}$$

where E_{core} and E_{fo} are the core-level and first-outer-shell binding energies, respectivey, while E_{so}^{*} is the effective binding energy for the doubly ionized state of the second-outer-shell. Since orbital energies, i.e., E_{core}, E_{fo}, and E_{so}^{*} here are unique to an atom of a specific element, the kinetic energy of Auger electrons are characteristic features of different elements. Typical probing depths in AES are in the range of 1–3 nm. According to the universal curve shown in Figure 2-10 before, for an Auger electron with a kinetic energy of 1000 eV, its penetration depth will be around 10 ML. Therefore, AES is highly surface sensitive.

The Coulomb interaction facilitates the energy transfer between electrons in an Auger process which is a complex process involving several steps. Such a process does not obey the dipole selection rules that govern optical transitions. Moreover, in contrast to the strong atomic number (Z) dependent radiative transitions, the Auger-transition probability is roughly independent of Z [32].

The AES spectrum can be utilized for thin-film thickness calibrations. The relative sensitivity parameters for the substrate and the film are S_s and S_f respectively. e^{-d/λ_f} is the probability of the substrate Auger electron travelling a distance d (ML) through the solid without undergoing scattering. $(1 - e^{-d/\lambda_f})$ is the probability of the film Auger electrons after travelling through a distance d. Then for a single film on the substrate, the AES peak-to-peak ratio I_f/I_s for the film and substrate signals can be expressed as

$$\frac{I_f}{I_s} = \frac{S_f}{S_s} \cdot \frac{1-\exp\left(-\frac{d}{\lambda_f}\right)}{\exp\left(-\frac{d}{\lambda_s}\right)} \tag{2-22}$$

where λ_f (Å/ML) and λ_s (Å/ML) are effective inelastic mean free paths in the film for Auger electrons emitted from the film and substrate atoms, respectively. When there are

two different thin films on the substrate, the AES peak-to-peak ratio for the topmost film (thickness d_{tf}) and the substrate is I_{tf}/I_s and can be expressed as

$$\frac{I_{tf}}{I_s} = \frac{S_{tf}}{S_s} \cdot \frac{1-\exp\left(-\frac{d_{tf}}{\lambda_{tf}}\right)}{\exp\left(-\frac{d_{tf}}{\lambda_s}\right)\exp\left(-\frac{d_{sf}}{\lambda_s}\right)} \tag{2-23}$$

where the subscript tf and sf mean the topmost and the second topmost films, respectively. The AES peak-to-peak ratio for the topmost film and the second film underneath is

$$\frac{I_{tf}}{I_{sf}} = \frac{S_{tf}}{S_{sf}} \cdot \frac{1-\exp\left(-\frac{d_{tf}}{\lambda_{tf}}\right)}{\exp\left(-\frac{d_{tf}}{\lambda_{sf}}\right)\left[1-\exp\left(-\frac{d_{sf}}{\lambda_{sf}}\right)\right]}. \tag{2-24}$$

The following table illustrates these parameters related to the Auger electrons of different elements that will appear in the following chapters.

Table 2-1 AES parameters[83]

Element	Energy / eV	λ_{eff} / ML	S_f / S_{Cu920}
Mn	542	2.54	0.35
Mn	589	2.61	0.48
Mn	636	2.76	0.29
Co	656	3.51	0.44
Co	716	4.1	0.71
Co	775	4.85	1
Ni	716	4.4	0.256
Ni	783	4.48	0.478
Ni	848	4.55	1
Cu	920	5.45	1

2.6.4 Magneto-optical Kerr Effect

The magneto-optical phenomenon is a magnetic-field or a spontaneous-magnetization influence on the emission or propagation of light in matter. There are basically four types of magneto-optical effect, i.e., the Faraday and Kerr effects (birefringence effects of circularly polarized light), the Voigt effect (a birefringence of linearly polarized light), and the gradient effect (a birefringence that depends on magnetization gradients) [57]. The Faraday and transmission-Voigt effect are applied to transmission materials, while the Kerr, reflection-Voigt, and gradient effects are probed by reflection of light. The penetration depth of the polarized light provides the magnetization information in a depth range which

for metals is about 20 nm. The Kerr and Faraday effects are linearly dependent on the magnetization vector, while the Voigt effect demonstrates a quadratic dependence. The quadratic scaling stems from an arrangement in which the external magnetic field is applied perpendicular to the light propagation direction. In such a case other effects that are proportional to the magnetic field will vanish. In other geometries where the external magnetic field has a perpendicular component also generate such quadratic scaling. The gradient effect is more sensitive to changes in the magnetization (linear dependence on the magnetization gradient).

The magneto-optical Kerr effect (MOKE) is the polarization change of light by upon reflection at the surface of magnetic materials. This change is only present for a non-zero magnetization and the magnitude is determined by the off-diagonal terms in the permittivity tensor, which are odd linear functions of the magnetization [48,57]. As such MOKE is a suitable technique for studying the changes in magnetization direction or magnitude in the region that is illuminated by a focused light beam. According to the relative orientation of the magnetization vector with respect to the light plane, there are three geometries of MOKE setup, i.e., longitudinal, polar, and transversal, as shown in Figure 2-16.

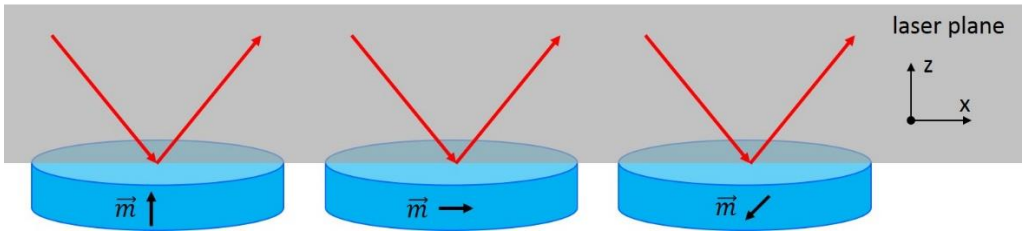

Figure 2-16 Three types of MOKE set up. Left, middle, and right panels show basic layouts of the light plane (the xz plane defined by the red arrows) and magnetization vectors (black arrows) in a polar, longitudinal, and transversal geometry, respectively.

Polar MOKE is more sensitive to the out-of-plane magnetization components. In this case, to simplify the analysis, the circularly polarized light is placed normal to the surface. To probe the in-plane magnetization of a thin film, the longitudinal setup is favored. A simple longitudinal MOKE setup is employed in this work for recording magnetization hysteresis loops by plotting the Kerr intensity as a function of the magnetic field. A schematic MOKE setup is shown in Figure 2-17.

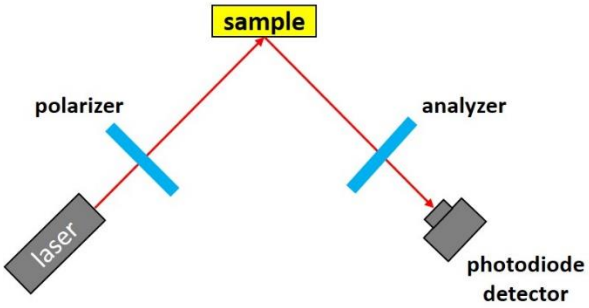

Figure 2-17 A sketch of the longitudinal-MOKE setup for the in-plane magnetization measurement.

2.7 Experimental details

2.7.1 Experimental setup

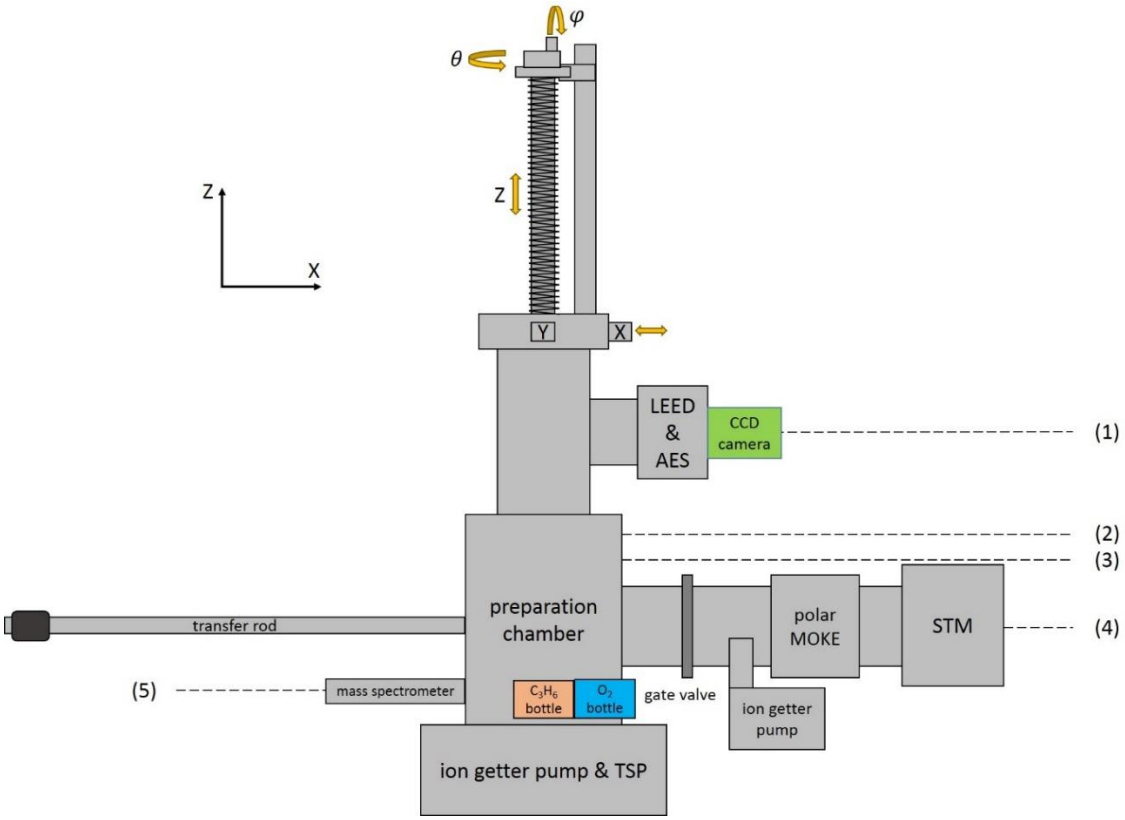

Figure 2-18 A sketch of the side view of the STM-MOKE chamber. (1)–(5) illustrate different heights.

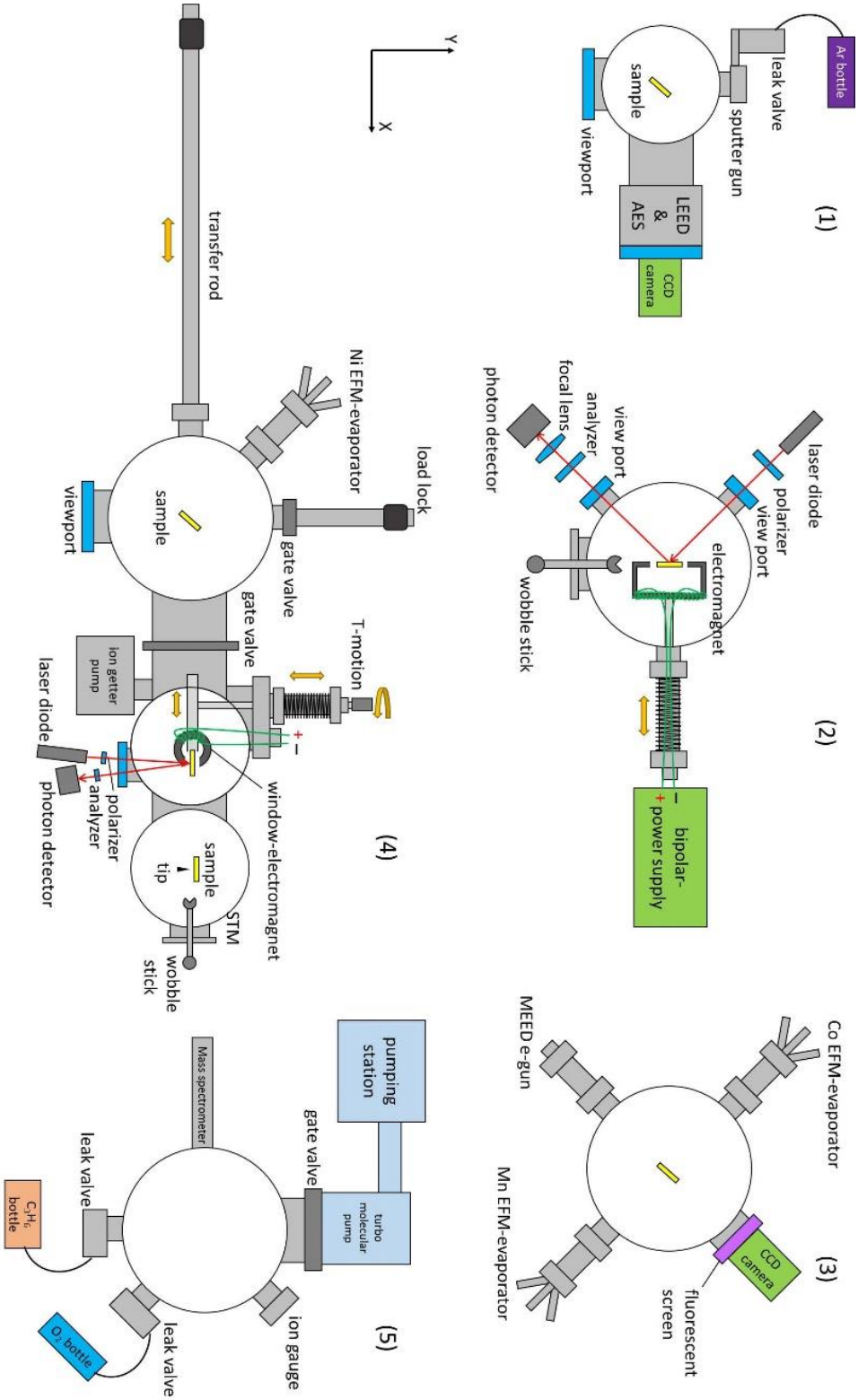

Figure 2-19 Sketches of the bird's eye view of horizontal cross sections of the STM-MOKE chamber. (1)–(5) correspond to the parts marked with the same numbers at different heights in Figure 2-18. Red arrows show laser paths. Yellow arrows indicate possible motions.

Figure 2-18 and Figure 2-19 are sketches of the UHV chamber from the side and top views, respectively. According to the height of different functionalities, the chamber can be divided into five parts, as marked by (1)−(5). Different functionalities are described as follows:

(1) Sputtering, annealing, AES, LEED;
(2) Longitudinal-MOKE (adjustable focus laser module, 635 nm, 4.5 mW, elliptical beam; UHV electromagnet, saturation ~120 Oe);
(3) Molecular beam epitaxy (MBE) with *in-situ* MEED;
(4) Sample transfer, polar-MOKE (adjustable focus laser module, 635 nm, 4.5 mW , elliptical beam; UHV electromagnet, saturation ~1000 Oe), room-temperature STM;
(5) Hydrocarbon gas and oxygen sources, residual gas detection, UHV pumping system.

Additionally, above the height of part (1) is the sample manipulator which has five degrees of freedom for adjusting the sample position and orientation, namely, x (0~25 mm), y (0~25 mm), z (105~570 cm), polar angle θ (0~90°) and azimuthal angle φ (60~240°). Below part (5) are the ion getter pump and a titanium sublimation pump (TSP). The pumping station in part (5) includes a small turbo molecular pump and a membrane pump.

In this thesis, the chamber has been modified based on the chamber described in Ref. [84] for adopting a longitudinal and a polar MOKE setup. These are shown in Figure 2-19 as part (2) and the chamber next to the STM chamber in part (4), respectively. Because of the limitation in the chamber geometry, both MOKE setups could not be combined together. In the longitudinal MOKE setup, the sample is placed on the manipulator to avoid possible mechanical vibrations. The manipulator is placed between two electrodes of a big electromagnet which can be moved both forward and backward via a linear motion feedthrough. The optical parts are mounted onto two viewports and collimated in cage systems, as shown in Figure 2-20 (c). In the polar MOKE setup shown in Figure 2-19 (4), a T-motion is designed for a movable sample stage combined with a circular-shape electromagnet. The T-motion shown in Figure 2-20 (a) provides two degrees of freedom for the motion of the sample stage in the x and y directions. In one of the electrodes of the electromagnet, a small window is made for shooting the laser onto the sample surface in a perpendicular direction (with a few degrees flexibility). In Figure 2-20 (b), optical

components are mounted on an aluminum optical table beside a viewport on the opposite side of the T-motion flange.

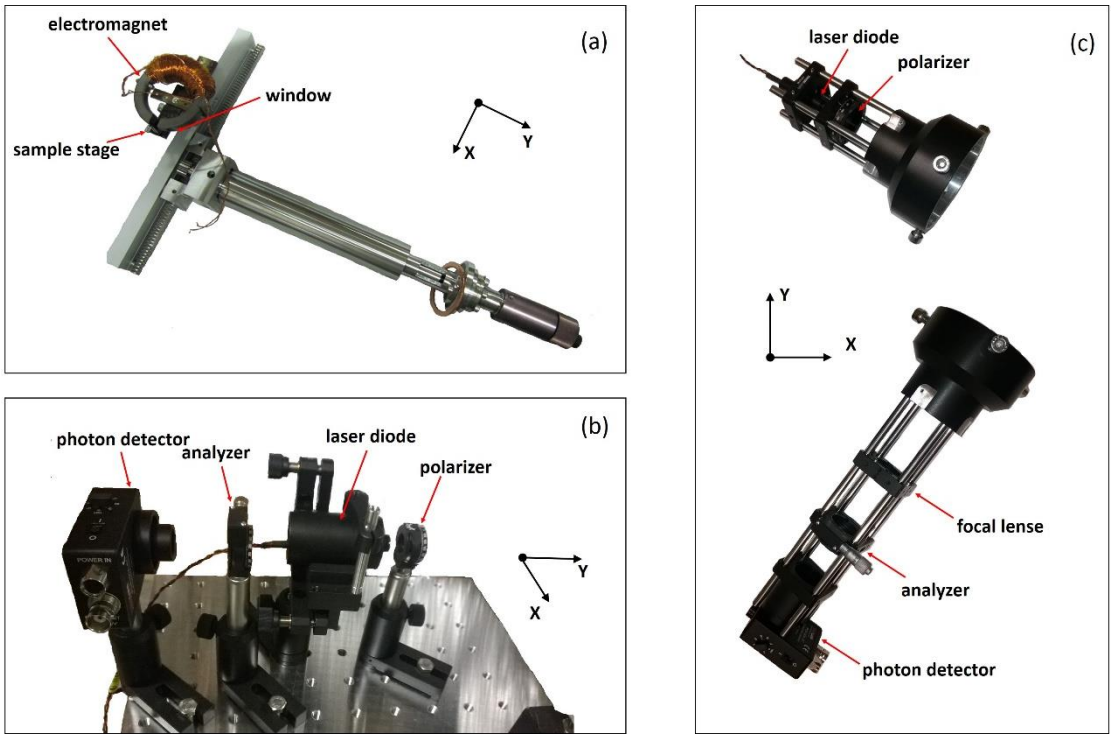

Figure 2-20 (a) A T-motion combined with an electromagnet and a sample stage. (b) Optical components for the polar MOKE setup. (c) Optical compnents in cage systems for longitudinal MOKE setup.

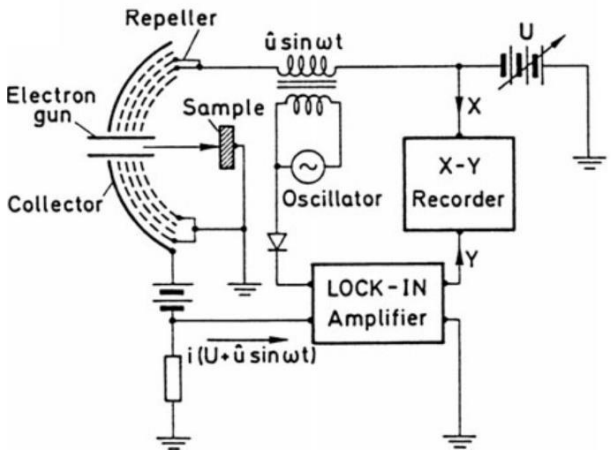

Figure 2-21 From Ref. [32]. Sketch of a four-grid LEED optics as a retarding field (RF) Auger electron energy analyzer. A screen is placed behind the four hemispherical grids (dashed lines) for collecting electrons.

In this work, a four-grid LEED optics are used for collecting Auger electrons emitted from the sample and for energy analyzing, as shown in Figure 2-21. The retarding voltage U determines the threshold energy of inelastic electrons reaching the collector. The current $i(U)$ reaching the collector is [32]

$$i(U) \propto \int_{eU}^{+\infty} N(E)dE \tag{2-25}$$

in which $N(E)$ is the energy distribution of collected electrons. The lock-in amplifier generates a small AC voltage modulation $u\sin\omega t$ applied to the repeller. For $u \ll U$, the current can be expanded in a Taylor series [32]

$$i(U + u\sin\omega t) = i(U) + i'(U)u\sin\omega t + \frac{1}{2}i''(U)u^2\sin^2\omega t + \cdots \tag{2-26}$$

in which the first harmonic signal corresponds to $N(E)$. The AES is an energy spectrum shown in a differentiated way of $N(E)$, i.e., $dN(E)/dE$, which is the second harmonic signal in equation (2-26). This term can be extracted by a phase-sensitive detection using a lock-in amplifier, giving rise to a magnified peak signal compared to the undifferentiated spectrum. A typical AES of a nickel substrate can be seen in Figure 2-22**.**

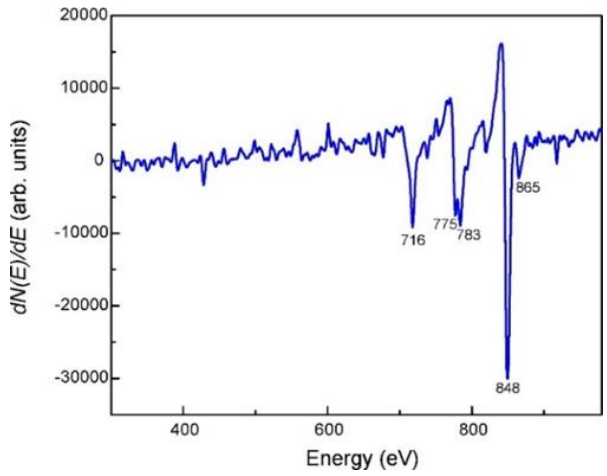

Figure 2-22 AES of a clean nickel single crystal at the primary electron energy of 3 keV. Differentiated Auger-electron-distribution peaks for nickel are marked by numbers in the spectrum.

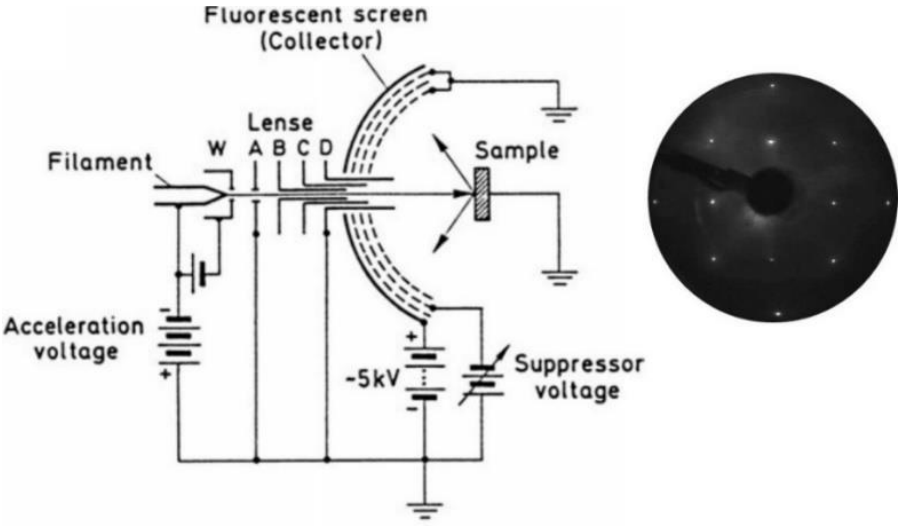

Figure 2-23 Sketch of a three-grid LEED setup (left panel, from Ref. [32]). The electron gun consists of a filament, a Wehnelt cylinder (W) and electron-static lenses (A-D). The voltages applied to B and C are between those applied to A and D. On the right panel, a typical LEED pattern for the Cu(001) surface at 219 eV is shown. Note that the LEED optics in this thesis is four-grid type and the screen voltage is -7 kV. Since the the same suppressor voltage is applied to the two grids in the middle as shown in Figure 2-21, the actual LEED setup in this thesis is equal to the three-grid type described here.

In a typical LEED setup, primary incident electron beams are perpendicular to the sample surface, as shown in Figure 2-23 (left). Since the diffracted electrons also have low energy, a bias is necessary to be applied to the screen for electrons to produce fluorescence. The obtained LEED pattern is analogous to a crosscut of these truncation rods by the fluorescent screen facing towards the sample surface, as an example shown in the right panel of Figure 2-23.

A closer look of the STM setup is shown in Figure 2-24. The setup is a room-temperature Omicron STM 1 which has a proven internal spring suspension system with eddy current (generated from the copper pates) damping for excellent vibration isolation. The STM stage can be lifted up or lowered down by the linear motion drive from below. The scanning probe and the sample on the STM stage are both aligned vertically. The standard tripod scanner enables a maximum scanning range of 200×200 nm^2 for each image.

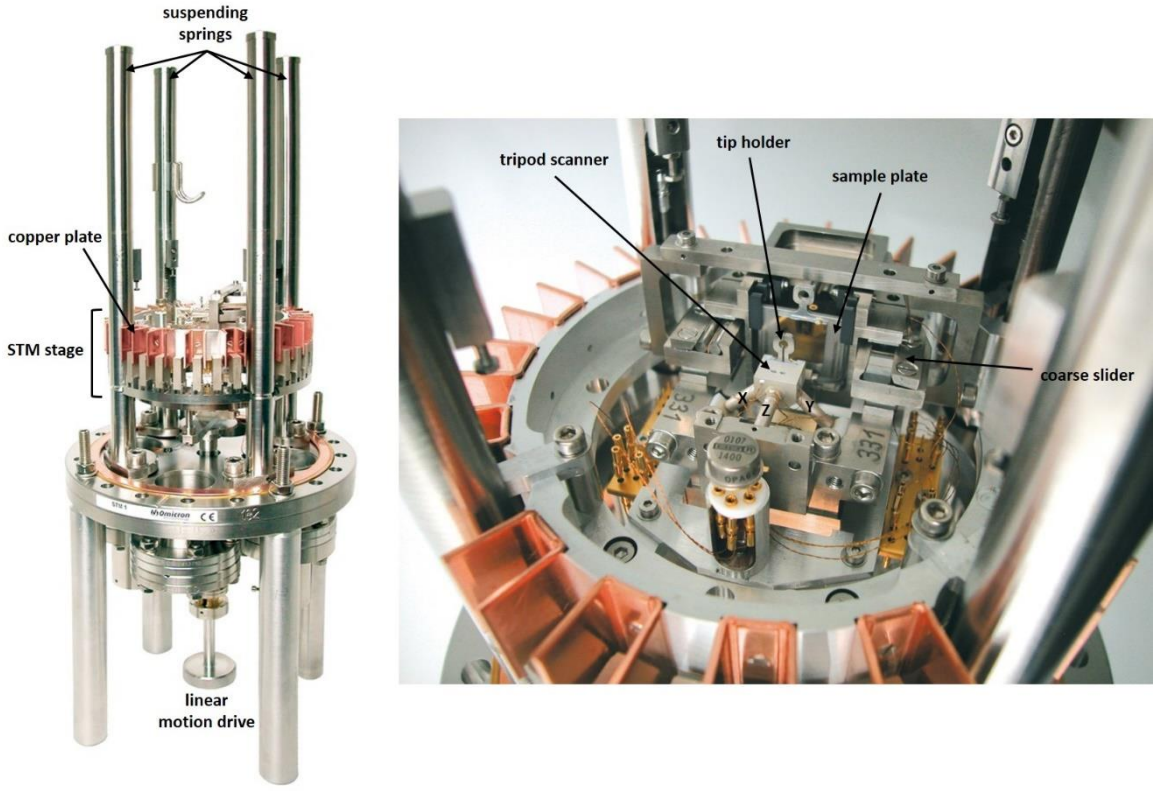

Figure 2-24 From Ref. [85]. Images of the UHV Omicron STM 1 (left panel) and the STM stage (right panel).

2.7.2 Sample preparation

The experiment was performed in a UHV chamber with a base pressure of 1×10^{-10} mbar. Disk-shaped Cu(001) and Ni(111) single crystals with a diameter of 10 mm were used as substrates. To achieve well-defined surfaces, the Cu(001) substrate was cleaned by cycles of Ar^+ sputtering with ion energy of 1 keV and subsequent annealing to 900 K for 30 min in UHV; the Ni(111) substrate was cleaned by cycles of Ar^+ sputtering with ion energy of 1 keV at 700~750 K, followed by subsequent annealing at 950 K for 20~30 minutes. The cleanliness and smoothness of the crystal surfaces were examined by AES, LEED, and STM. AES spectra for both crystals are shown in Figure 2-25. In both AES spectra, only the characteristic peaks for Cu and Ni are seen, as marked by energy values. The STM images shown in Figure 2-26 indicate smooth and defect-free surfaces for both crystals and sharp LEED patterns further confirm the good quality of the crystalline surfaces.

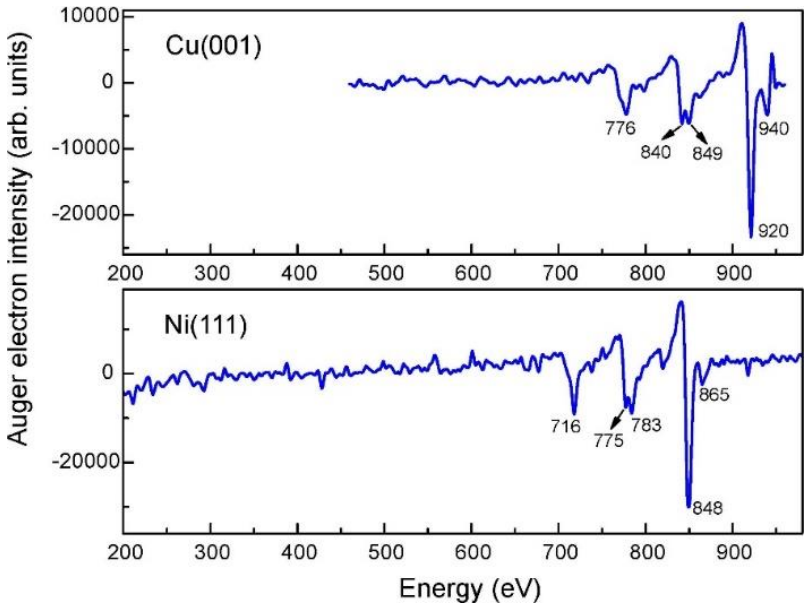

Figure 2-25 AES spectra of the Cu(001) (top panel) and Ni(111) (bottom panel) crystals.

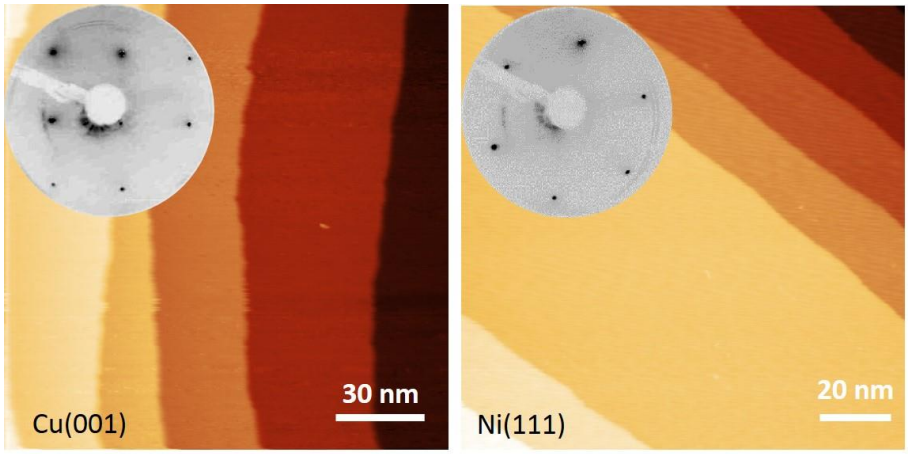

Figure 2-26 STM topography images of Cu(001) (left panel) and Ni(111) (right panel). Feedback parameters for Cu(001) and Ni(111) are 1.1 nA, +0.3 V and 1.3 nA, +0.8 V, respectively. The insets show the LEED patterns of both surface at an electron energy of 140 eV (for Cu) and 120 eV (for Ni).

During the sputtering process, the ion energy and incident angle can be controlled in an accurate way for creating nanostructured surfaces. Examples are shown in Figure 2-27. Due to different crystalline surface orientations for fcc Cu(001) and fcc Ni(111), the sputtered surface show diverse shapes of holes on the substrate terraces. The (001) surface exhibits square-like holes, while the (111) surface shows irregular shaped structures.

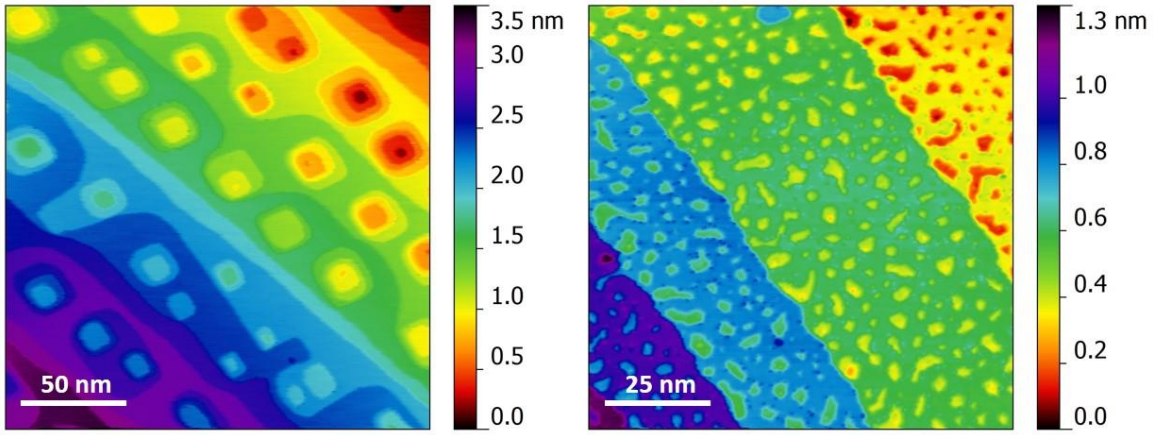

Figure 2-27 Nanostructured surfaces on Cu(001) (left panel) and Ni(111) (right panel) created by Ar^+ sputtering. The ion-beam incident angle with respect to the substrate surface is 38° and the ion energy 0.5 keV.

For the metallic thin film deposition, MBE technique was used. Cobalt (Co) and manganese (Mn) were evaporated while the sample was held at room temperature. Co was evaporated from a Co rod with a purity of 99.95%, which was bombarded with electrons, while Mn was evaporated by electron bombardment of Mn pieces with 99.95% purity in a molybdenum crucible. Since Co exhibits a coherent layer-by-layer growth mode on Cu(001) at room temperature [86,87], during Co evaporation, MEED was employed to monitor the evaporation rate from the intensity oscillations of the specular beam intensity. Afterwards, AES and STM were used for the more accurate Co thickness determination. The Mn thickness was calibrated by AES and STM. The graphene growth is performed in ultrahigh vacuum by chemical vapor deposition (CVD) on a single Ni(111) crystal. The carbon source are hydrocarbon molecules (ethylene or propylene). Detailed preparation recipes will be introduced in chapter 6. To explore the magnetic properties of the sample, *in-situ* longitudinal MOKE measurements were performed. A room temperature STM (Omicron 1) was used for the STM measurements. A lock-in amplifier [modulation voltage and frequency: 20 mV, 2.38 kHz] facilitates extracting the second-harmonic term of the signal and the differential conductance map can be obtained simultaneously with the constant-current topography during the scanning process. The scanning probe is a ferromagnetic Fe ring-shaped probe with an in-plane magnetic sensitivity [88], fitting to the expected in-plane magnetization direction of the system [89,90].

2.7.3 Iron ring probe preparation

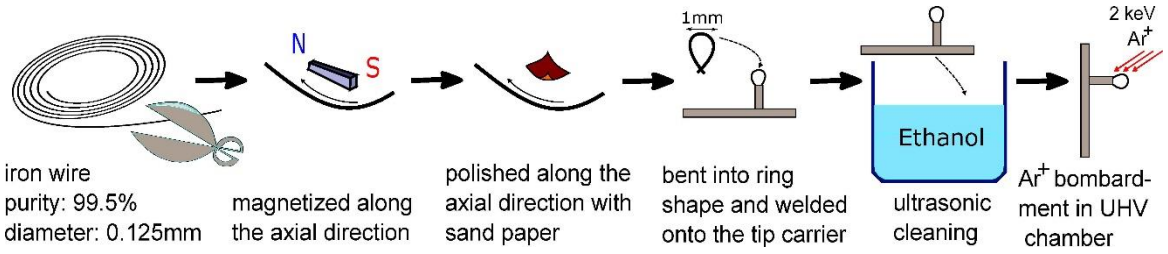

Figure 2-28 Schematic sketch of the fabrication and preparation process for a bulk-iron-ring probe.

The preparation of spin-polarized probes plays an important role in the implementation of spin-polarized scanning tunneling microscopy (Sp-STM) [75]. Compared with conventional preparation methods, the ring-shaped bulk Fe probes have the advantage of a well-controlled in-plane magnetization orientation due to shape anisotropy, and overcome the disadvantage of high stray fields of bulk ferromagnetic tips. Moreover, the design of the Fe ring probe simplifies the fabrication procedure of probes used in Sp-STM, and facilitates in-plane spin structure investigations [88]. As shown in Figure 2-28, following the recipe in Ref. [88], the Fe ring probes were prepared from an iron wire with diameter of 0.125 mm and purity of 99.5%, which was first magnetized along its axial direction with a permanent magnet and polished with sand paper, also along the axial direction. Then the iron wire was bent into 1 mm diameter ring, followed by ultrasonic cleaning and Ar^+ bombardment (ion energy of 2 keV) in the UHV chamber. Afterwards, the prepared probe is transferred to the STM stage and tested on a well-defined crystalline surface.

3 Electronic and magnetic properties of Mn on Co/Cu(001)

[Part of this chapter is from the publication *Phys. Rev. B* **91** 214406 (2015).]

3.1 Introduction

The AFM spin structure in low-dimensional systems has been drawing significant attention in the past decade [91–93,6,5,94,95]. For ultra-thin AFM films, because of the vanishing net magnetic moment, many fundamental magnetic properties are not easily probed directly. Not until the magnetic exchange anisotropy was discovered [3], the ferromagnetic/antiferromagnetic (FM/AFM) coupled systems have been harnessed for the exploration of the unique magnetic behavior of AFM layers. In nature, there are two kinds of single element AFM crystals, Cr and Mn. Since Mn displays diverse phases on different crystalline lattices under different conditions [96–101], the magnetic properties of ultra-thin films of this single-element metal epitaxially grown on FM substrates have been attracting more and more researchers to explore. Due to the strained and distorted lattice of the e-fct structure, Mn with this crystalline structure is metastable, nonetheless, it can be both structurally and magnetically stabilized when epitaxially grown on, for example, fct Co/Cu(001) [89,102]. In order to interpret the Mn AFM spin configurations in AFM/FM exchange-coupled systems, e-fct Mn/Co(001) became an AFM/FM model system because both metals are single elements and the pseudomorphic growth facilitates achieving a well-defined interface. According to an ab-initio study of e-fct Mn, a (001)-plane-confined $c(2\times2)$ compensated collinear spin structure was predicted [90]. Later on, a MOKE experiment showed no oscillation of the saturation Kerr ellipticity as a function of the Mn thickness [89]. The enlarged coercivity after Mn deposition further supported an in-plane compensated AFM spin configuration at the interface [89]. However, there is still no direct proof for the 2D collinear compensated spin structures. On the surface of low-dimensional

Mn films, because of the broken inversion symmetry, unique magnetic spin structures might be found different from the bulk. Sp-STM [103,104] facilitates exploring the surface Mn spin configuration in real space and provides a distinct tool to view the Mn surface even on the atomic scale [94,101,55,56,105]. The recent Sp-STM studies of AFM fct Mn on Co/Cu(001) at both low [106] and room temperatures [88] have imaged Mn surfaces on relatively large scales and indeed observed a layerwise contrast difference between successive Mn layers. The observed layerwise contrast of the Mn surface suggests an in-plane layerwise uncompensated AFM spin configuration and fits to the prediction of the AFM/FM exchange-coupled system with a collinear in-plane spin structure. However, the lateral resolution achieved in all previous studies did not allow conclusions on the atomic-scale Mn spin configuration, which still remains unknown.

In this chapter, different scales of STM spectroscopic contrasts are discussed for an interpretation of the Mn surface AFM spin configurations different from previous studies. The Sp-STM study here reproduced the layerwise contrast, but this contrast demonstrates a thickness-dependent behavior and coexists with a possible atomic-scale noncollinear spin texture that differs from the predicted 2D spin structures with collinear *c*(2×2) compensated [89,90] and in-plane uncompensated [88,106] AFM configurations. Measurements of epitaxial AFM e-fct Mn films by Sp-STM at room temperature are presented, using a bulk iron ring as spin-polarized scanning probe [88]. Due to shape anisotropy, the bulk iron ring senses the in-plane spin component of the Mn atoms along the ring plane. The observations point towards a dominating non-magnetic electronic origin of the STM spectroscopic layerwise contrast, possibly coexisting with a layered AFM spin configuration. Moreover, the high-resolution Sp-STM study reveals a (12×2) geometric reconstruction of the Mn surface as well as evidence for a noncollinear Mn surface spin structure, the presence of which is attributed to competing exchange interactions in the frustrated and reconstructed Mn film. Additionally, oxygen influence on the large-scale layerwise spectroscopy contrast and the possible electronic state modification of the Mn surface are also discussed.

3.2 Large-scale layerwise spectroscopic contrast on the Mn surface

3.2.1 Thickness-dependent layerwise contrast

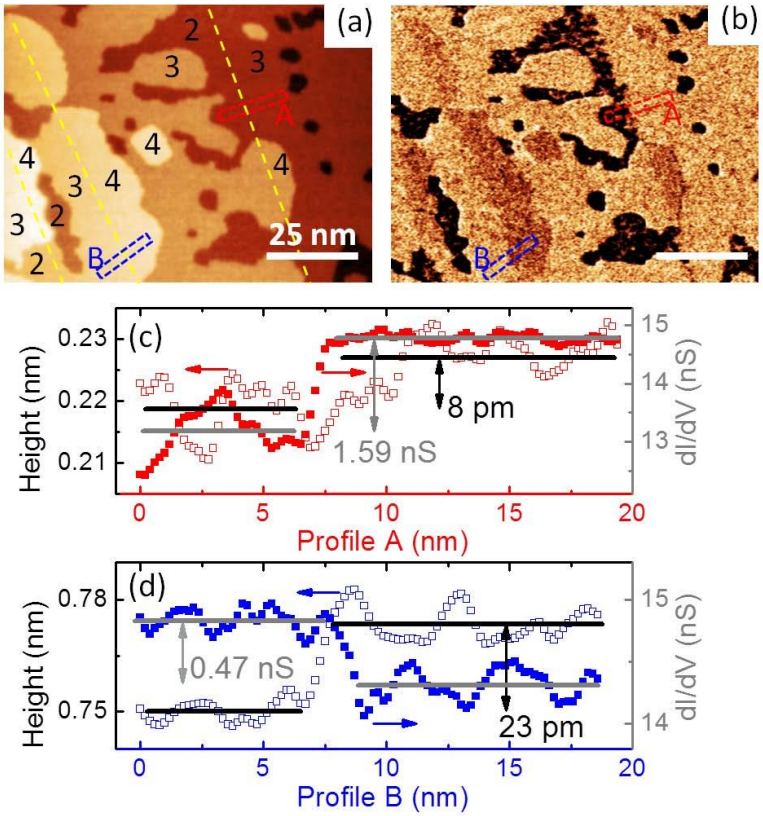

Figure 3-1 (a) Constant-current topography and (b) simultaneously recorded *dI/dV* map at sample bias +0.15 V, tunneling current 2.8 nA. Yellow dashed lines in (a) indicate overgrown Co steps underneath the Mn layer. Red and blue dashed rectangles mark areas where profiles have been taken from left to right, averaging pixels over the width of the rectangles. (c), (d) Plots of line profiles of A and B. Open and solid scattered symbols are from (a) and (b), respectively.

At room temperature, Mn exhibits a step-flow layer-by-layer growth mode above 1 ML thickness on the fct Co/Cu(001) surface [88,102,106]. Figure 3-1 (a) shows the topography of 3 ML Mn/4 ML Co/Cu(001) with three layers Mn (second, third, fourth) exposed, as indicated by numbers in some places. The Mn film thickness of 3 ML was determined by AES and the layer assignment was done according to AES and STM together. Yellow dashed lines schematically mark the overgrown Co step edges. Figure 3-1 (b) is the

corresponding differential conductance map recorded at the same time by a lock-in amplifier with a voltage modulation of 20 mV applied to the DC sample bias. In this *dI/dV* map, the Mn surface exhibits a clear three-level layerwise contrast with a very dark−bright−dark sequence on second, third, and fourth layers. On the same Mn terrace across the Co step edge underneath, the contrast reverses with one monolayer more overgrown Mn on the next Co step. Figure 3-1 (c) and (d) present line profiles A and B taken from both the topography image and the differential conductance map. In the topography image, on the same Mn terrace, both regions A and B show a larger height where Mn has overgrown a Co step edge due to the larger Mn vertical lattice constant compared to that of Co. However, the step heights between 2 and 3 ML Mn (A) and 3 and 4 ML Mn (B) appear differently. The step between layers 3 and 4 is about two times higher than that between 2 and 3. Though both values are close to the vertical interlayer distance difference between fct Mn and Co [106,107] and the slight deviation could be due to the accuracy of *z* piezo calibration, the 15 pm height difference between steps in profiles A and B cannot be explained by assuming the same electronic property of the different layers. From profiles of the differential conductance map we also learn that the contrast difference between 2 and 3 is about 3.4 times that between 3 and 4 layers. Considering that a magnetic STM probe is used, the extracted *dI/dV* signal cannot be interpreted alone by an in-plane layerwise AFM spin configuration of Mn [106,107].

3.2.2 Spectroscopy contrast reversal test

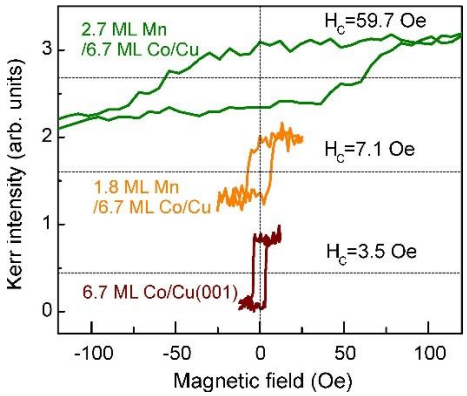

Figure 3-2 Hysteresis loops for 6.7 ML Co/Cu(001) (bottom), 1.8 ML Mn/6.7 ML Co/Cu(001) (middle), and 2.7 ML Mn/6.7 ML Co/Cu(001) (top).

In order to confirm that the thickness range for Mn with the observed layerwise contrast is above the critical thickness of Mn for AFM order at room temperature, *in-situ* longitudinal MOKE measurements is performed. The magnetic field was applied along the [110] in-plane easy axis of Co. Figure 3-2 shows hysteresis loops of 6.7 ML Co/Cu(001) without and with 1.8 ML and 2.7 ML Mn on top. Bare Co has a small coercivity of 3.5 Oe. When 1.8 ML Mn is deposited, the coercivity slightly increases to 7.1 Oe. However, after 2.7 ML Mn deposition, a pronounced enlargement of coercivity appears and the value reaches about 60 Oe, indicating AFM behavior of Mn at this thickness. The critical thickness for Mn on this 6.7 ML Co template should be between 1.8 ML and 2.7 ML, which is, at room temperature, close to Kohlhepp's result [108]. Although the interfacial Co roughness influences the Mn critical thickness, the critical thickness deviation between filled and half-filled Co layers appears to be less than 1 ML [35] and the Mn thicknesses discussed in this chapter should be above the critical thickness.

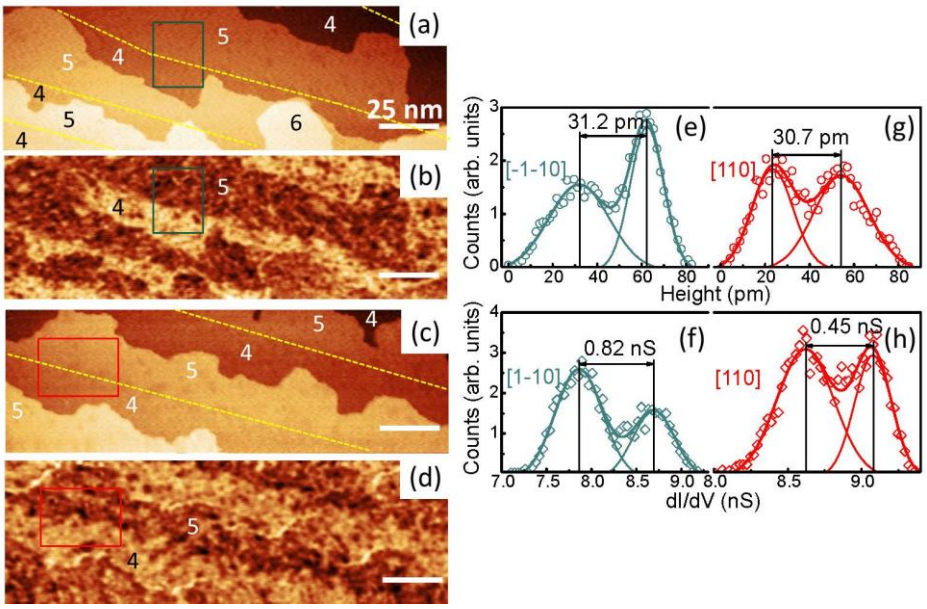

Figure 3-3 (a) (c) STM topography images of Mn on 5 ML Co/Cu(001) with fouth and fifth Mn layers exposed. Before Mn deposition, Co layers were magnetized along [-1-10] and [110] directions for (a) and (c), respectively. Yellow dashed lines indicate overgrown Co steps underneath. (b) (d) Simultaneously recorded *dI/dV* maps of (a) and (c). Feedback parameters: +0.2 V, 2.0 nA. Inset scale bars are 25 nm. (e), (f), (g), (h) are histograms for areas within rectangles in (a), (b), (c), (d), respectively.

According to the layered uncompensated AFM spin model for Mn [88,106], if the first ML FM Mn layer follows the Co magnetization direction [109,110], two oppositely magnetized Co layers with the same thickness of AFM Mn on top should give rise to opposite spin contrast with the same probe. Figure 3-3 (a) and (c) show topographic surfaces of the same thickness of Mn with oppositely magnetized FM Co underneath. The height difference between 4 and 5 ML Mn across the overgrown Co step on the same Mn terrace is almost the same, as shown by histograms in Figure 3-3 (e) and (g). Nevertheless, the *dI/dV* maps in Figure 3-3 (b) and (d) corresponding to the two Co magnetization directions exhibit different contrast levels, as shown in (f) and (h). The Mn differential conductance with [110] direction magnetized Co turns out to be about half of that with [-1-10]-direction magnetized Co underneath, however, no contrast reversal between the 4 and the 5 ML Mn occurs. From Figure 3-3 (b), it can also be seen that 5 and 6 ML Mn have almost the same contrast and the difference is too small to be clearly observed [to be discussed later].

As already discussed before in connection with Figure 3-1, spin contrast from an in-plane layered uncompensated AFM spin structure alone cannot explain the observed layerwise *dI/dV* contrast of the Mn surface. It should be concluded that there must be also a layer-dependent non-magnetic electronic contribution to the differential conductance maps. Nonetheless, a layerwise component of the AFM spin structure in Mn layers cannot be excluded, which could explain the different *dI/dV* contrast between 4 and 5 ML Mn layers in Figure 3-3 (b) and (d).

3.2.3 The influence of oxygen on the spectroscopic contrast of the Mn surface

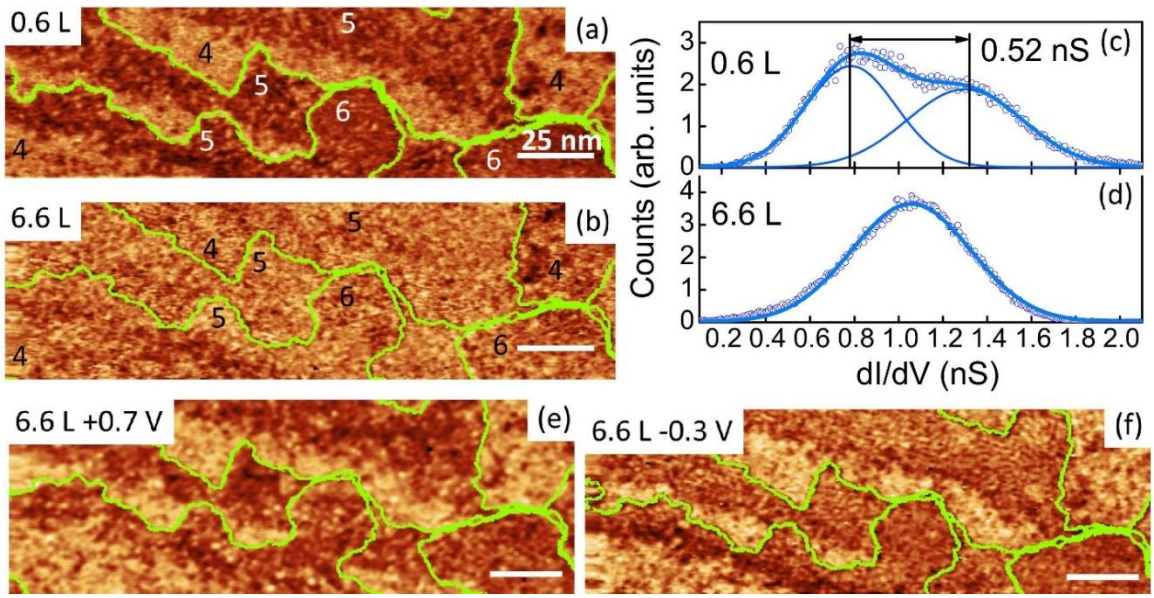

Figure 3-4 (a) (b) *dI/dV* maps of areas almost the same as in Figure 3-3 (a) with different oxygen dosage of 0.6 L and 6.6 L, respectively. Feedback parameters: +0.2 V, 2.0 nA. (c), (d) Histograms of (a), (b), respectively. Curves are horizontally shifted with the same span in *x* axis for better comparison. *x*-axis labels in (c) are the same as in (d). (e), (f) *dI/dV* maps of 6.6 L oxygen/Mn of almost the same area as in (a) at bias voltages of +0.7 V (e), -0.3 V (f), tunneling current 2.0 nA. Green curves illustrate Mn step edges. Inset scale bars in (a), (b), (e), (f) are 25 nm.

Mn is quite sensitive to oxygen and can be easily oxidized. The change of the Mn electronic state can thus in turn influence its magnetic properties. For example, according to an *x*-ray absorption spectroscopy (XAS) and *x*-ray magnetic circular dichroism (XMCD) study on FM 0.4 ML Mn on 3.0 ML Co/Cu(001), 5.5 L oxygen exposure changes the electronic configuration of Mn from the d^5+d^6 state to pure high-spin d^5 state, which reverses the Mn magnetic moment and forms an AFM coupling between MnO and Co [111]. In order to probe the oxygen influence on the large-scale layerwise contrast of the Mn surface, a quantitative study by exposing the Mn surface to different amounts of oxygen is performed. Figure 3-4 (a) and (b) present differential conductance maps of nearly the same areas as Figure 3-3 (a) after exposure to 0.6 L and 6.6 L oxygen, respectively. The oxygen exposure

has nearly no influence on the topography images. However, from the *dI/dV* maps, an obvious contrast change occurs after dosing only 0.6 L oxygen, as the histogram of Figure 3-4 (a) in Figure 3-4 (c) shows in comparison to Figure 3-3 (f). 0.6 L oxygen decrease the *dI/dV* contrast of the clean Mn surface by about 37%. Dosing another 6 L oxygen, the *dI/dV* contrast at +0.2 V bias voltage almost vanishes, shown in Figure 3-4 (d). Subsequently, LEED was performed and the clear diffraction pattern observed on clean Mn is now merged into the background after oxidation, indicating a fully oxidized Mn surface. Ref. [10] demonstrates that 5.5 L oxygen exposure on 0.4 ML Mn/Co/Cu(001) leads to MnO. Accordingly, here MnO should be the dominant phase on the surface. Although at +0.2 V, the Mn surface dosed with 6.6 L oxygen exhibits no distinguished spectroscopic contrast, by tuning the bias voltage the layerwise *dI/dV* contrast can still be observed, as illustrated in Figure 3-4 (e) and (f) for +0.7 V and -0.3 V bias voltages, respectively. This is consistent to STS measurements at different Mn thicknesses and will be discussed below.

3.2.4 Thickness-dependent scanning tunneling spectroscopy (STS) on clean and oxidized Mn surfaces

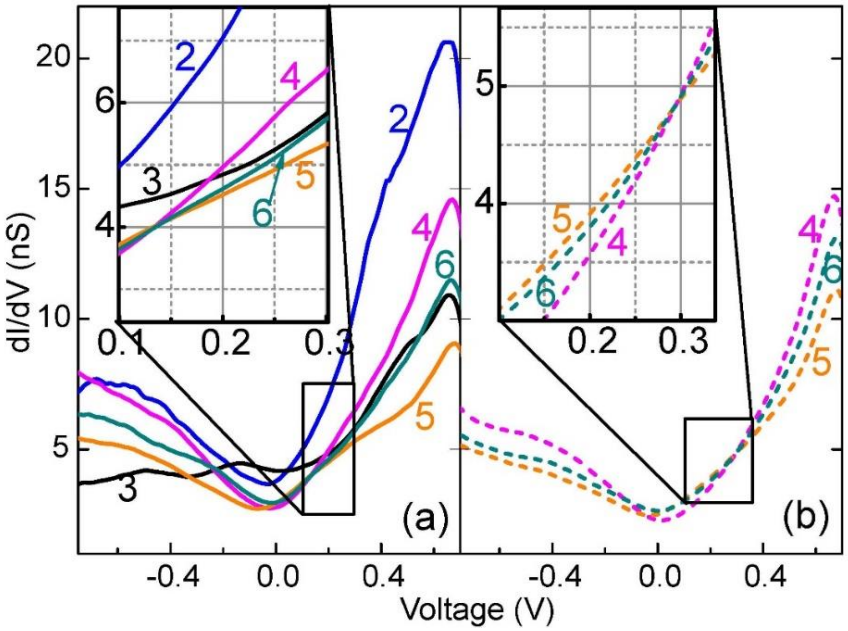

Figure 3-5 (a), (b) Thickness-dependent constant-current *dI/dV* spectra of Mn/Co/Cu(001) (solid lines) and 6.6 L oxygen/Mn/Co/Cu(001) (dashed lines) at different Mn thicknesses as indicated by numbers corresponding to atomic monolayers. Stabilization at +0.2 V sample bias, 2.0 nA tunneling current. The insets show magnified views of the same spectra.

Figure 3-5 (a) and (b) compare thickness-dependent STS curves of clean Mn and Mn dosed with 6.6 L oxygen. The STS curves for 2 and 3 ML Mn in Figure 3-5 (a) are from one sample which had not been exposed to oxygen later on and thus no curve for these two thicknesses is shown in Figure 3-5 (b). On clean Mn, at a bias voltage of +0.15 V, the differential conductance on layer 3, 4 and 2 has a decreasing tendency and the *dI/dV* difference between layer 2 and 3 is about 3.8 times of that between 3 and 4 layers, which is consistent to the discussion before in Figure 3-1. Ref. [106] shows that, at +0.6 V, 3 and 4 ML Mn exhibit dark and bright contrast, which matches our result in STS curves in Figure 3-5 (a). At +0.2 V, the STS contrast difference between 5 and 6 ML Mn demonstrates to be about 20% of that between 4 and 5 ML Mn.

The contrast vanishing point of 4, 5 and 6 ML Mn at +0.15 eV before oxygen dosing [Figure 3-5 (a)] shifts to +0.3 eV on MnO in Figure 3-5 (b). At +0.2 V, the *dI/dV* contrast in the STS curves on 4, 5, and 6 ML Mn gets reversed after oxidation. The differential conductance has a bias-dependent behavior and by comparing STS curves of Mn and MnO, we can see that the oxygen plays a significant role in modifying the LDOS of Mn. An ab-initio calculation for ultra-thin manganite films shows that the hybridized O 2*p* and Mn 3*d* states can both contribute significantly to the density of states at the Fermi level [112]. At negative bias voltages near E_F, electrons tunnel from occupied states of the sample to unoccupied states of the tip. When the O 2*p* and Mn 3*d* orbitals hybridize, electrons in MnO layers may become more localized compared to the itinerant electrons in clean Mn, such that for electrons tunneling from sample to tip, the tunneling conductance becomes smaller for MnO than for clean Mn for the same feedback parameters. As shown in Figure 3-4 (b), 6.6 L oxygen almost kill the *dI/dV* contrast at feedback parameters of +0.2 V, 2.0 nA, which means that after this oxygen exposure, the surface density of states of the exposed layers of different thickness becomes nearly identical at this energy. By tuning the tunneling electron energies, the difference between the LDOS at different MnO thicknesses becomes obvious, which could result from a different electronic structure on different layers of clean Mn. Moreover, since Mn atoms possess a large magnetic moment, the charge transfer may lead to the polarization of oxygen and change the Mn magnetic moment as well. Since the previous study on the oxygen influence has been conducted on the FM Mn surface [111], a quantitative study with other techniques on the oxygen influence on the AFM Mn spin moment could be an interesting topic in the future.

3.3 High-resolution contrast on the Mn surface

3.3.1 Stripe contrast

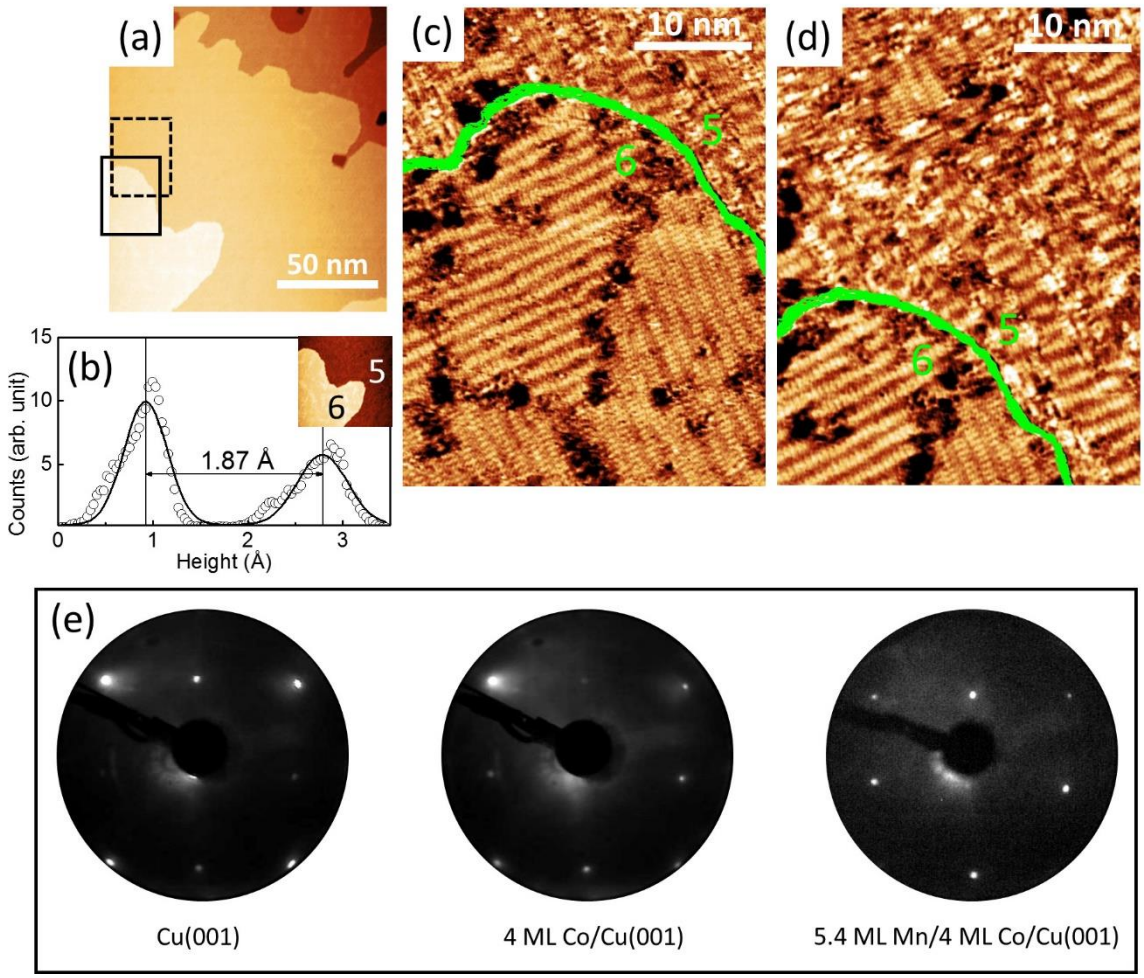

Figure 3-6 (a) Constant-current topography of the Mn surface (sample bias +0.2 V, tunneling current 2.5 nA). (b) Histogram of the a part of the topography image cropped from (a), as shown in the inset. (c), (d) Constant current *dI/dV* maps corresponding to areas marked with solid and dashed rectangles in (a), respectively (sample bias +0.2 V, tunneling current 10.5 nA). Green boundaries highlight the step edges between regions of 5 and 6 ML Mn thickness. (e) LEED patterns for Cu(001) (left), 4 ML Co/Cu(001) (middle), and 5.4 ML Mn/4 ML Co/Cu(001) (right) at 117.8 eV.

In order to further understand the AFM spin configuration of the e-fct Mn surface on the atomic scale, a 5.4 ML Mn film on 4.0 ML Co/Cu(001) was investigated. As seen in Figure

3-6 (a), only the fifth and the sixth ML Mn are exposed and the step height between two adjacent layers amounts to 1.87 Å according to the histogram of Figure 3-6 (b). This height is consistent with the vertical interlayer distance of the expanded face-centered tetragonal (e-fct) Mn on Co/Cu(001) [106,107]. The LEED pattern of this film is shown in the right of Figure 3-6 (e). Compared to the sharp $p(1\times1)$ spots on both clean Cu(001) and 4 ML Co/Cu(001), the Mn LEED image is also dominated by sharp $p(1\times1)$ spots at the same positions as those of the Co substrate, but the background intensity is somewhat enhanced. This suggests a dominating pseudomorphic growth of Mn on the fcc Co(001) template. However, indications of surface reconstructions for Mn/Co/Cu(001) have been observed before [107]. These reconstructions have been interpreted as being confined to the surface and not reflecting the major bulk structure.

Using the lock-in technique, local differential conductance maps was recorded simultaneously with the topography by the spin-polarized bulk Fe ring probe, which senses the in-plane-oriented surface magnetization expected for AFM Mn in this system [88]. Figure 3-6 (c) and (d) are differential conductance maps of the areas marked by solid and dashed rectangles in Figure 3-6 (a), mainly showing the exposed 6 ML and 5 ML Mn terraces, respectively. On both terraces, there exist domains with stripes oriented in two orthogonal directions. On the 6 ML terrace, as shown in Figure 3-6 (c), these stripes form larger ordered domains compared to the 5 ML terrace in (d). Similar domains with the same stripe features were also observed in other areas with Mn thicknesses of 5 ML and 6 ML. The 6 ML areas always contain longer-range-ordered stripes, whereas the 5 ML areas only possess some smaller striped domains mixed together with disordered areas.

3.3.2 (12×2) reconstructed e-fct Mn surface

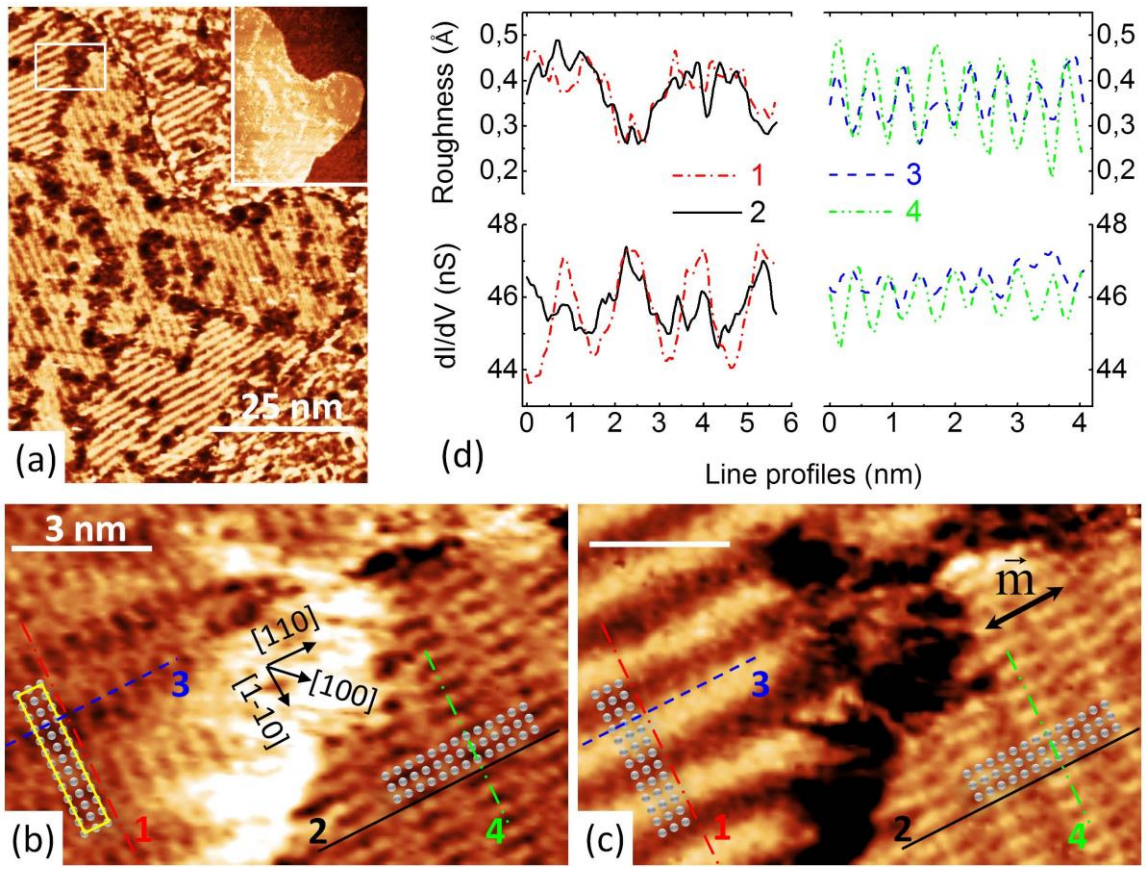

Figure 3-7 (a) Constant-current *dI/dV* map at 6 ML Mn thickness (sample bias +0.2 V, tunneling current 10.5 nA). The inset shows the corresponding simultaneously recorded topography image. (b), (c) High-resolution topography and *dI/dV* map of the area marked by a white rectangle in (a) (sample bias +0.2 V, tunneling current 10.5 nA). The black double-sided arrow in (c) shows the Fe ring orientation, the yellow rectangle in (b) indicates the unit cell of the (12×2) superstructure, and small white circles indicate the positions of Mn surface atoms. (d) Line profiles taken from (b) and (c). Line profiles 1, 2, 3 and 4 correspond to lines marked by the respective line styles and colors in (b) and (c). The line profiles from (b) are taken exactly at the same sample positions as those from (c).

Figure 3-7 (a) is a differential conductance map from a larger area of 6 ML Mn thickness with long-range-ordered stripe domains. The inset shows the corresponding topography image recorded during the same scan. In order to explore more detailed information about

the two orthogonally-oriented stripes, atomic-resolution scanning was performed on a typical area as marked by a white rectangle in Figure 3-7 (a). The high-resolution topography image and differential conductance map are shown in Figure 3-7 (b) and (c), respectively. In (b), a corrugated surface with two orthogonal domains in the left and the right part of the image is observed. Both show the same periodicity, as demonstrated by taking line profiles 1 and 2 for one direction, 3 and 4 for another direction. The corresponding profiles are illustrated in Figure 3-7 (d). Line profiles of the topography illustrate that the apparent surface corrugation amounts up to about 0.3 Å. According to the periodicity measured from profiles 1 and 3 (or 2 and 4), a (12×2) superstructure unit cell can be identified on the surface, as highlighted by the yellow rectangle in Figure 3-7 (b). The white circles represent the positions of Mn atoms within one unit cell.

While the topography of the two domains is virtually the same, just rotated by 90°, the differential conductance contrast shows notable differences. The left domain exhibits a different periodicity, as evidenced by the line profile 1 in Figure 3-7 (d). Line profile 1 (left area) in the *dI/dV* map has half the periodicity of line profile 2 (right area), and also half of the topographic periodicity of line profile 1. Moreover, in Figure 3-7 (c), the amplitude of profile 2 is not identical to profile 1, but about 20% less. It could be interpreted as the effect of spin contrast, where the orientation of the tip magnetization breaks the symmetry present in the topography image. The orientation of the iron ring probe is illustrated by the black arrow in the differential conductance map in Figure 3-7 (c). The magnetic moment of the apex atom is along the tangential direction of the ring. Since this magnetic moment has a larger component along the [110] direction, the contribution from spin contrast should be dominated by the spin component of Mn atoms along this direction.

The strong similarity of the (12×2) superstructure in the two 90°-rotated domains in the constant-current topography image [Figure 3-7 (b)] means that it is mainly of non-magnetic origin. It is plausible to assume that there is a corresponding geometric reconstruction of the Mn film. Vertically expanded pseudomorphic films often exhibit a geometric reconstruction and/or surface buckling [99,113–115]. This opens the question why no (12×2) superstructure is observed in the LEED image shown in the right of Figure 3-6 (e), just an enhanced background. A possible explanation could be the small size of structurally well-ordered domains that exhibit the (12×2) superstructure. Although the region imaged in Figure 3-6 and Figure 3-7 consists of domains somewhat larger than the transfer width

of the LEED system (typically 10 nm), this might not be the case in many of the other regions of the sample. In regions with 5 ML Mn thickness, the size of such domains is particularly small and overall, the fraction of large-ordered stripe domains could be relatively small compared to the fraction of the short-range-ordered and disordered domains.

3.3.3 Noncollinear spin structure simulation

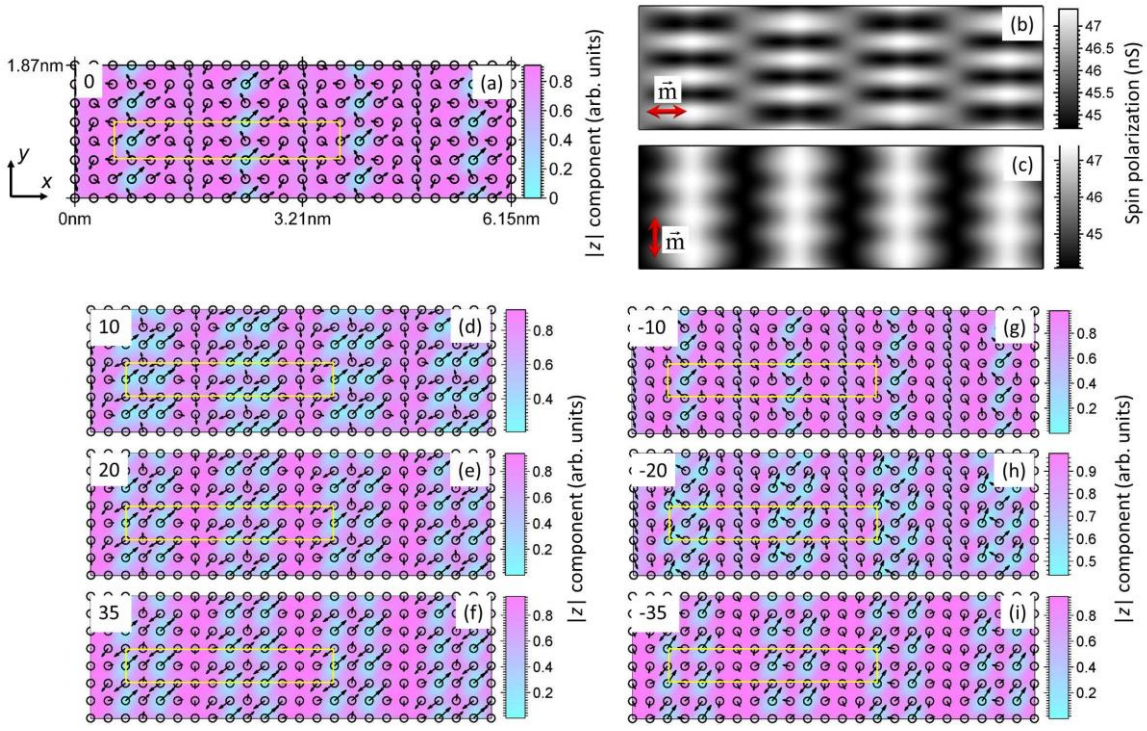

Figure 3-8 (a) Simulated noncollinear spin structure of the reconstructed Mn surface, assuming only spin contrast in the *dI/dV* maps. Black arrows show the orientation and absolute values of each atomic spin projected in the *xy* plane and the color bar on the right represents the absolute magnitude of the *z* components of spins (see text). Black circles represent Mn atomic sites. (b), (c) Smoothed and periodically extended experimental *dI/dV* maps obtained from the right and left parts of Figure 3-7 (c) (see text). Red arrows show the ring orientations. (d) – (i) Other possible noncollinear spin models for the Mn surface, assuming also nonmagnetic electronic contrast for the simulation (see text). The numbers on the top-left corners of images for noncollinear spin models illustrate different weighting factors (unit: nS/nm) for non-magnetic contributions.

In order to interpret this contrast difference between the two orthogonally-oriented domains in the differential conductance maps of Figure 3-7, models for the spin structure of the reconstructed Mn surface are extracted. The experimental data for one unit cell of the right and left domain of Figure 3-7 (c) is smoothened on the lengthscale of atomic distances, averaged over a few unit cells, and a zero line is set such that the average *dI/dV* contrast is zero. The resulting contrast maps are shown in Figure 3-8 (b) and (c), which then represent the average experimental *dI/dV* signal for an *x*- and *y*-aligned tip, respectively. The red double-sided arrows indicate the directions of spin sensitivity. As in the experiment [see line profiles 1 and 2 in the bottom of Figure 3-7 (d)], the maximum amplitude of the spin polarization projected on the *x* direction [Figure 3-8 (b)] is about 20% lower than in the *y* projection [Figure 3-8 (c)]. Before proceeding further, it has to be considered that in addition to a spin-polarized contribution to the *dI/dV* signal, there might be also a non-spin-polarized one, arising from the geometric (12×2) reconstruction. This non-magnetic contribution should be independent of the tip orientation. This non-magnetic contribution is approximated by the experimental contrast of the constant-current topography image. The topography signal from the right-hand side of Figure 3-7 (b) was smoothed in the same way as described above. Depending on the weighting factor (unit: nS/nm) that describes the weight of the non-magnetic contribution, different spin structures can be extracted from the experimental data. The relationship between the *dI/dV* map, spin signal, and electronic effect could be described as: *dI/dV* map = spin + electronic effect (non-magnetic). The contrast of Figure 3-8 (b) and (c) was taken and reduced by the non-magnetic contrast, as proportional to the *x* and *y* component of the atomic spins, as it is usually assumed in spin-polarized tunneling [55,75,91]. Hereby the decay of the spin polarization into the vacuum is assumed to be equal for both spin directions. To extract also the absolute value of the *z* component, it is assumed that the absolute values of all atomic spins are equal and assign zero *z* component to the largest in-plane spin. Setting now the non-magnetic contribution to zero, i.e., assuming spin-polarized tunneling as the sole source of the observed *dI/dV* contrast, leads to the spin structure shown in Figure 3-8 (a). It shows an area in the *xy* plane with a size of 61.5 Å×18.7 Å. In this simulated map, the yellow rectangle marks the (12×2) unit cell, and black circles represent sites of Mn atoms. A noncollinear spin structure is obtained, as presented by arrows, which show the projection of the atomic spin moments on the *xy* plane. The color bar on the right indicates the absolute value of the *z* component of the spins. In this spin structure, the averaged in-plane spin moment within one unit cell

is zero, i.e., all spins compensate in the *xy* plane if summed up. The sign of the *z* component is undetermined. One could assume a checkerboard-like arrangement of the sign of the *z* component in order to have the relative orientation of the spins of neighboring atoms closer to 180°.

In Figure 3-8 (d) – (i), other possible models for the spin structure of the Mn surface are exemplarily presented. In Figure 3-8 (d), (g), (h), (i), many neighboring spins are close to parallel alignment, which is not so likely for Mn, making these spin structures less plausible than the ones shown in Figure 3-8 (a), (e), or (f). Note that, while the models presented here have a compensated spin structure in the *xy* plane, experimentally a superimposed constant spin component cannot be excluded neither along *x* nor *y*. The Mn spin structure in such a case would be compensated only when the Mn layers underneath are included. The spin arrangement of deeper Mn layers, however, is not accessible by the technique used here.

Often the DMI [50–52] is the reason for noncollinear spin structures [55,56,105,116,117]. However, in the low-*Z* materials considered here and, in particular, for Mn with its half-filled 3*d* shell, DMI is not expected to play a major role. Thus competing and frustrated Mn-Mn antiferromagnetic exchange interactions in the reconstructed Mn film are mainly responsible for the observed noncollinear spin configuration at room temperature.

3.4 Co segregation phenomenon

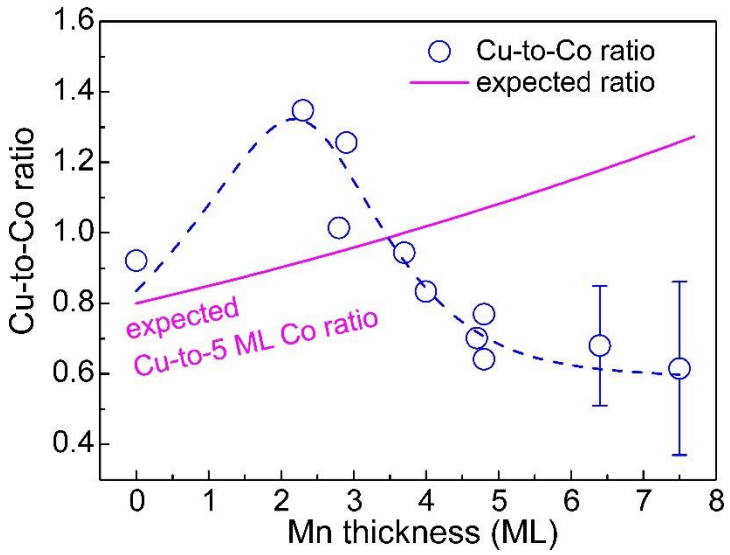

Figure 3-9 Cu-to-Co ratio of Auger electron $dN(E)/dE$ intensities of Mn/5 ML Co/Cu(001) as a function of Mn thickness. Cu and Co peaks in the spectra at electron energies of 920 eV and 716 eV, respectively, were used. Open circles represent experimental Cu-to-Co ratios, the solid curve shows the trend expected from the inelastic mean free paths of Cu and Co Auger electrons, the dashed curve is a guide to the eye. Error bars increase at higher Mn overlayer thicknesses as indicated, due to low signal.

As already mentioned before in connection with Figure 3-6 and Figure 3-7, there are less long-range-ordered stripe domains with similar periodicity in 5-ML-thick areas of the Mn film compared to 6 ML Mn. A possible explanation comes from AES. Figure 3-9 shows the Cu-to-Co ratios of AES intensities of Mn/Co/Cu(001) as a function of Mn thickness for different sample preparations where the Co thickness was always 5.0 ± 0.2 ML. The data points marked by open circles represent the Cu-to-Co peak ratios from AES for room-temperature preparation of Mn. Since the Cu Auger electrons have a longer IMFP due to their higher kinetic energy (920 eV) compared to Co Auger electrons (716 eV), the Cu signal is less attenuated by overlayers, and the Cu-to-Co peak ratio is supposed to increase with increasing Mn overlayer thickness. Assuming IMFP lengths of 5.45 and 4.1 ML for Cu and Co, respectively [83], an increasing curve like the solid line in Figure 3-9 would be expected, whereas the experimental data for room-temperature deposition of Mn show a clearly decreasing trend. This could be a hint towards a certain amount of Co segregation

into the initial capping Mn atomic layers during room-temperature deposition. Accordingly, there should be more segregated Co atoms at the surface of 5 ML Mn than at 6 ML. These Co atoms could act as defects on the surface and form boundaries to isolate the stripe domains or lead to an even more complicated spin configuration, which would explain why the order of the stripe-like reconstruction is more disturbed in 5-ML areas of the Mn film compared to 6 ML.

For the large-scale layerwise contrast, since it is dominated by electronic contribution, the thickness-dependent STS in Figure 3-5 (a) could be also due to Co segregation into the Mn layers [118]. Since e-fct Mn is metastable and different reconstructions may occur in different thickness ranges [107,118], these segregated Co atoms may assist to vary the Mn lattice slightly. According to different Co segregation ratios, the Mn crystalline lattice may demonstrate a slight layer-by-layer difference which could not be sensed by the previously applied methods [89,107]. However, by STM deeper layers under the surface cannot be explored. Nevertheless, it can be concluded that a layer-dependent non-magnetic contribution to the spectroscopic contrast is the main reason for the layerwise contrast observed in spin-dependent STM experiments of Mn/Co/Cu(001).

3.5 Extinction of the layerwise contrast on the 180-K-prepared Mn surface

As it is already known, at room temperature the Co-segregation-caused electronic contribution dominates the layerwise contrast on Mn surface. If there were no or just few amount of segregated Co atoms in the Mn film, the layerwise *dI/dV* contrast would be too weak to see. To further confirm this scenario, Mn films with thicknesses of 1.4 ML, 3.6 ML, and 5.5 ML were deposited at 180 K after 5 ML Co/Cu(001) as template were prepared at room temperature. Figure 3-10 (a), (b), (c) show topography images of Mn films with different thicknesses. The Mn growth at 180 K still retains a layer-by-layer growth mode. Differently from room-temperature-prepared Mn films, the low-temperature preparation leads to more islands scattered on the surface. In the simultaneously recorded *dI/dV* maps, no layerwise contrast is seen, as Figure 3-10 (d), (e), (f) illustrate. The probe has been tested before and after scanning on the low-temperature-prepared samples by STM in connection with a lock-in and the probe condition is stable enough to observe a layerwise *dI/dV* contrast. Since the mobility of Mn atoms at low temperatures can be drastically lowered compared

to room temperature, the Co segregation could be effectively reduced when Mn was deposited at 180 K. Accordingly, the layerwise contrast vanishes as expected, which further proves the electronic-dominating layerwise contrast observed in this chapter before.

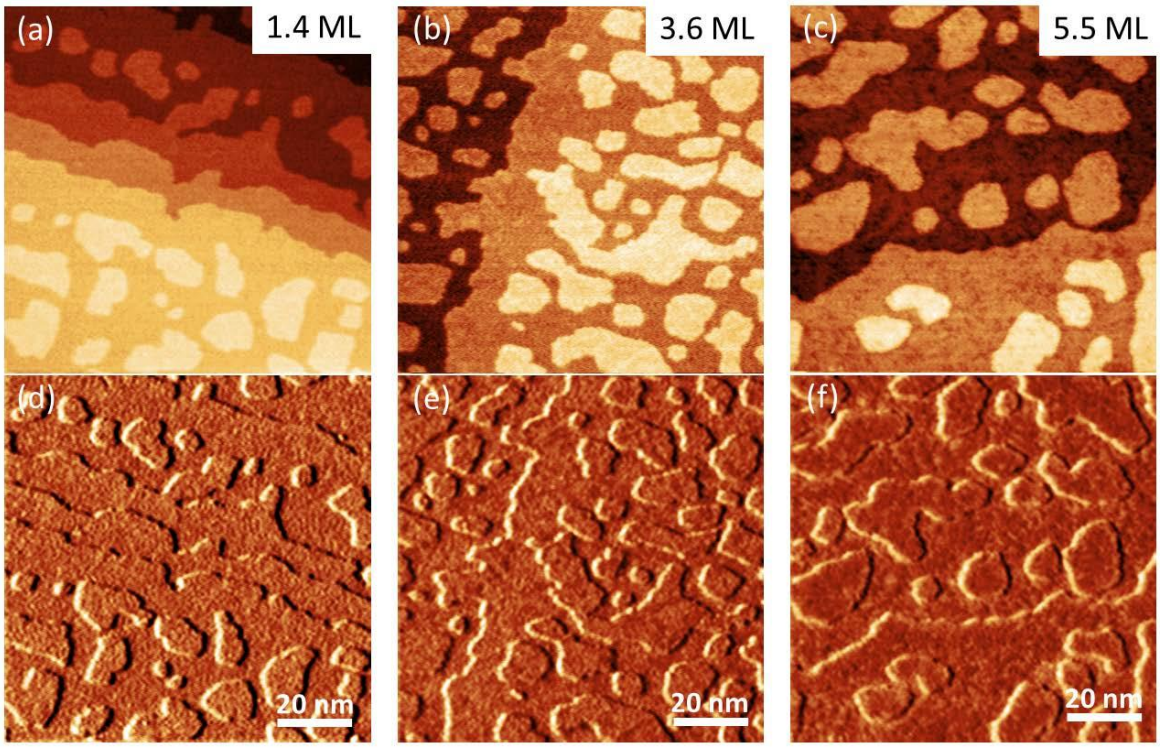

Figure 3-10 (a), (b), (c) Constant-current STM topography images for 180-K-deposited Mn on room-temperature-deposited 5 ML Co/Cu(001). (d), (e), (f) Simultaneously recorded *dI/dV* maps for (a), (b), (c), respectively. STM measurements were performed at room temperature. Feedback parameters: +0.2 V, 2.1 nA.

3.6 Connection of spectroscopic contrasts on different length scales

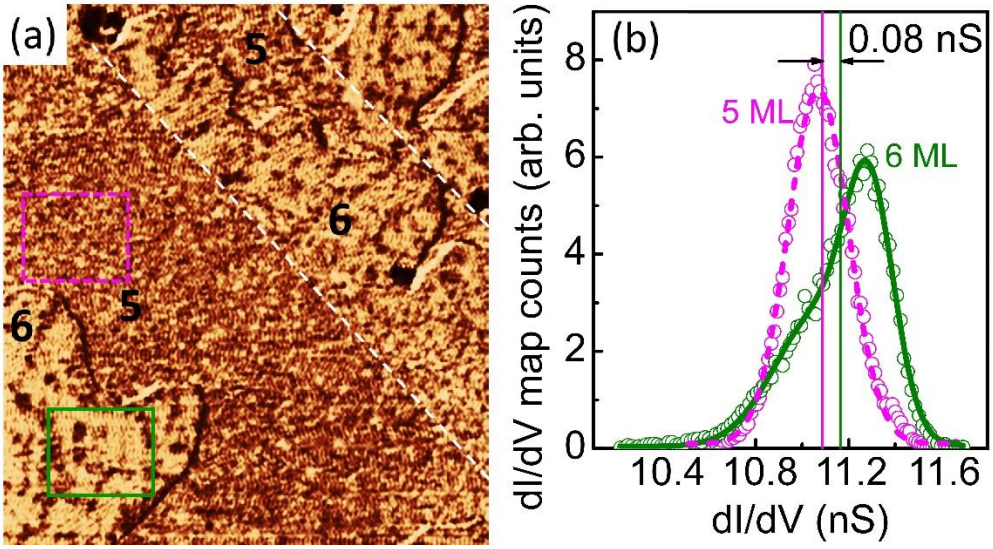

Figure 3-11 (a) Simultaneously recorded *dI/dV* map for Figure 3-6 (a) at constant current mode, sample bias +0.2 V, tunneling current 2.5 nA. The dashed white line illustrates steps at the surface of the Co film underneath. (b) Histograms for the two areas at 5 and 6 ML Mn film thickness, respectively, marked by rectangles in Figure 3-11 (a). Vertical solid lines show average values within the two rectangular areas, respectively.

On a larger scale, a layerwise contrast in *dI/dV* maps of Mn/Co/Cu(001) have been previously observed [88]. This could be also observed on the sample shown in Figure 3-11 (a), which presents a differential conductance map of the same position as shown in Figure 3-6 (c) and (d) with the same bias voltage, but different feedback parameters. Regions with 6 ML Mn appear clearly brighter than those of 5 ML. The dashed white line approximately marks step edges of the Co film underneath. On the same Mn terrace, across a Co step, the contrast changes where the Mn thickness increases from 5 to 6 ML. The two histograms in Figure 3-11 (b), taken in regions of 5 and 6 ML Mn thickness as indicated by the corresponding rectangles in Figure 3-11 (a), illustrate an average 0.08 nS contrast difference and is consistent to the STS contrast level between 5 and 6 ML in Figure 3-5 (a). The relative contrast is thus about a factor 10 smaller than the atomic-scale *dI/dV* contrast in Figure 3-6 and Figure 3-7, and thus difficult to see there. While the histogram for 5 ML Mn shows a symmetric shape with a certain width, the histogram for 6 ML Mn is

asymmetric with a peak at higher contrasts and a tail to darker contrasts. This is due to the different lengthscales of the ordered domains of reconstruction at 5 and 6 ML local Mn thicknesses. While in regions of 6 ML Mn thickness a bright contrast with dark lines in between is still recognized at the lower lateral resolution of Figure 3-11 (a), the grayscale of regions of 5 ML Mn thickness is perceived as the average of very small bright and dark areas.

The simulation of Figure 3-8 (a) for the Mn surface spin structure would be compatible with a fully compensated spin configuration. The layerwise large-scale contrast has proven to be quite reproducible in this research. For a fully compensated spin structure, it would need to be explained by an electronic contrast due to a different degree of Co segregation in the fifth and sixth atomic Mn layer from the Co-Mn interface. A possible scenario could thus be that the larger Co segregation into the fifth Mn layer results in smaller domains of the stripe structure, and thus the average *dI/dV* contrast, as seen at lower resolution, includes both domains and disordered regions, while in the sixth Mn layer, domains are larger and the black regions are still distinguished also at the lower resolution of Figure 3-11 (a). However, as discussed before, a superimposed layerwise uncompensated spin component in the *xy* plane aligned by the magnetization direction of the Co layer cannot be excluded.

3.7 Summary

The spectroscopic contrast of the e-fct Mn surface on Co/Cu(001) on different lengthscales has been investigated by Sp-STM. The *dI/dV* signal is different for each thickness of the Mn layer up to 6 ML. This thickness-dependent large-scale spectroscopy contrast between successive Mn-layer thicknesses becomes weaker for increasing Mn thickness and proves to be mainly of electronic origin. Co segregation is suggested as the origin of the layer-dependent electronic properties. However, an uncompensated layered AFM spin component cannot be ruled out. On the atomic scale, there exists a geometric superstructure with a (12×2) periodicity in two types of mutually orthogonal domains on the Mn surface. The simultaneously observed differential conductance maps reveal a noncollinearity of the Mn surface spin structure at room temperature. Simple models of layerwise Mn surface spin structures can simulate the experimental data and present possible spin configurations of the atomic-scale AFM spin structure. Co segregation may also influence the size of the reconstructed domains. The layerwise spin structure of Mn is attributed to competing AFM

exchange interactions in the frustrated and reconstructed Mn layer. The large-scale layerwise contrast is interpreted to be independent of the contrast from the atomic-scale layerwise spin structure. These two types of spectroscopy contrast on different scales are related to the lateral resolution of the image and tip-sample distances.

Oxygen plays an important role in tuning the layerwise contrast, indicating a modification of Mn LDOS by oxygen, possibly accompanied with a change of the Mn magnetic moment.

4 Characterization of Mn on Cu(001) and the interface modification

4.1 Introduction

Lots of interesting magnetic phenomena are expected in 2D structures like surfaces and interfaces. Ultrathin magnetic films, because of the reduced dimensionality, exhibit distinguished magnetic response changes with respect to the bulk [119–121] and the morphology of such thin films can influence the magnetic properties significantly [122–125]. The 3*d* transition metal Mn has drawn much attention in ultra-thin magnetic film research in the last decades, not only because of its large atomic magnetic moment from the half-filled *d* orbital, but also due to the diversity of phases when epitaxially grown on different substrates [99,126–133]. Sub-ML-thickness Mn epitaxially grown on Cu(001) has been investigated since more than twenty years ago [99,126,134–136] and Mn atoms in the ordered 2D MnCu surface alloy demonstrate unique magnetic behavior [113,121,137–140]. Besides sub-ML-thin Mn, there exist also studies on thick Mn films grown on Cu(001). Flores *et al.* found that there was no layer-by-layer growth for Mn below 270 K and attributed it to disorder caused by high-strain in thicker films [126]. Egelhoff *et al.* investigated the same system below 77 K. According to an intensity oscillation in reflection high-energy electron diffraction (RHEED), they found a layer-by-layer growth up to 4 ML [141]. However, no room-temperature growth of thick Mn films on Cu(001) has been reported yet.

In this chapter, room-temperature-deposited thin and thick Mn films are investigated by STM and LEED. For thick Mn films, because the growth no longer retains a layer-by-layer mode, ways for modifying the growth to be a 2D mode will be discussed in the following sections.

4.2 Growth of Mn/Cu(001) at room temperature

This section gives an overview of Mn growth on a Cu(001) substrate at room temperature. For a Mn thickness below 1 ML, the growth mode turns out to be 2D, as Figure 4-1 (a) and (e) show. At a coverage less than half ML, round-shaped islands are observed. The LEED pattern for 0.2 ML island coverage shows a clear *c*(2×2) superstructure, as red circles indicate in Figure 4-1 (b). This *c*(2×2) superstructure is due to the formation of a 2D ordered surface alloy of MnCu and is not caused by the Mn overlayer on the surface, which has already been confirmed by previous studies [98,99]. The *c*(2×2) superstructure appears at a Mn coverage less than 0.5 ML here, different from Ref. [98] that claims that the *c*(2×2) superstructure appears only at Mn coverage above half a ML. For lower coverages [< 0.5 ML], only *p*(1×1) patches and disordered areas have been found in Ref.[98]. In Figure 4-1 (a), the coverage of the round-shaped islands amounts to 0.2 ML statistically. These islands could consist of MnCu alloy, where the Cu atoms originate from replacement by Mn. According to Ref. [134], annealing at 340 K could lead to the disappearance of these islands and cause them to diffuse to the step edges. At room temperature, in the step edge areas, Mn atoms could also incorporate into the step edges, thus not forming individual islands [134]. The presence of some step-area MnCu alloy could also be taken into account for the *c*(2×2) superstructure. The actual Mn coverage could thus be higher than 0.2 ML in Figure 4-1 (a). According to Ref. [136], when Mn atoms reach the Cu(001) surface, they incorporate directly into the substrate and exchange with Cu atoms. The following diffusion process of these incorporated Mn atoms is driven by vacancies at the surface and the diffusion coefficient does not depend only depend on temperature, but also on the coverage. Higher temperature leads to a rise of the vacancy-mediated diffusion motion of incorporated Mn atoms and shorten the time for achieving a homogeneous Mn distribution. More importantly here, the mobility of these incorporated Mn atoms has a coverage-dependent behavior that determines the order of the surface alloy at different coverages, which essentially comes from the Mn nearest-neighbor repulsive interactions over short distances [136]. Lower coverages give rise to long Mn−Mn mean distances and low mobility, thus a disordered alloy is more favored and in the LEED image, only a *p*(1×1) pattern from the substrate can be seen[98]. When increasing the coverage, the mobility becomes larger and at a certain intermediate coverage, the diffusion coefficient of the incorporated Mn atoms could be strongly enhanced such that the Mn−Mn mean distance is

maximized for this coverage, and the incorporated atoms' mobility again becomes low, forming the ordered *c*(2×2) alloy which exists only in the surface [113]. Refs. [134,136] suggest an intermediate coverage of 0.3 ML at which ordered alloying starts and this coverage might approximate the actual amount of Mn in Figure 4-1 (a) [actual coverage > 0.2 ML]. This explains the observation of the ordered *c*(2×2) superstructure for the MnCu alloy. In a word, factors, such as temperature, time after sample preparation, actual deposition rate, surface vacancy concentration, and so forth, may vary the Mn diffusion motion and in turn influence the order of the surface alloy [136]. Specific alloying order should depend on the actual environment in the experiment.

Figure 4-1 (e) shows a surface with an island coverage of 0.7 ML on Cu(001) and (f) is the corresponding LEED pattern, which shows a different superstructure compared to *c*(2×2). Since the MnCu *c*(2×2) alloy only exists on the surface [113], after the surface is fully covered by the *c*(2×2) MnCu alloy (50% Mn and 50 % Cu), in principle, areas with and without islands should be of the same configuration. Namely, no MnCu *c*(2×2) alloying phase is expected in the layer underneath islands. The later deposited Mn atoms [red dots without green circles in Figure 4-1 (h)] could also exchange with Cu atoms in the MnCu alloy and further increase the surface Mn concentration. Comparing the experimental and simulated *p*(2×1) [plotted together with *p*(1×2)] LEED patterns in Figure 4-1 (f) and (g), it is easy to find that (f) has extra spots at the *c*(2×2) sites. If simply superimpose Figure 4-1 (c) and (g) together, the pattern will perfectly match the experimental result in Figure 4-1 (f), which possibly indicates a coexistence of three different domains with *c*(2×2), *p*(2×1), and *p*(1×2) alloying phases on island coverage of 0.7 ML on the surface.

When the Mn coverage exceeds 1 ML, the growth mode changes into the Stranski-Krastanov (SK) growth [142] and the surface roughness increases with the deposited amount of Mn, as Figure 4-1 (j), (k), (m) illustrate. The corresponding LEED patterns get more and more diffuse for higher coverages, and Cu atoms might be immiscible with Mn in the thick disordered adlayer. In this high coverage range, the Mn mobility could be much lower and the diffusion coefficient smaller compared to the sub ML, which makes it difficult to maintain an ordered phase of alloy at the surface. From the topographies with more than 1 ML Mn coverage in Figure 4-1, it can be concluded that the ordered-MnCu-surface alloy cannot structurally stabilize the subsequently overgrown Mn film and a 2D structure can hardly be achieved at room temperature for thick Mn films on Cu(001).

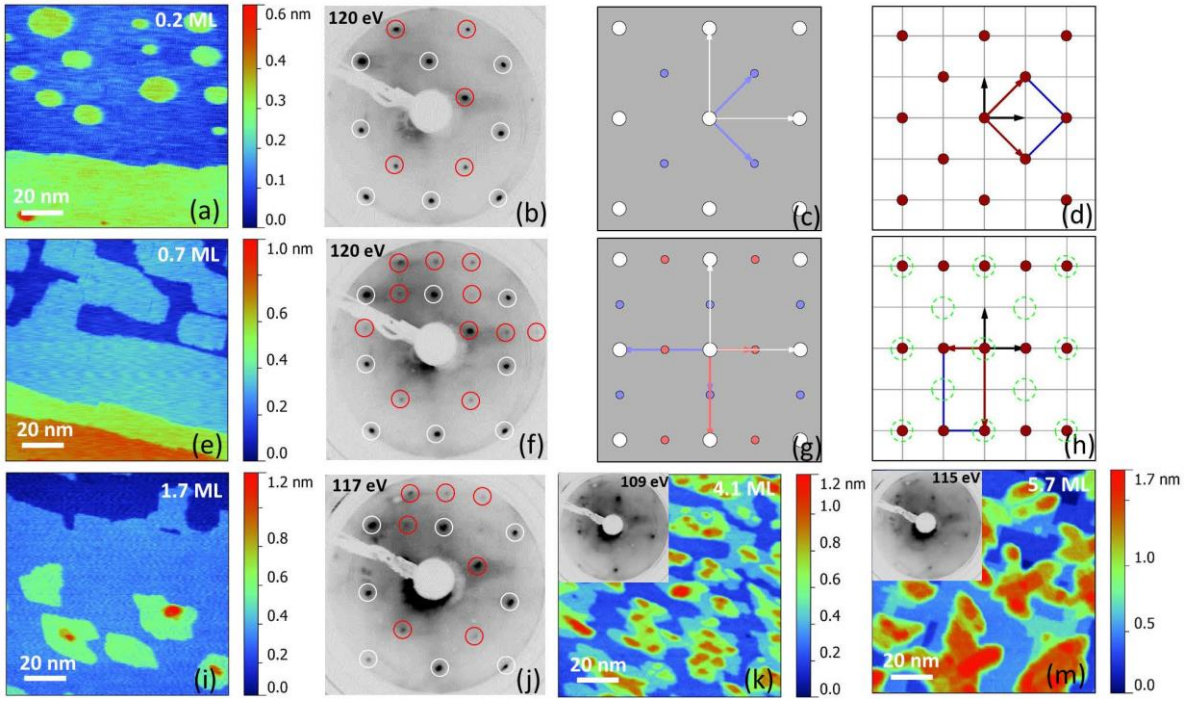

Figure 4-1 (a), (e), (i), (k), (m) Topography images of room-temperature-grown Mn on Cu(001) with coverage of 0.2 ML, 0.7 ML, 1.7 ML, 4.1 ML, and 5.7 ML, respectively. Feedback parameters: +0.2 V, 2.0 nA. Color bars on the right hand side show the surface roughness. (b), (f), (j) LEED patterns for the films shown in (a), (e), (i) at 120 eV, 120 eV, and 117 eV electron energy. White and red circles mark the substrate diffraction spots and superstructure spots, respectively. Insets of (k), (m) are the respective LEED patterns at 109 eV and 115 eV. (c), (g) Simulated LEED patterns for *c*(2×2) and *p*(1×2) [plotted together with *p*(2×1)] superstructures, respectively. White arrows show the substrate unit cell vectors, blue arrows *p*(1×2) and pink arrows *p*(2×1) superstructure unit cell vectors. (d), (h) Correspondingly simulated real-space lattices for (c) and (g). Crossing points of gray grids are atomic sites for the Cu(001) substrate surface, red dots Mn atoms in the topmost layer. Note that in (h) only one domain [*p*(2×1)] is plotted. Green circles in (h) indicate the *c*(2×2) sites. Black arrows demonstrate substrate unit cell vectors and red arrows are the superlattice unit cell vectors.

4.3 Interface modification

As discussed in the last section, at room temperature, thick Mn film can hardly grow in a layer-by-layer mode on the Cu(001) substrate, which is not favorable because lots of

magnetic phenomena are expected in structures with two-dimensional (2D) configurations in surface magnetism. The following parts will mainly discuss different methods for achieving 2D thick overlayers via interface modification.

4.3.1 Surfactant effect

Oxygen, when introduced into the growth of 3*d* transition metals like Co, Ni, and Fe on Cu surfaces, exhibits a surfactant effect which assists to reduce the possibility of three-dimensional (3D)-type structures and enhance the 2D growth mode [143–146]. During the growing process, oxygen is always floating on top of the deposited layer and does not form a bulk-like oxide with the 3*d* metal, which lowers the surface free energy of the metal film and facilitates a layer-by-layer growth scenario, as Figure 4-2 schematically illustrates.

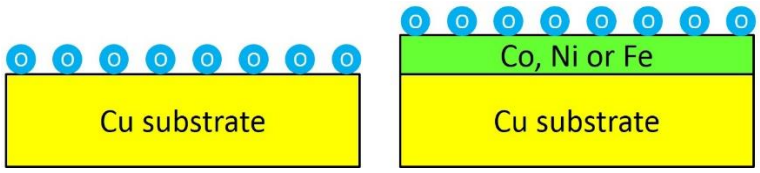

Figure 4-2 Sketch of the oxygen surfactant-assisted growth of Co, Ni, or Fe on a copper substrate. The top shows the Cu substrate with a reconstructed oxygen layer on left and the right is the deposition process of a metal film onto the oxidized Cu substrate. This sketch was drawn according to Ref. [146].

Mn also belongs to the 3*d* transition metals. Analogous to the surfactant-assisted growth of Co, Ni and Fe, oxygen could also be utilized to lower the surface free energy and give rise to a 2D-like structure for Mn deposition onto Cu(001) at room temperature. To achieve a controllable oxygen coverage, the clean Cu(001) crystal was annealed at 500 K in the oxygen atmosphere (1×10^{-6} mbar) with the dosage of 1200 Langmuir (L) [146]. Figure 4-3 (a) and (b) compare LEED patterns for clean and oxygen modified Cu(001) surfaces. Before oxidation, the substrate exhibits a well-defined surface, as the sharp *p*(1×1) pattern indicates. The oxidation procedure produces an ordered $\left(\sqrt{2}\times2\sqrt{2}\right)R45°$ oxygen reconstruction, the so-called "missing-row" (MR) reconstruction, for between two neighboring oxygen rows, one row is missing, as Figure 4-3 (d) illustrates. Since there are two orthogonal oxygen-reconstructed domains on Cu(001), the real LEED pattern will show diffraction spots for both, giving rise to the experimental observation in Figure 4-3

(b). In the simulated LEED pattern of Figure 4-3 (c), the diffraction spots from the orthogonal domains are marked by red and purple colors, respectively, such that this scenario is clearly seen. On such oxygen-reconstructed surface, the number of oxygen atoms amounts to about 37.5% of the surface layer if considering 1.5 O atoms and 4 Cu atoms in an overlayer unit cell.

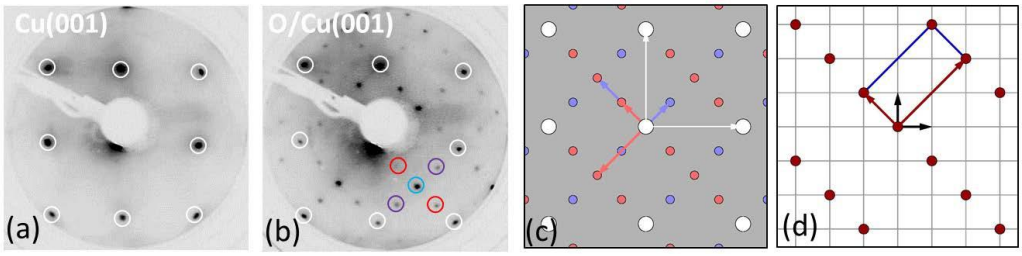

Figure 4-3 (a), (b) LEED patterns for clean Cu(001) and the "missing-row" reconstructed oxygen/Cu(001) surface at 130 eV. White circles mark the diffraction spot positions for the substrate, red and purple circles mark the diffraction spots for two orthogonal domains in a unit cell of the superstructure. (c) Simulated LEED pattern for (b), blue and pink dots demonstrate diffraction spots from two orthogonal domains and blue and pink arrows are the corresponding unit cell vectors. White arrows are unit cell vectors for the substrate. (d) Simulated real space lattice, crossing points of gray nets and red dots are the substrate and overlayer atoms, respectively. Only one superstructure domain is shown here. Black arrows demonstrate Cu(001) substrate unit cell vectors and red arrows are the oxygen overlayer unit cell vectors.

With the well-defined oxygen-reconstructed Cu(001) template, room temperature deposited Mn surfaces with different coverages are shown in Figure 4-4. The sub ML Mn growth on MR-reconstructed O/Cu(001) differs greatly from that of sub ML Mn/Cu(001) discussed in the last section. The islands do not have regular shape in Figure 4-4 (a). The surface roughness for a sub-ML of Mn [Figure 4-4 (a)] is lower than for higher coverages and the growth mode exhibits a 2D-like fashion even for deposition of thicker layers, as shown in Figure 4-4 (b), (c), and (d). Line profiles in Figure 4-4 (h) taken from topographies give a more distinct view of the surface roughness, which stays at an almost constant level of 5 Å above 1 ML. Differently from the surfactant-assisted growth of Co, Ni, and Fe on a copper substrate, the LEED pattern for the sub-ML Mn surface and even thicker overlayers [shown in Figure 4-4 (e), (f), and (g)] do not exhibit any *c*(2×2) superstructure as those in

the Co, Ni, and Fe cases. The LEED pattern gets more and more diffuse for thicker Mn films and from 4.2 ML on, no clear spots can be distinguished. Since the well-ordered *c*(2×2) phase that forms upon deposition of the ferromagnetic metals Co, Ni, and Fe on the MR-reconstructed O/Cu(001) demonstrate the surfactant effect of oxygen [145,146], the absence of the *c*(2×2) superstructure in Figure 4-4 (e) and (f) indicates that there is no oxygen surfactant effect in the Mn deposition procedure, although the oxygen does assist the initial 2D growth of Mn. Accordingly, manganese oxide may exist in the bulk of the films. The binding energy between Mn and oxygen is supposed to be larger than that between Mn and Cu, such that oxygen cannot simply segregate on top of the Mn surface without forming oxides.

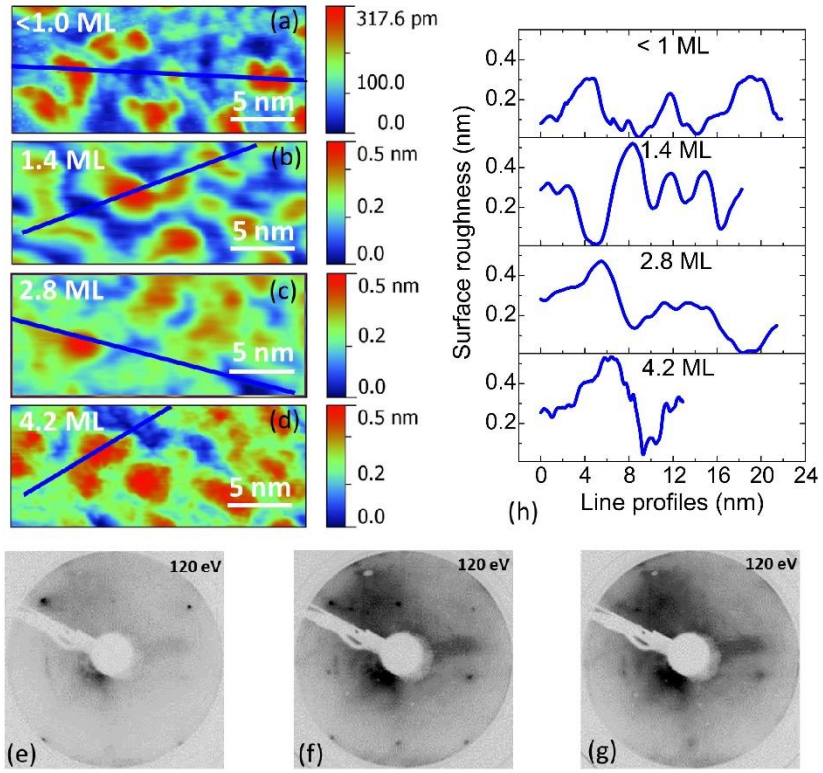

Figure 4-4 (a), (b), (c), (d) Constant-current topographies of Mn grown on the oxygen "missing-row" reconstructed Cu(001) surface. Thicknesses are <1.0 ML, 1.4 ML, 2.8 ML, 4.2 ML. Color bars on the right demonstrate the surface roughness. Feedback parameters: (a) +0.5 V, 1.18 nA; (b) +0.2 V, 2.2 nA; (c) +0.2 V, 2.3 nA; (d) +0.2 V, 1.4 nA. (e), (f), (g) LEED patterns for (a), (c), (d) at 120 eV. (g) Surface line profiles for (a), (b), (c), (d) (top-down sequence), as marked by blue lines in the topography images.

4.3.2 Seeding layer effect

As discussed in Chapter 3, Mn thin films can be structurally and magnetically stabilized by ferromagnetic Co layers. If the Co coverage is below a critical thickness, e.g. sub ML, will it assist the 2D growth and still stabilize the Mn adlayer? In this section, the role of sub-ML Co in the Mn-growth procedure will be discussed.

At room temperature, 0.6 ML and 0.4 ML Co are epitaxially grown on Cu(001) as templates are for the subsequent deposition of sub-ML and thicker Mn layers. STM topographies in Figure 4-5 (a) and (b) show pseudomorphically grown Co islands and sharp LEED patterns indicate well-defined surfaces. After 0.1 ML Mn deposition on 0.6 ML Co/Cu(001), the separately distributed Co islands of Figure 4-5 (a) are connected and larger patches are formed in Figure 4-5 (b). Meanwhile, there are 1~2 ML higher small islands formed on top of these large patches. 0.3 ML Mn almost fill up gaps between islands and 1 ML coverage completely smoothens the first layer and simultaneously starts a new layer, as Figure 4-5 (c) and (d) illustrates. Below 1 ML, the surface roughness is higher than in thicker films, which possess an almost constant roughness up to 4.2 ML. For Mn coverages higher than 1 ML, Figure 4-5 (f), (g) and (h) demonstrate layer-by-layer growth mode. LEED patterns in the sub-ML range of Mn become more and more diffuse with an enhanced background for increasing coverage. At 1.3 ML, extra *c*(2×2) superstructure spots appear in the diffraction pattern, shown in Figure 4-5 (f), and after further deposition, the background intensity is increased more and more till the diffraction spots fully disappear at 4.2 ML. The *c*(2×2) superstructure in Figure 4-5 (n) indicates the formation of an ordered surface alloy in Figure 4-5 (f), possibly by MnCu alloying in areas where copper substrate is not covered by Co. Because the exposed copper area in Figure 4-5 (e) is more than half a ML and higher than that in Figure 4-5 (a), when Mn reaches these areas and fills up the gaps, the MnCu alloy formed in (f) should be more than that in (d). According to the previous discussion on MnCu alloy in this chapter, the MnCu *c*(2×2) alloy starts at 0.3 ML Mn coverage and is maximmu at 0.5 ML [134]. Although meanwhile, Mn may alloy together with Co as well, possibly in a disordered way, the higher percentage of MnCu alloying could lead to the ordered *c*(2×2) phase in Figure 4-5 (f). From the LEED patterns in Figure 4-5, a disordered interfacial alloy is possibly present in the Co-assisted 2D growth of Mn, possibly the intermixed alloying among Mn, Co, and Cu atoms.

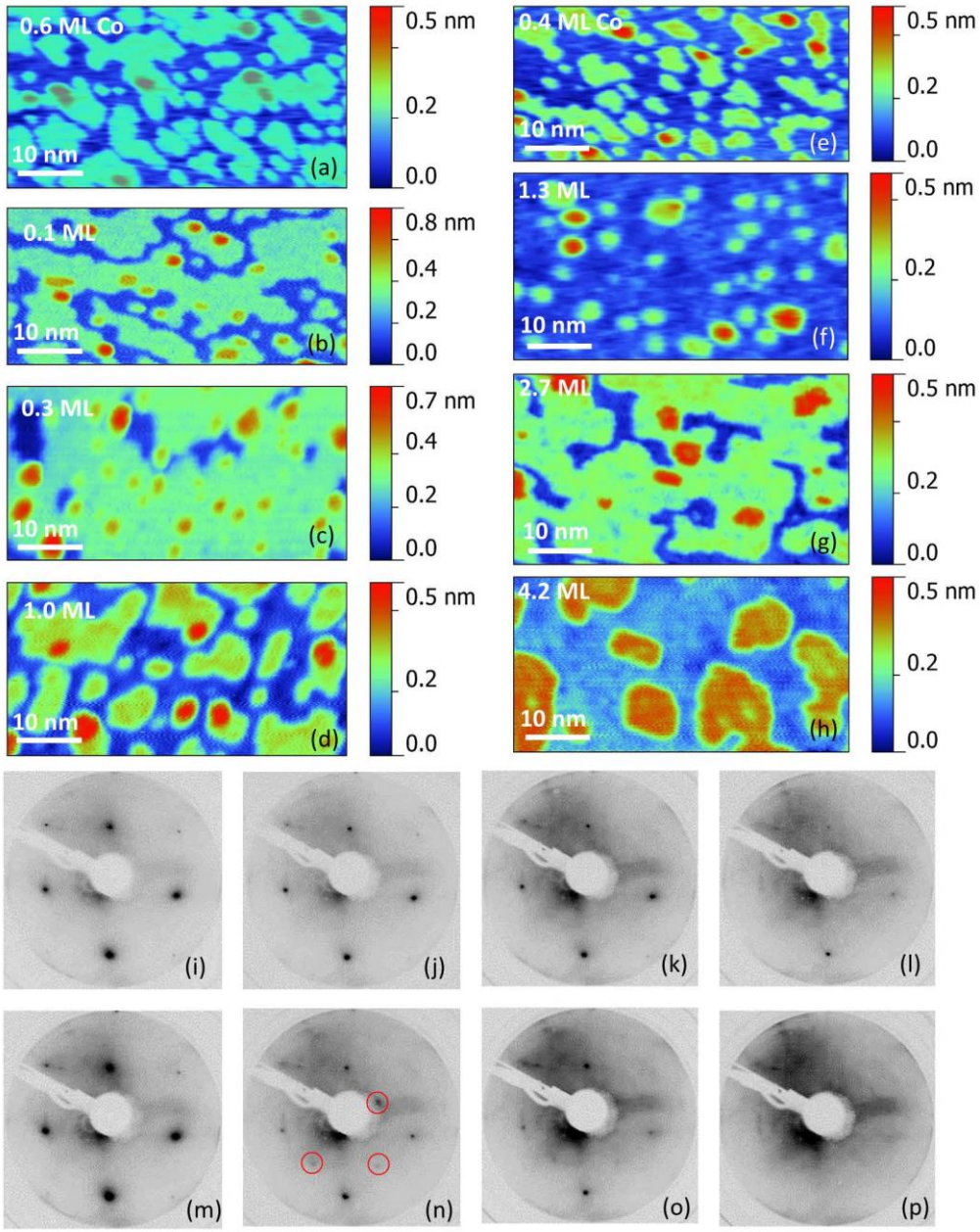

Figure 4-5 (a), (e) Topography images of 0.6 ML and 0.4 ML Co on Cu(001). (b), (c), (d) Mn grown on 0.6 ML Co/Cu(001) with thicknesses of 0.1 ML, 0.3 ML, and 1.0 ML. (f), (g), (h) Mn grown on 0.4 ML Co/Cu(001) with thicknesses of 1.3 ML, 2.7 ML, and 4.2 ML. Color bars on the right demonstrate the surface roughness. (i), (j), (k), (l) are LEED patterns at 140 eV for (a), (b), (c), (d), respectively. (m), (n), (o), (p) are LEED patterns at 140 eV for (e), (f), (g), (h), respectively. Red circles in (n) indicates superstructure spots. Feedback parameters: (a) +0.2 V, 2.2 nA; (b) +0.2 V, 2.1 nA; (c) +0.2 V, 2.1 nA; (d) +0.2 V, 2.5 nA; (e) +0.2 V, 2.5 nA; (f) +0.2 V, 2.1 nA; (g) +0.2 V, 2.1 nA; (h) +0.2 V, 2.2 nA.

From this section it can be concluded that the influence of a small amount of Co on the growth of Mn on Cu(001) is remarkable, especially for thicker Mn layers. The 2D growth of Mn layers is favored by these Co nanostructures which act as seeds for the incoming Mn atoms. Thus we can call this Co-assisted growth a "seeding layer effect". Compared to the oxygen-assisted growth of Mn in the last section, a Co seeding layer can better define the surface roughness and does not introduce surface contamination during and after the deposition.

4.4 Summary

Room-temperature-deposited Mn films with different thicknesses have been investigated. In the sub-ML thickness range, different phases of surface MnCu alloy have been observed, such as *c*(2×2) (island coverage of 0.2 ML), *p*(2×1) and *p*(1×2) (island coverage of 0.7 ML). When the Mn coverage exceeds 1 ML, the growth mode changes into the Stranski-Krastanov growth and the surface roughness increases. The ordered MnCu-surface alloy cannot structurally stabilize the subsequently overgrown Mn and a 2D structure can hardly be achieved at room temperature for thick Mn films on Cu(001).

To obtain a thick 2D- Mn film, an oxidized Cu interface and a nanostructured Co seeding layer have been intentionally established prior to the Mn deposition. The oxygen surfactant effect is not favored for the Mn deposition on the oxygen-"missing-row"-reconstructed surface, which could be caused by a larger binding energy between Mn and O than between Mn and Cu. Sub-ML nanostructured Co islands can better define the surface roughness and do not introduce surface contamination during and after deposition, such that a better-defined 2D growth of Mn films is achieved.

5 Growth of Mn on Ni(111)

5.1 Introduction

Growth of 3*d* thin films on metallic substrates is an interesting topic, because except for the diverse crystalline structures, the structure-related electronic and magnetic properties are especially attractive for researchers. In the past decades, Mn thin films have been explored intensively [55,88,90,99,101,107,118,132,133,135,147–150]. When deposited on a metal surface, Mn could form ordered or disordered alloys with the substrate atoms [99,149,151,152]. In some cases, alloys are only limited to the surface, such as Mn on Cu(100) [98], Ni(100) [99,148], and Ni(110) [149,153], while some alloys involve a few atomic layers as in Mn/Ag(001) [154]. In other cases, like Mn on Fe(100) [155] and Fe(110) [156], no alloy is formed, and only a pure Mn adlayer is found.

This chapter introduces the growth of Mn thin films on a Ni(111) substrate, a system not yet explored so far. Firstly, STM and LEED studies on room-temperature-deposited Mn of different thicknesses will be shown. Then the influence of temperature on the crystalline structure of the Mn film will be discussed together with a simulation of the LEED pattern obtained from low-temperature-prepared Mn film. The last section is about the comparison of the growth of thick Mn films on Ni(111) and Cu(001) at low temperature.

5.2 Growth of Mn on Ni(111) at room temperature

Room-temperature-prepared Mn films will be presented in this section. The growth of Mn at different stages is studied by STM and MEED. Atomically resolved surface topography images with sub-ML Mn islands on Ni(111) are also discussed for further understanding of the initial-stage growth of Mn.

5.2.1 Room-temperature deposition of Mn

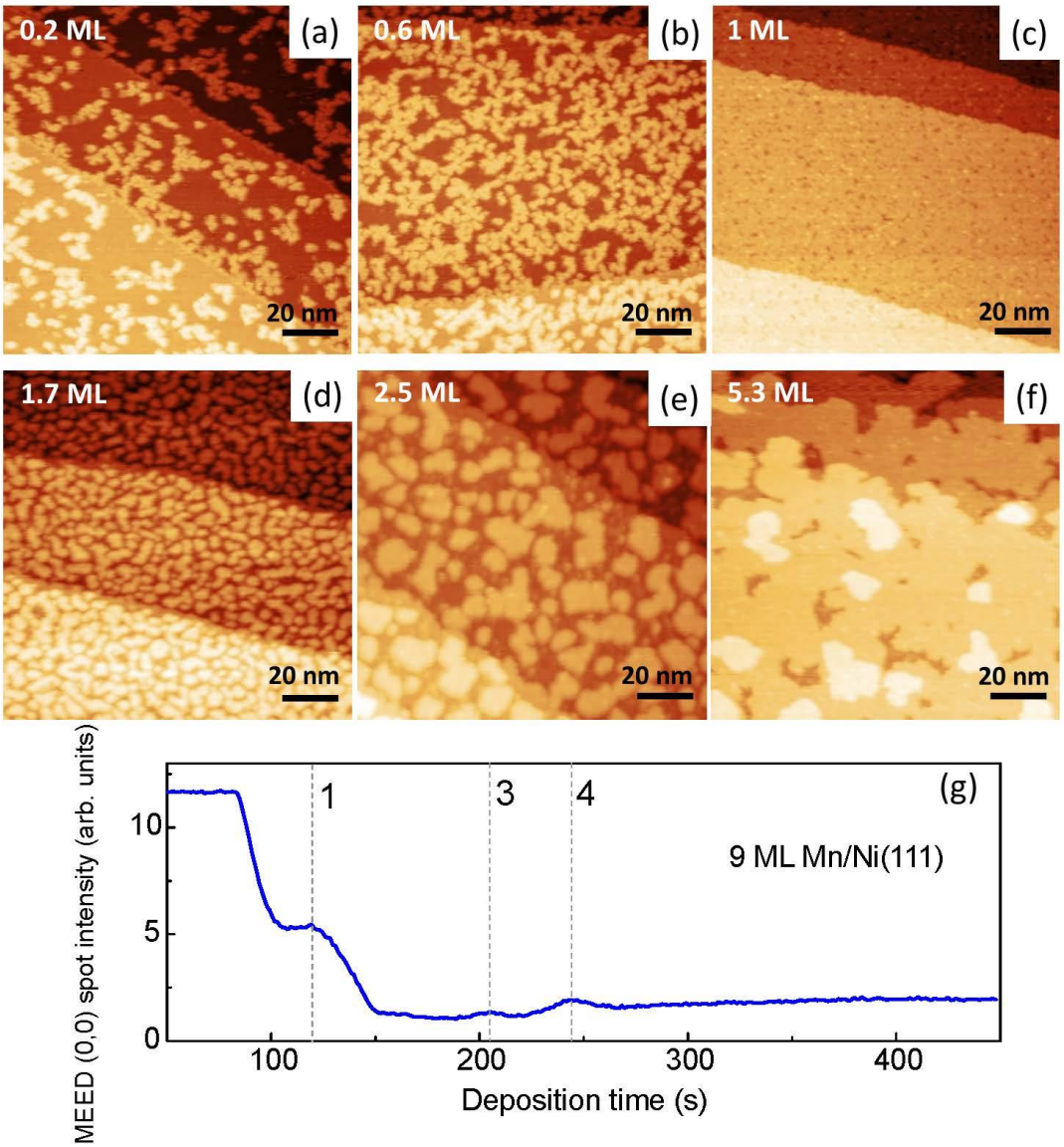

Figure 5-1 (a), (b), (c), (d), (e), (f) Constant-current topographies of room-temperature-deposited Mn on Ni(111) with thicknesses of 0.2 ML, 0.6 ML, 1 ML, 1.7 ML, 2.5 ML, 5.3 ML. (g) MEED curve of the (0,0) spot intensity during the deposition of 9 ML Mn on Ni(111). Feedback parameters: (a) +0.2 V, 1.9 nA; (b) +0.2 V, 2.2 nA; (c) +0.5 V, 1.1 nA; (d) +0.2 V, 2.1 nA; (e) +0.5 V, 1.4 nA; (f) -0.2 V, 2.1 nA.

Room-temperature-deposited Mn on Ni(111) demonstrates a structural thickness-dependent behavior. In the sub-ML range, Mn atoms first form tiny scattered islands and the gaps in between are gradually filled to form a wetting layer, as seen in Figure 5-1 (a)–(c) . At the thickness of 1.7 ML, islands in Figure 5-1(d) become lager and gaps are

more uniformly distributed than those in the sub-ML range. Between 3 ML and 4 ML, even larger patches are formed at 2.5 ML thickness in Figure 5-1(e) and patches of similar size can be seen in Figure 5-1(f). To gain a more systematic understanding of the growth behavior of Mn on Ni(111), a thick Mn layer was deposited and an in-situ MEED intensity curve simultaneously recorded, as shown in Figure 5-1(g). According to the MEED curve, after about 4.5 ML, no oscillation occurred during the following deposition, which means that the layer-by-layer growth probably ends at this or a slightly higher thickness. In the MEED curve, the second peak cannot be seen. The reason could be that the electron reflex spot intensity on the fluorescent screen becomes too dim when the second layer starts to grow and the sensitivity of the detecting CCD camera is not high enough for such low intensity signal, indicating some phase transition after the completion of the first layer. Figure 5-1(f) illustrates that the layer-by-layer growth still exists at 5.3 ML, although the peak for the fifth ML is not present in the MEED curve, which could be a hint for another phase transition after 4.5 ML.

5.2.2 Atomic-resolution imaging of a submonolayer of Mn on Ni(111)

As discussed in the last section, above 1 ML of Mn, a phase transition could happen and this phenomenon is further confirmed by LEED. The LEED images do not exhibit any diffraction pattern above 1 ML Mn thickness at room temperature, which means that the order of the hexagonal crystallographic lattice is no longer conserved in the surface layer. To obtain a deeper understanding of the sub-ML Mn lattice structure, Figure 5-2 (a) and (b) present atomic-resolution imaging of the as grown Mn/Ni(111) surface. The two images were taken from the same sample but different areas. The time interval between the two images is short to ensure similar piezo condition of the STM scanner. The 2D fast Fourier transforms (FFT) of the Ni and Mn areas reveal that the lattice of sub-ML Mn islands does not conserve the substrate lateral lattice constant, as the insets of Figure 5-2 (a) and (b) show. Moreover, the Mn lattice is not a regular hexagonal one, but laterally distorted. The incommensurate Mn lattice could be due to the large lattice mismatch to the fcc Ni(111) surface. From the LEED image of a sub-ML Mn in Figure 5-2 (d), except for the sharp diffraction spots, it can only be observed a diffuse background, compared to the clean nickel surface. Considering the STM data, the background intensity could come from a distortion of the Mn crystallographic structure within the islands on Ni(111) and the distortion may

vary on islands of different size. The LEED pattern for 1 ML Mn exhibits a less diffuse background, indicating a smaller lattice distortion. Disordered interfacial alloying could also lead to LEED background intensity, however, no further evidence for this is found here. When the Mn thickness exceeds 1 ML, no LEED pattern for room-temperature-deposited Mn/Ni(111) is observed. The reason should be consistent to the discussion before in connection with Figure 5-1, namely that a phase transition occurs above 1 ML Mn thickness and that the crystallographic structure for each layer differs from the one underneath.

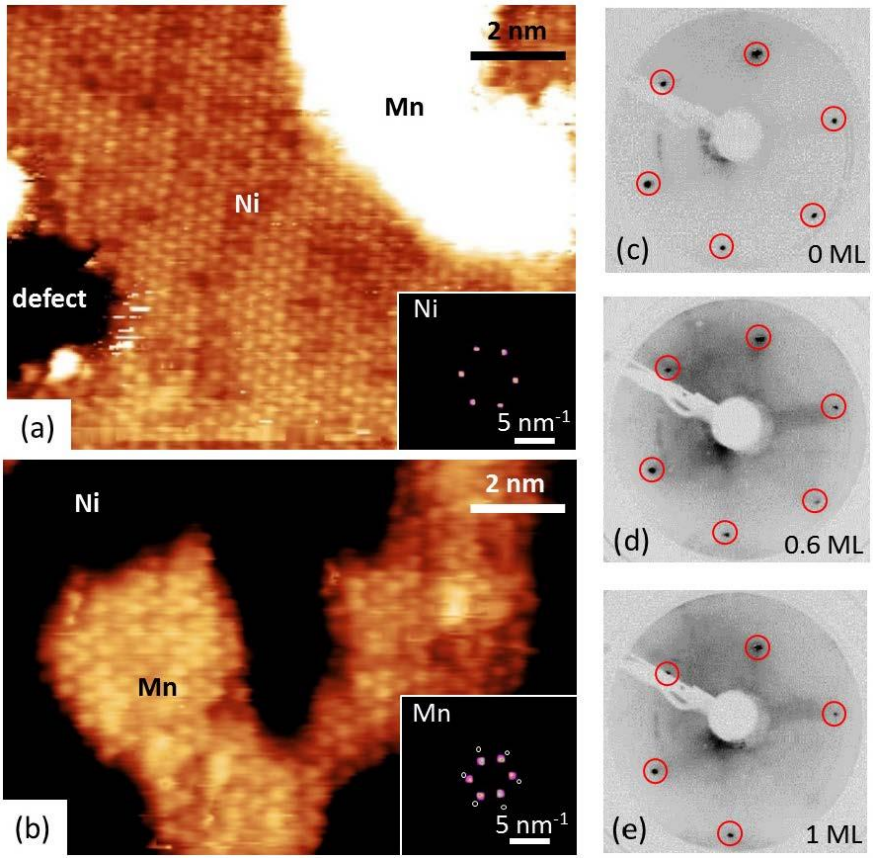

Figure 5-2 (a), (b) Atomic-resolution constant-current STM images for 0.2 ML Mn/Ni(111) showing the Ni substrate (a) (+25 mV, 2.2 nA) and a Mn island (b) (+49 mV, 2.8 nA) with enhanced contrast. Insets show the 2D FFT of the corresponding STM images for Ni(111) and Mn/Ni(111). The white circles in the inset of (b) represent the superimposed 2D FFT pattern of the inset of (a). (c), (d), (e) LEED patterns for Ni(111), room-temperature-deposited 0.6 ML Mn/Ni(111) and 1 ML Mn/Ni(111). Red circles mark the hexagonal *p*(1×1) diffraction spots at 120 eV.

5.3 The influence of temperature on the growth of a monolayer Mn on Ni(111)

Temperature plays an important role for thin film deposition [157–160]. As was known before, 1 ML is a critical thickness for room-temperature-deposited Mn/Ni(111). The change of the crystallographic structure of Mn with 1 ML thickness at different temperatures is an interesting topic to be discussed.

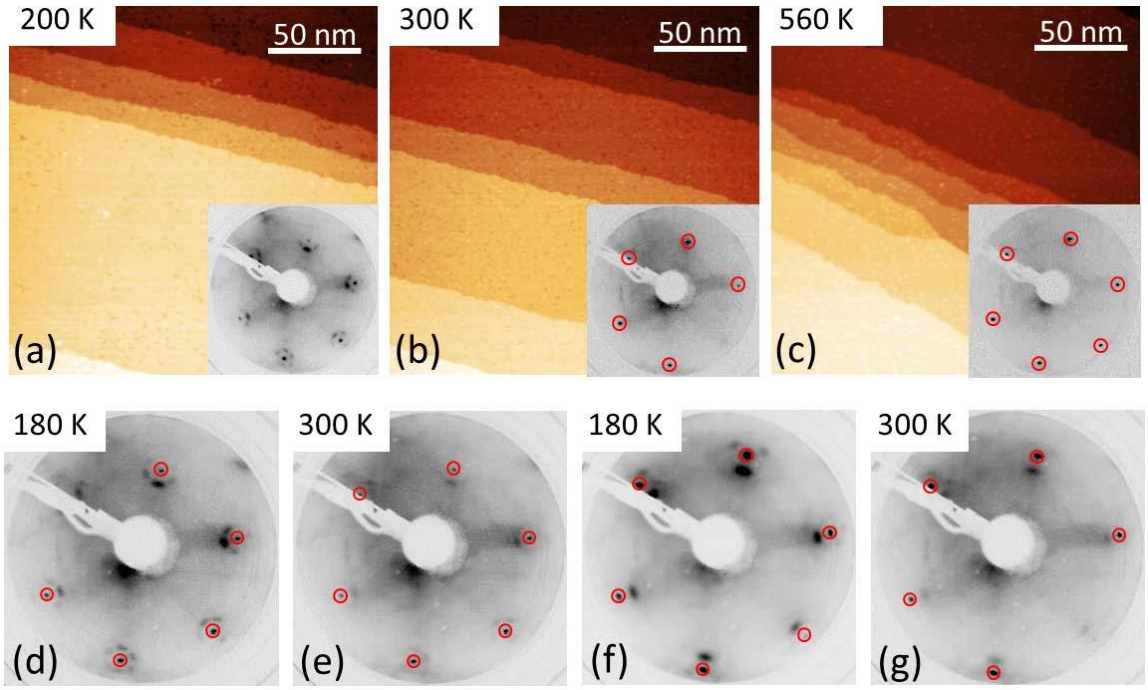

Figure 5-3 (a), (b), (c) Room temperature constant-current STM images of 1 ML Mn/Ni(111) prepared at 200 K, 300 K, 560 K, respectively. The inset of (a) shows the LEED pattern taken at 180 K, 150 eV. Insets of (b) and (c) are corresponding LEED patterns both taken at room temperature, 120 eV. (d), (e) show LEED patterns for sample in (a) at 145 eV, taken at 180 K and 300 K, respectively. (f), (g) are LEED patterns at 113 eV after sample in (a) was annealed from 180 K (f) to 300 K (g). Red circles in the LEED patterns mark the hexagonal *p*(1×1) diffraction spots. Feedback parameters: +1.1 V, 0.49 nA.

Figure 5-3 shows the result of the characterization by room-temperature STM and LEED of 1 ML Mn on Ni(111), deposited at different temperatures. STM topography images for deposition at 200 K, 300 K and 560 K show complete smooth Mn wetting layers on the

nickel substrate. LEED is an effective tool for exploring the crystallographic structure in reciprocal space. LEED patterns corresponding to Mn deposited at different temperatures exhibit diverse features. For growth at 200 K, the LEED pattern displays diffuse superstructure spots around the substrate diffraction spots. Only hexagonally ordered spots from the substrate are present at both, 300 K and 560 K growth temperature. What makes the 560 K LEED pattern different from the room-temperature one are the sharp diffraction spots on a much lower background, indicating a well-ordered (1×1) hexagonal lattice for high-temperature-deposited Mn. After annealing the 200-K-prepared Mn layer from to 300 K, the superstructure in the LEED image is almost gone and only the inner dim spots are seen, as shown in Figure 5-3 (e) and (g) at 145 eV and 113 eV, respectively. Note that the LEED superstructure observed on the 200-K-prepared Mn/Ni(111) exhibits six-fold and three-fold symmetries around the substrate lattice diffraction spots at 145 eV and 113 eV, respectively. Similar six-fold superstructures on the (111) surface have also be observed in other systems, such as Ag/Ni(111) [157–160], and Ag/Cu(111) [161].

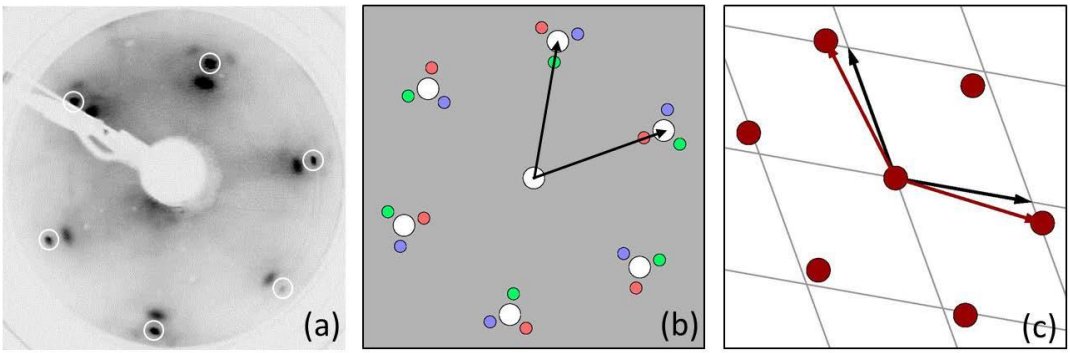

Figure 5-4 (a) LEED pattern from Figure 5-4 (f). (b) Simulated LEED pattern of (a). Three different domains are marked by pink, green, and blue colors. White spots show the hexagonal *p*(1×1) diffraction spots, black arrows represent vectors of the reciprocal unit cell. (c) Simulated real-space lattice for (b). Only one domain, corresponding to the blue spots in (b), is shown. The gray grid represents the Ni(111) substrate lattice, red dots indicate Mn atoms. Black arrows show the substrate unit cell vectors, red and arrows the superlattice unit cell vectors.

To understand the LEED superstructure observed on low-temperature-grown Mn/Ni(111), a simulation of an incommensurate lattice is performed using the LEEDpat [162] software. According to the experimental LEED image shown in Figure 5-4 (a), to achieve a consistent

pattern in the simulation, the ratio for the real-space superlattice vector to the basic lattice vector is set to be 1.113 and the two superlattice vectors are rotated 7° counterclockwise and clockwise, respectively, as the red arrows illustrate in Figure 5-4 (c). Differently from STM, LEED can reflect the lattice structure in a much larger area. The observed LEED pattern can be a superimposition of differently oriented domains. In the simulated pattern of Figure 5-4 (b), three individually oriented domains with a mutual angle of 120° are marked by separate colors. In real space [Figure 5-4 (c)], only one domain of the Mn superlattice is drawn and this domain corresponds to the blue diffraction spots in Figure 5-4 (b). The simulation of the real-space Mn lattice demonstrates that the lattice is laterally distorted in one certain direction on the hexagonal substrate lattice. The inset of Figure 5-2 (b) for the room-temperature-deposited sub-ML Mn/Ni(111) also indicates a distortion of the Mn lattice, but not just in one certain direction. The superimposition of the 2D FFT patterns for Ni(111) and 0.2 ML Mn islands in the inset of Figure 5-2 (b) indicates a larger interatomic distance in Mn islands than in the substrate.

Although the 200-K-grown Mn layer exhibits a superstructure in the LEED pattern, the room-temperature-grown layer for both 0.6 ML and 1 ML Mn thickness does not exhibit any superstructure, as Figure 5-2 (d) and (e) show. The reason could be a temperature-dependent metastable arrangement of the Mn adlayer as well as the interaction strength between Mn−Mn and Mn−Ni atoms, as illustrated in alkali-adlayer/metal systems [163]. Comparing to the LEED pattern of 560-K-deposited Mn [inset of Figure 5-3 (c)], the 300 K LEED pattern [inset of Figure 5-3 (b)] has a stronger diffuse background, indicating some disorder at room temperature, either from a weak lattice distortion, or a disordered alloy, or a coexistence of both. No superstructure in the LEED pattern of the 560-K-grown layer is seen, which could be because at such high temperature, the lattice distortion is too weak to be observed, or even absent. It should be noted that, a similar six-fold superstructure as observed in the inset of Figure 5-3 (a) for 200-K-deposited Mn has also be reported in other systems, such as Ag/Ni(111) [157–160] and Ag/Cu(111) [161]. The scenario for superstructure formation in these systems is attributed to a rotated Ag lattice with respect to the substrate and such superstructure is from high-temperature-deposited Ag layer (> 300 K). However, no three-fold superstructure as in Figure 5-4 (a) has been reported. According to the LEED pattern simulation for 200-K-deposited Mn [Figure 5-4 (b)], the superposition of differently oriented domains with distorted lattice could result in

the three-fold superstructure which is consistent with the experimental result and may not be necessarily from the lattice rotation. Moreover, in the 200-K-deposited Mn/Ni(111) system, the *in situ* observed LEED pattern demonstrates an energy-dependent symmetry of the superstructure which changes from six-fold [Figure 5-3 (d)] to three-fold [Figure 5-3 (f)].

5.4 Low-temperature growth of a thick Mn film on Ni(111) and Cu(001)

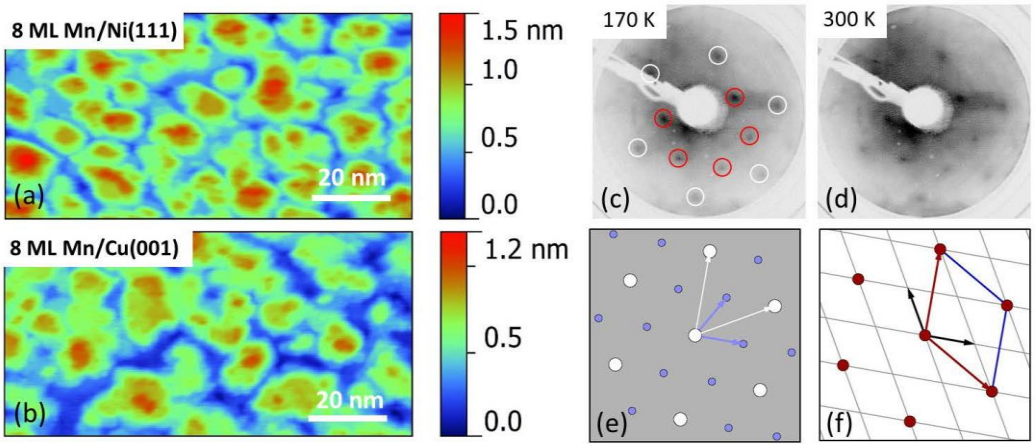

Figure 5-5 (a), (b) Room-temperature STM topographies for 170-K-deposited 8 ML Mn on Ni(111) and Cu(001), respectively. Feedback parameters: (a) +0.2 V, 2.16 nA; (b) +0.5 V, 1.13 nA. (c) LEED pattern for (a) taken at 170 K. (d) LEED pattern for (a) taken after annealing to room temperature. Electron energy for both patterns is 120 eV. White circles show the positions of hexagonal *p*(1×1) spots and red circles mark the diffraction spots of the superstructure. (e) Simulated LEED pattern of (c). White and blue arrows represent reciprocal unit cell vectors for substrate and overlayer, respectively. (f) Simulated real-space lattice for (e). The red dots and crossing points of the gray grid are for topmost and top second Mn atoms, respectively. Black arrows show the grid-layer unit cell vectors, red arrows the dot-layer superlattice unit cell vectors.

As discussed before, a low-temperature-deposited ML Mn exhibits a metastable laterally distorted lattice at 200 K. How does the crystallographic structure arrange in thick Mn films at low temperature? Figure 5-5 (a) and (b) show STM topography images of 8 ML Mn deposited at 170 K on Ni(111) and Cu(001), respectively. Both exhibit a Stranski-

Krastanov (SK) growth mode, i. e., layer-plus-island growth. The surface roughness for Mn on Ni(111) is slightly higher than that on Cu(001). The obvious difference between low temperature deposited Mn on the two substrates is the ordered phase of Mn on Ni(111). No LEED spot but a diffuse background can be seen on 8 ML Mn/Cu(001) at 170 K, indicating a structural disorder in the thick Mn film. On the contrary, the same thickness of Mn on Ni(111) exhibits not only diffuse (1×1) hexagonal diffraction spots, but also some superstructure spots, as seen in Figure 5-5 (c). By analyzing this superstructure, the simulated LEED pattern in Figure 5-5 (e) reveals a $\left(\sqrt{3}\times\sqrt{3}\right)R30°$ reconstruction. The reconstruction remains unchanged after annealing the film to 300 K, except for a stronger diffuse background, indicating a stable lattice structure in the thick Mn film. The simulated real-space lattice does not show incommensurate lattice distortion in the overlayer, and the phase for a thick Mn layer differs from that of thin layers discussed before.

5.5 Summary

Mn deposition at room temperature on Ni(111) exhibits a layer-by-layer growth up to 5.3 ML. Two phase transitions might occur after the completion of the first ML and at 4.5 ML. In the layer-by-layer-growth thickness range, the size of Mn islands depends on thickness. Atomic-resolution imaging of sub-ML Mn/Ni(111) reveals a laterally distorted Mn lattice, while the LEED study suggests a relatively smaller distortion in the Mn wetting layer than in 0.2 ML Mn islands. Disordered interfacial alloying could also exist, leading to the diffuse LEED background, but no further evidence is found.

The low-temperature-deposited 1 ML Mn film shows a metastable lattice distortion. This metastable phase becomes less distorted when the temperature is increased to 300 K. The reason could be a temperature-dependent metastable arrangement of the Mn adlayer as well as the interaction strength between Mn−Mn and Mn−Ni atoms. The 300-K LEED pattern of 1 ML Mn/Ni(111) with a stronger diffuse background indicates some disorder at room temperature, either from a weak lattice distortion, or a disordered alloy, or a coexistence of both. The (1×1) LEED pattern of the 560-K-grown-ML Mn indicates weak or no lateral lattice distortion.

Thick Mn films on both Ni(111) and Cu(001) exhibit SK growth at low temperature. Mn/Ni(111) shows a $\left(\sqrt{3}\times\sqrt{3}\right)R30°$ reconstruction while Mn/Cu(001) does not exhibit

any regular crystalline lattice according to the absence of diffraction spots. The $(\sqrt{3}\times\sqrt{3})R30°$ reconstruction for thick Mn/Ni(111) exhibits no obvious temperature dependence up to 300 K and a stable lattice structure should be present. The simulated real-space lattice shows no incommensurate lattice distortion in the overlayer, and the stable phase for thick Mn/Ni(111) differs from the metastable lattice of the wetting layer on Ni(111).

6 Characterization of graphene on Ni(111) and of a submonolayer Mn on graphene

6.1 Introduction

Nickel, due to its catalytic property in CVD procedures, has been applied as substrate for the growth of graphene (Gr) in recent years. Because of the almost perfect match of the Ni(111) and graphite lattice parameters, Gr/Ni(111) is attracting more and more attention [164]. There have been many studies of Gr on Ni(111) [39,41,45,165–174]. Although compared to other substrates [175–180] the Ni(111) matches Gr best, the preparation conditions, such as temperature [181,182], carbon concentration at the growth front [182,183], purity of the substrate [182], or cooling rate [171,184], can influence the quality of the Gr sheets on the nickel substrate, such that the structure formed on the sample surface could be far more complicated than expected [182]. Except for the (1×1)-restricted Gr, rotations, extra carbon structures underneath, or surface defects may also exist and influence the Gr interaction with the substrate. These unexpected structures exhibit unique structural and electronic properties which may be interesting for Gr-based electronic and spintronic applications.

In this chapter, the growth of Gr on Ni(111) will be discussed with respect to different preparation conditions in sections 6.2 and 6.3. The preparation conditions are summarized as follows:

(1) 800−840 K, 600−1800 L propylene, 4−10 min subsequent annealing at dosing temperature;
(2) 900 K, propylene at 1×10^{-5} mbar for 5 min (3000 L), 20 min subsequent annealing at 920 K;

(3) 900 K, propylene at 2.5×10^{-6} mbar for 10−20 min (1500−3000 L), no subsequent annealing.

Gr prepared under condition (1) exhibits mainly (1×1) epitaxial phase, as discussed in section 6.3.1, while under condition (2) and (3), the percentage of rotated Gr is increased, leading to diverse surface configurations, as discussed in section 6.3.2. Section 6.4 selects areas of rotated Gr prepared under condition (2) and discusses their structural and electronic properties. Section 6.5 is about the influence of oxygen on the rotated Gr prepared under condition (3) on Ni_2C/Ni(111). In section 6.6, sub-ML Mn in contact with Gr is shown.

6.2 Prior to graphene

It is already known that the Gr growth on Ni(111) depends not only on the temperature [181,182], but also on the carbon concentration in the substrate [182,185]. When the temperature is not sufficiently high, carbide may saturate the surface and prevent further formation of Gr[186]. Values for this temperature limit for the surface carbide phase have been reported before, such as 420 °C [182], 460 °C [170], 480 °C [186] and 500 °C [181]. In Figure 6-1 (a), the LEED pattern of the clean Ni(111) substrate is shown. It demonstrates sharp (1×1) diffraction spots, indicating a well-defined surface. The detailed description of the substrate preparation procedure has been presented in the previous section 0.2.1. At 800 K, after 200 L ethylene exposure, nickel carbide is formed, as the extra superstructure spots and diffuse background in Figure 6-1 (b) illustrate. Nonetheless, if the hydrocarbon gas dosing time is long enough under these conditions, the surface carbide can also be converted into (1×1) epitaxial Gr [182]. If the temperature is high such that the surface carbide is no longer stabilized, arriving hydrocarbon molecules will decompose at the surface, and the carbon atoms will firstly dissolve into the bulk, leaving the nickel surface clean [170]. In other words, the nucleation of Gr on the surface has some time delay. According to Ref. [170], carbon atoms in the bulk nickel substrate differ from those in Gr. Because of a lower chemical potential for the latter, once Gr starts to nucleate on the surface, a carbon sink is generated and the carbon diffusion is reversed, such that bulk carbon atoms will segregate to the surface to form Gr. This time delay indicates kinetic barriers for Gr nucleation and growth. If the time is not long enough for dissolved carbon atoms to segregate, no Gr can be obtained [181]. Although Figure 6-1 (c) shows a sharp (1×1) pattern after 250 L ethylene exposure at 900 K, this pattern does not prove Gr, because the clean

Ni(111) surface after carbon dissolution would give rise to the same pattern. To further confirm that the sharp pattern in Figure 6-1 (c) is not mainly from Gr, oxygen is employed as a sensor because the Gr-covered Ni surface will be protected from oxidation [165]. After 300 L oxygen exposure, the pattern shown in Figure 6-1 (c) vanished and no diffraction spots could be seen. The carbon peak at 272 eV in the AES spectrum shown in Figure 6-1 (d) appears to be quite small, on the contrary, the oxygen peak at 503 eV is of almost the same amplitude as the nickel peak at 848 eV, indicating a large faction of Gr-uncovered oxidized nickel surface in Figure 6-1 (c). However, the possibility that some small fraction of nucleated Gr islands exist cannot be excluded.

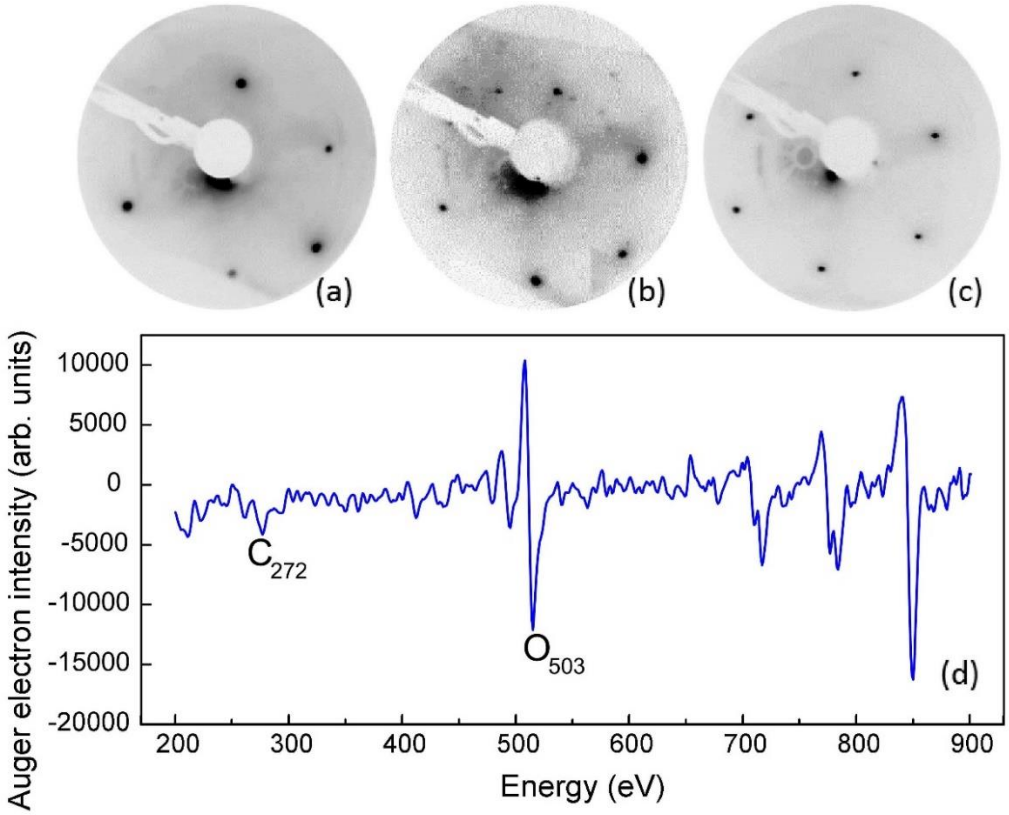

Figure 6-1 (a) LEED pattern for pristine Ni(111) at 140 eV. (b), (c) LEED patterns taken after 200 L and 250 L ethylene dosage during which the Ni(111) substrate was held at 800 K and 900 K, respectively. Both patterns have been taken at 146 eV. (d) Auger electron $dN(E)/dE$ intensity taken after the sample shown in (c) has been exposed to 300 L oxygen. All LEED patterns were taken at room temperature.

6.3 Temperature and dosing rate influence on the growth of graphene

In this section, the growth of Gr will be discussed with respect to temperature as well as hydrocarbon gas dosing rate. Bulk carbon segregation also plays an important role in modifying the contact environment of Gr.

6.3.1 Graphene preparation between 800 K and 840 K

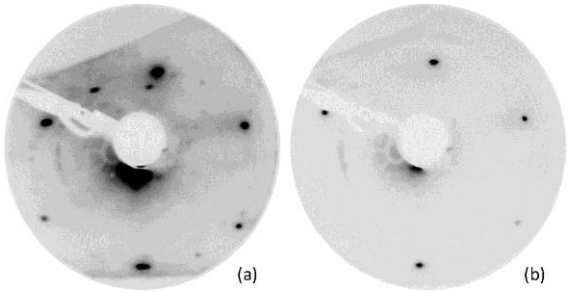

Figure 6-2 (a) A LEED pattern after dosing 600 L propylene at Ni(111) substrate temperature of 800 K. It is a typical pattern for samples prepared between 800–840 K with dosage of 600–1800 L. (b) LEED pattern taken after the sample shown in (a) was annealed without propylene at the dosing temperature for 7 min. It is a typical pattern for samples annealed at the dosing temperature without propylene for 4–10 min. Both patterns were taken at room temperature and 110 eV electron energy.

At low temperatures, i.e., below 850 K, the growth of Gr on Ni(111) could be blocked by the surface carbide which forms prior to Gr. Tests have been done by varying the Ni(111) substrate temperature in the range of 800–840 K with different propylene dosages (600–1800 L). If there is no subsequent annealing after the dosing and the sample is just let to cool down to room temperature naturally (down to 500 K in 5 min), nickel carbide superstructure spots will be present in the LEED patterns. A representative LEED pattern is shown in Figure 6-2 (a). However, by annealing the carbide-covered surface at the same hydrocarbon-gas-dosing temperature for a few minutes in UHV, the carbide superstructure disappears and a sharp (1×1) pattern can be seen in Figure 6-2 (b). The *in situ* room-temperature STM measurements with the atomic-resolution imaging further confirm the existence of a ML of epitaxial Gr on Ni(111), as will be discussed below.

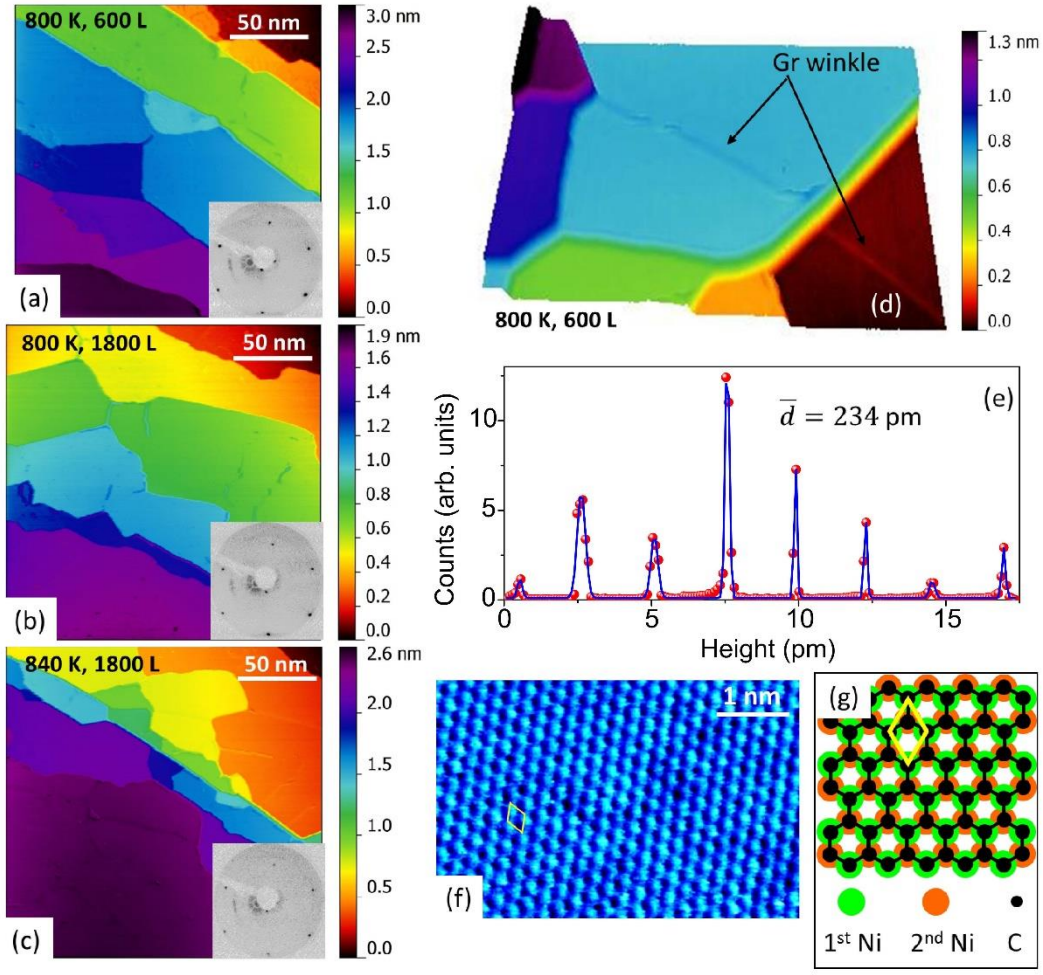

Figure 6-3 (a), (b), (c) Constant-current STM images for a ML of epitaxial Gr on Ni(111). The preparation conditions are illustrated in the top-left corner of each image. The subsequent annealing is performed at the dosing temperature without propylene for (a) 7 min, (b) 4 min, (c) 10 min, respectively. The inset of each image shows the corresponding LEED pattern at 92 eV. (d) 3D plot of the topography for ML epitaxial Gr on Ni(111) with the same preparation condition as (a). (e) Histogram of STM image shown in (d). (f) atomic-resolution STM image for a ML of epitaxial Gr/Ni(111). This area is from the same sample as shown in (b). The yellow diamond illustrates one Moiré pattern unit cell. (g) Sketch of a top view of a top-hcp Gr sheet on Ni(111) as shown in (f). The yellow diamond demonstrates the atomic configuration inside one contrast unit cell with a periodicity of 0.245 nm. Solid green and orange circles represent nickel atoms in the first and second nickel layers from the top. Solid black circles illustrate carbon atoms in the Gr sheet. Feedback parameters: (a) +1.3 V, 0.65 nA; (b) +0.65 V, 1.17 nA; (c) +1.14 V, 0.49 nA; (d) +1.1 V, 0.76 nA; (f) +0.59 V, 2.19 nA.

STM topography images in Figure 6-3 show the epitaxial single-layer Gr sheet on Ni(111). The low-temperature-prepared Gr, as Figure 6-3 (a)-(d) illustrate, has fully covered the nickel steps and typical features for Gr, wrinkles, which are due to thermal quenching [187,188], are also present on some terraces. The uniform height distribution in the histogram of Figure 6-3 (d) in Figure 6-3 (e) further confirms that the Gr layer has completely saturated the nickel surface and the average height difference between subsequent steps approximates the value of interlayer distance of close-packed-fcc Ni(111) substrate. The atomic-resolution STM image for the epitaxial Gr/Ni(111) shown in Figure 6-3 (f) reveals a 2D-Gr-crystal lattice with a three-fold symmetry due to a strong variation of the LDOS between the sublattice introduced by the substrate [189]. The bright spots correspond to the carbon atoms sitting on top of the second ML Ni to form a triangular lattice, while those carbon atoms at the first ML Ni sites appear less bright [166]. A sketch in Figure 6-3 (g) illustrates how the actual lattice arranges for the observed STM contrast in Figure 6-3 (f). This top-hcp Gr lattice is consistent to the STM image of the Gr lattice reported in Ref. [166]. Furthermore, on the atomic scale, the single Gr sheet on Ni(111) could demonstrate other arrangements with respect to the substrate lattice and different arrangements might coexist [166,45,190].

These low-temperature-prepared epitaxial Gr sheets are mainly formed by direct surface carbide conversion and the subsequent annealing procedure plays an important role in the high quality (1×1) Gr formation process. According to Ref. [182], once this (1×1) Gr is formed, the 2D-carbon sheet terminates the nickel surface and no further carbon structure can be formed underneath. This epitaxial Gr sheet is chemisorbed on Ni(111) and the strong hybridization of Ni-3*d* states and Gr out-of-plane π orbitals cause a band gap opening of the Dirac cone at the *K* point, which drastically modifies the electronic and magnetic properties of the Gr layer compared to the free-standing Gr sheet [31,37,41,173,174,191–194].

Except for the predominantly observed epitaxial ML Gr on Ni(111), when changing the scanning position on the sample, occasionally, some areas have been found exhibiting large hexagonal-shaped superlattices, as shown in Figure 6-4 (a). In the topography, the line profile AB exhibits a periodicity of the superlattice of 3.157 nm. There are also some small patches exhibiting shorter periodicities. Detailed discussion about the mutiperiodic superlattice will be presented in section 0.4.1.

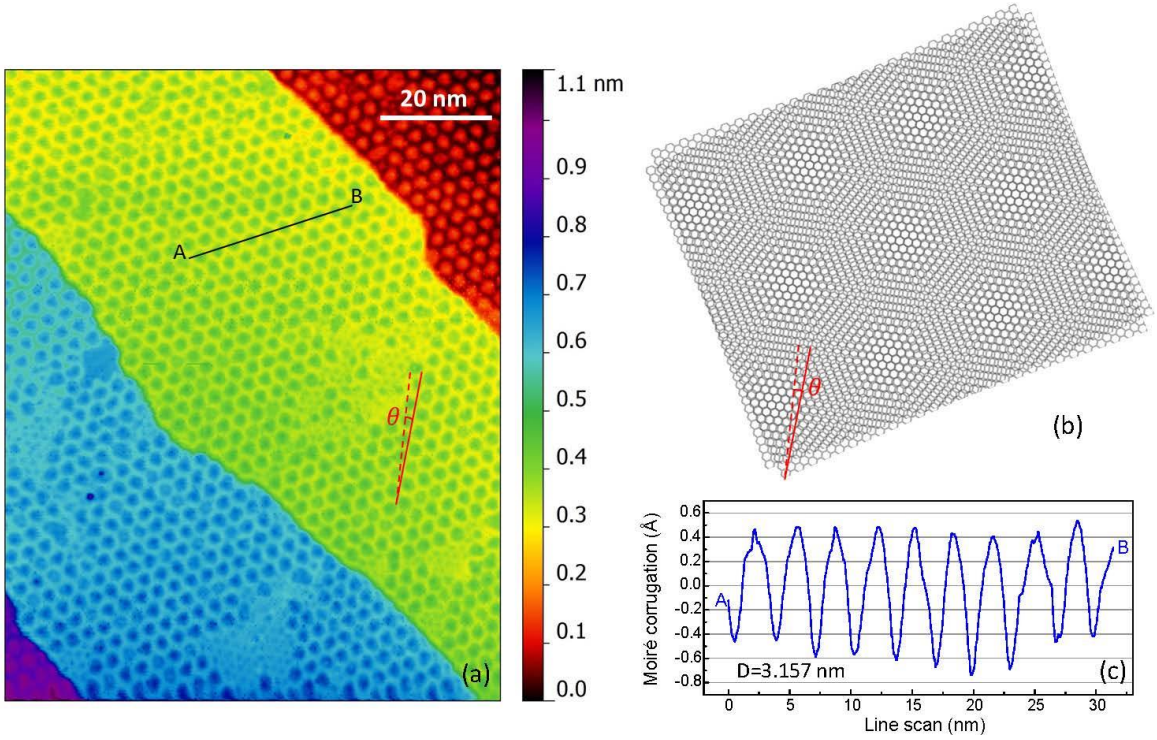

Figure 6-4 (a) Constant-current STM image of a ML Gr/Ni(111). This area is from a different scanning position on the same sample prepared also for Figure 6-3 (a). Feedback parameters: +1.07 V, 0.76 nA. (b) Simulated Moiré pattern for (a). (c) Moiré corrugation for the line scan AB shown in (a). The dashed red line indicates the [110] direction of Ni(111) and the solid red line shows the rotating angle θ for the Gr sheet with respect to the [110] direction of the substrate.

The origin of the observed superlattices have been discussed by several researchers [195–200] and the most widely accepted explanation is the Moiré assumption [201,202]. The Moiré pattern [203,204] originates from the misalignment of two periodic layers. When there is a relative rotation between two layers, the rotation-caused interference will generate a superperiodic structure with the same symmetry as the original two layers. This phenomenon is well-known in optics. Since the nickel crystalline lattice and the Gr 2D lattice both have a periodic structure, i.e., the electronic distributions of both also have the same periodic property, when the two periodic electronic lattices are coupled together and rotated by some angle, the electronic interference will exhibit a similar effect as that in optics and the LDOS on the surface would demonstrate some superstructure. Accordingly, considering the Moiré assumption, the superlattice observed here in Figure 6-4 (a) should possibly come from the Gr sheet rotation with respect to the Ni(111) substrate underneath,

because the tunneling current in an STM measurement is proportional to the LDOS on the sample surface and the STM image is a reflection of the surface LDOS. The Moiré pattern observed in Gr on the Ni(111) surface has been reported already by several researchers [164,170,182,184,205–207] and they all attribute the mechanism of the superlattice formation to the Moiré assumption in STM experiments. The relation between the Moiré superlattice periodicity *D*, the atomic spacing *d* of graphite and the Gr misorientation angle θ is expressed by $D = d/(2sin\theta/2)$ [201,208]. According to this equation, since d is known to be 0.246 nm [201], the superlattice periodicity of 3.157 nm should correspond to a rotation angle of 4.5°. The simulated pattern in Figure 6-4 (b) is also consistent to that measured by profile AB shown in Figure 6-4 (a). According to Ref. [182], at low temperature, after the cracking of hydrocarbon molecules, except for forming surface carbides, carbon atoms may also bond together directly on the nickel surface to nucleate and form Gr. The rotation of the Gr layer is due to thermal fluctuations in the low-temperature range [182]. This rotated-Gr (twisted-) area differs from most of the other areas of epitaxial Gr on the sample surface, as shown in Figure 6-3, and is not representative for the Gr arrangement on Ni(111) under such preparation conditions.

6.3.2 900-K-prepared graphene

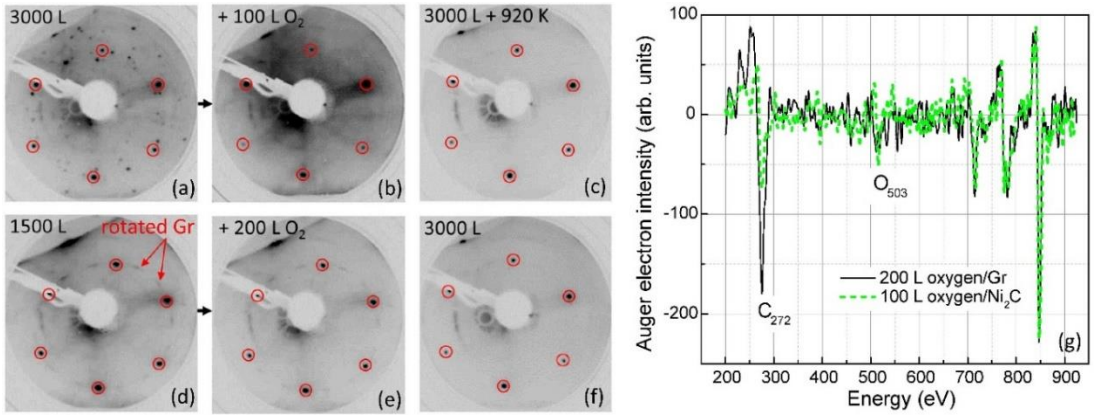

Figure 6-5 (a), (c), (d), (f) LEED patterns after Ni(111) was exposed to propylene at 900 K without subsequent annealing. (b), (e) LEED patterns after dosing 100 L and 200 L oxygen to the samples shown in (a) and (d), respectively. (g) Corresponding Auger electron $dN(E)/dE$ intensity for samples shown in (b) and (e). The sample in (c) was subsequently annealed at an elevated temperature of 920 K for 30 min immediately after dosing, while no subsequent annealing was performed for (f). Propylene dosing parameters: (a) 1×10^{-5} mbar for 5 min (3000 L), (d) 2.5×10^{-6} mbar for 10 min (1500 L), (c) 1×10^{-5} mbar for 5 min (3000 L), (f) 2.5×10^{-6} mbar for 20 min (3000 L). All LEED patterns were taken at room temperature and 149 eV. Red circles mark the (1×1) reciprocal hexagonal lattice of the Ni(111) substrate.

Gr growth at 900 K demonstrates a diversity under the influence of hydrocarbon-dosing rate (pressure), dosing time, and subsequent annealing procedure. Figure 6-5 (a) and (d) show LEED patterns after fast and slow dosing of hydrocarbon at 900 K. For the former, surface-carbide-generated superstructures on the LEED pattern can be seen clearly, while the latter exhibits two additional blurred spots in-between two (1×1) spots, where the angle between the superstructure spots appears to be about 20°. The pattern shown in Figure 6-5 (d) could be due to the rotated Gr on Ni(111) with a rotation angle of 20°. To further confirm the existence of Gr, 200 L oxygen was dosed and the resulting LEED pattern in Figure 6-5 (e) exhibits no obvious change compared to Figure 6-5 (e). On the contrary, after 100 L oxygen exposure of the nickel-carbide surface in Figure 6-5 (a), the carbide superstructures disappear and the background intensity is strongly enhanced, indicating an oxidized surface after the oxygen exposure. The AES for both oxygen-exposed surfaces in Figure 6-5 (g)

demonstrates that the carbon density on the surface in Figure 6-5 (d) is much higher than that in Figure 6-5 (a), as the two carbon peaks at 272 eV show, indicating a Gr-covered surface for Figure 6-5 (d) [186]. Except for the dosing rate, the subsequent annealing procedure also matters. By comparing Figure 6-5 (a) and (c) with the same dosing time and rate, because of the additional annealing procedure for (c), sharp (1×1) diffraction spots are seen, indicating the formation of Gr by converting the surface carbides. Figure 6-5 (d) and (f) have the same dosing rate, but the length of time for (f) is twice of that for (d), therefore, no additional spot is observed in (f), indicating a Bernal-stacked (AB-stacked) sequence [209] for Gr on Ni(111) in Figure 6-5 (f). To further understand the Gr growth at 900 K, real-space imaging of the sample surface is a direct way.

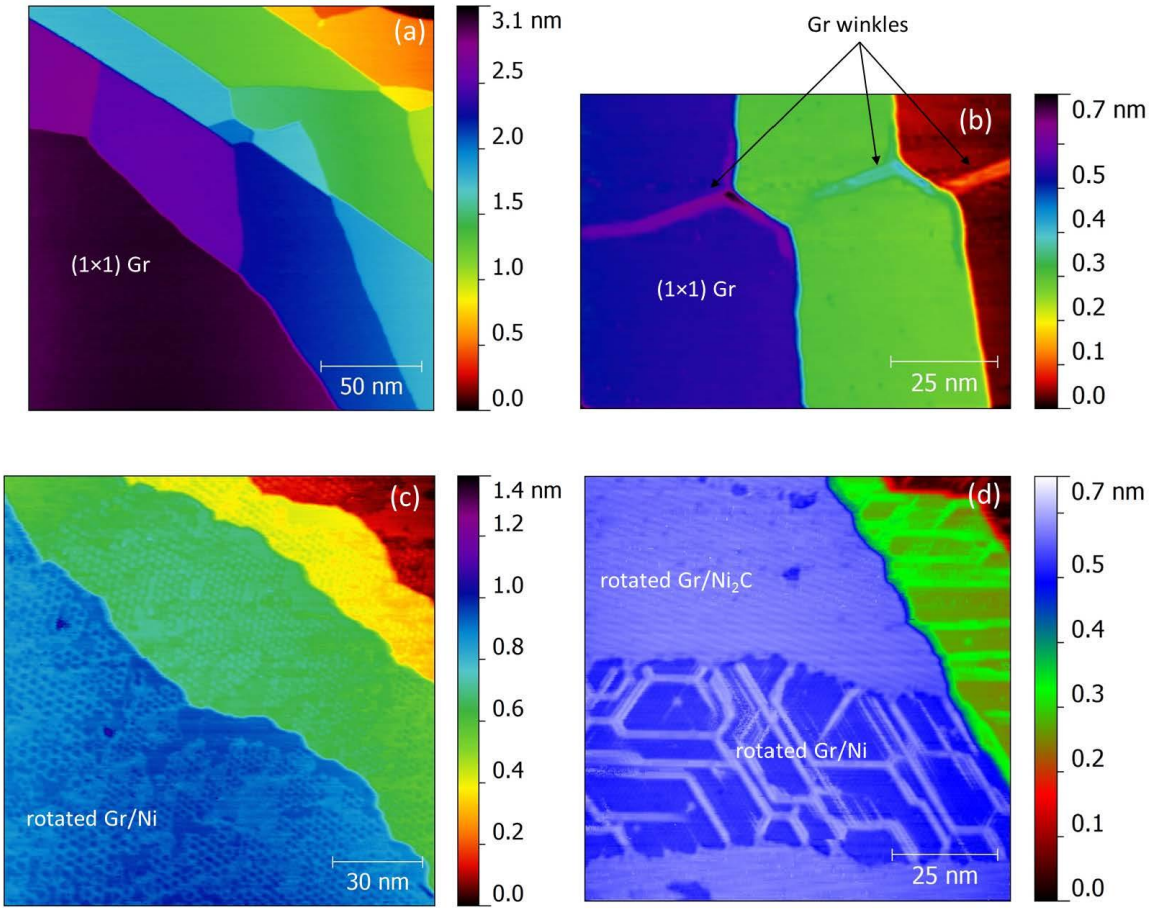

Figure 6-6 Corresponding constant-current STM images for the sample shown in Figure 6-5 (c). (a), (b) Mostly observed (1×1) Gr on the sample surface. (c), (d) Occasionally observed rotated Gr. Feedback parameters: (a) +1 V, 2.4 nA; (b) +0.81 V, 2.13 nA; (c) +1 V, 2.61 nA; (d) +0.99 V, 2.35 nA.

Figure 6-6 shows corresponding STM topography images of Figure 6-5 (c). As shown in Figure 6-6 (a) and (b), a similar morphology is also observed in most of the other areas on the sample surface. These areas only exhibit smooth and flat (1×1) Gr on Ni(111), as is consistent to the LEED patterns of Figure 6-5 (c). However, there are still some small exceptional areas that exhibit a different morphology, as shown in Figure 6-6 (c) and (d). In panel (c), rotated Gr on Ni(111) is observed, as the hexagonal Moiré superlattice on different steps illustrates. In contrast, panel (d) shows Gr on different substrates underneath. There are mainly two types of structures under the Gr layer, i.e., Ni(111) and Ni_2C. Similar topographies have also been observed before, i.e., the Gr/Ni_2C area exhibits stripe features and the Gr/Ni(111) area exhibits Moiré superlattices [182,206]. The formation of Ni_2C underneath the Gr layer is due to carbon segregation from the bulk. Such structures are only found underneath the rotated Gr layer [182]. The epitaxial Gr is bonded strongly on the nickel surface and no further carbon structure can be formed in between, however, the rotated Gr is physisorbed on the metal surface and the binding is not that strong as that of the epitaxial Gr [210], such that segregated carbon atoms could possibly form carbide structures under the rotated Gr layer [164,182,211,212]. This scenario is confirmed by the *in situ* observations [182] for high-temperature-grown Gr [181,182]. The previous assumption, namely, that the Ni_2C which forms prior to the topmost-rotated Gr layer is the reason for the rotation of Gr [206], turns to be not satisfying for the explanation of high-temperature Gr growth because of the instability of surface carbides.

The carbon concentration is an important factor for the Gr growth at high temperatures. According to Ref. [164], to nucleate Gr directly on the nickel surface at high temperatures needs a high carbon concentration in the substrate. Once this concentration is reached, Gr will start to grow. Higher temperature growth may also increase the fraction of rotated Gr on Ni(111) [164,182,212]. The type of structure that will be formed under the rotated Gr layer by further segregating carbon atoms depends on the bulk carbon concentration [164,182]. If the concentration is not high enough to form another Gr layer, carbides will grow instead, as shown in Figure 6-6 (d).

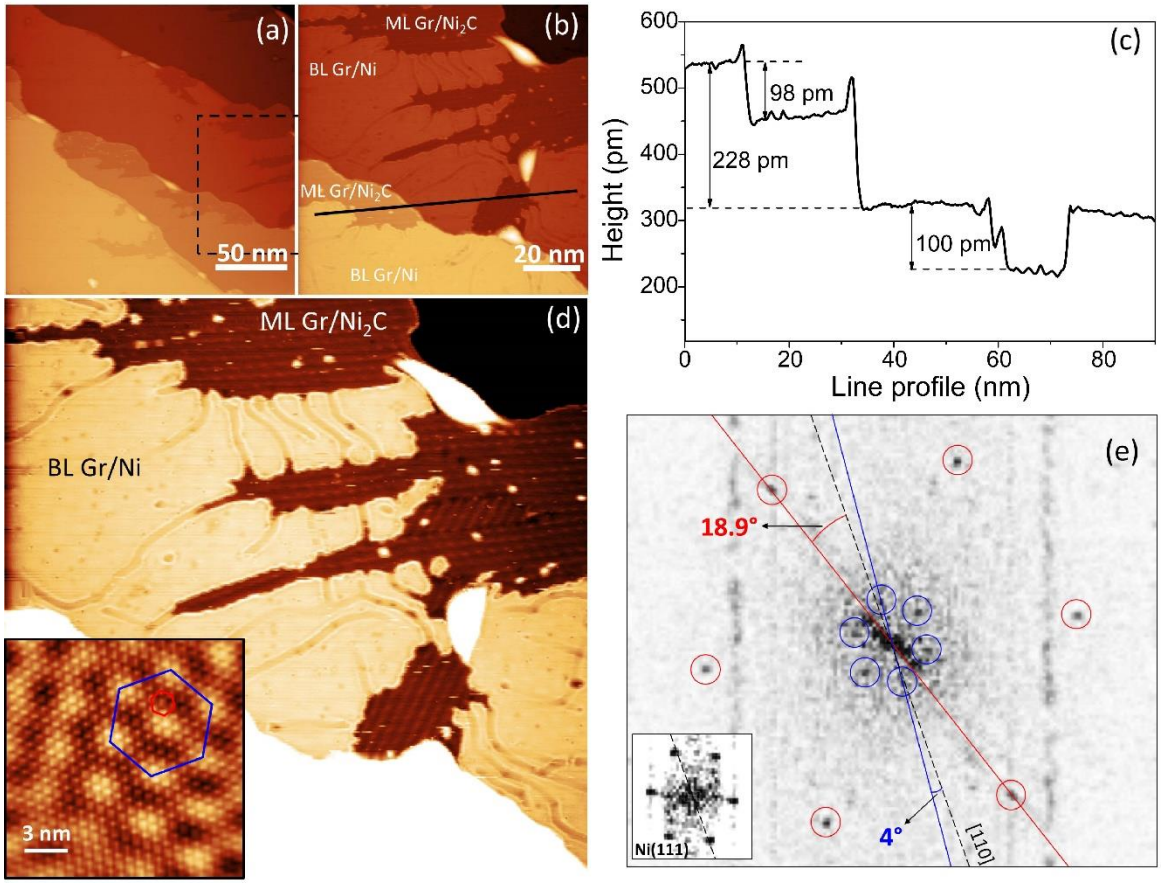

Figure 6-7 (a), (b), (d) Constant-current STM images corresponding to the sample shown in Figure 6-5 (f). Feedback parameters: +1.1 V, 0.49 nA. Part of (b) shows the zoomed-in image of the area marked by dashed rectangle in (a). (c) Line profile for the black line in (b). (d) illustrates the same area as (b) but with enhanced image contrast on one terrace. The inset is the 2D FFT-filtered area for the BL Gr/Ni(111). (e) 2D FFT of the BL Gr area in (d). The inset of (e) is the 2D FFT of Ni(111) in Figure 5-2 (a). The dashed black line demonstrates the [110] direction of the Ni(111) substrate. Red and blue circles mark the two superlattices caused by the misorientation of the two non-Bernal-stacked Gr layers.

Compared with the ML Gr on Ni_2C in Figure 6-6 (d), the STM images in Figure 6-7 illustrate not only ML Gr/Ni_2C/Ni(111), but also bilayer (BL) Gr/Ni(111). As seen in Figure 6-7 (d), the ML Gr on Ni_2C areas exhibits similar structures as Ni_2C/Ni(111), where the stripe spacing of 1.65 nm [206,213], while the spacing here is 1.6–2 nm which is close to the Ni_2C spacing. For the BL Gr/Ni(111) region, the 2D FFT in Figure 6-7 (e) demonstrates two sets of hexagonal patterns, as the red and blue circles illustrate. The inset of Figure 6-7 (d) is the 2D-FFT filtered [using the two sets of hexagonal superlattices

marked by red and blue circles in Figure 6-7 (e)] image for the BL Gr region. There are two different periodic superlattices with six-fold symmetry, as the blue and red hexagons show. The blue and red hexagons correspond to two sets of patterns marked by the same colors in Figure 6-7 (e). The real-space periodicities are 0.75 nm and 3.55 nm, respectively. These two superlattices are due to the non-Bernal stacking of two Gr layers with the rotation angle of 18.9° and 4° with respect to the [110] direction of the Ni(111) substrate. The calculated angles are also consistent with the rotation angles for the two sets of patterns in Figure 6-7 (e). The misorientation angle between the two Gr sheets should then be 22.9°, accordingly. From the line profile across two nickel terraces in Figure 6-7 (c), on the same terrace the BL Gr area is about 1 Å higher than Gr on Ni_2C area. The monolayer rotated Gr is weakly bonded to Ni_2C and the ML Gr/Ni_2C is about 0.85 Å higher than the physisorbed ML Gr/Ni(111), as will be shown in Figure 6-12 later. The topmost Gr layer in the BL Gr system demonstrates to be quasi-freestanding [214,215] and has a semimetallic behavior [216]. Ni_2C exhibits metallic character [217] and to explore the electronic interaction between Ni_2C and Gr on top will be an interesting topic in the future.

In a word, 900-K-prepared Gr exhibits diverse phases, including (1×1) epitaxial Gr and Gr with some certain degrees of rotation. Since the latter bonds relatively weaker with the Ni(111) surface, the formation of further carbon structures like Ni_2C and another Gr may occur via bulk carbon segregation, leading to even more complicated structural configurations.

6.4 Properties of 900-K-prepared rotated graphene

In order to understand properties of 900-K-prepared rotated Gr, this section will only select rotated Gr areas and focus on diverse Moiré pattern periodicities and corrugations, as well as Gr's electronic properties influenced by different carbon structures underneath. All samples shown in this section were prepared under condition (2).

6.4.1 Multi-periodic superlattices of rotated graphene on Ni(111)

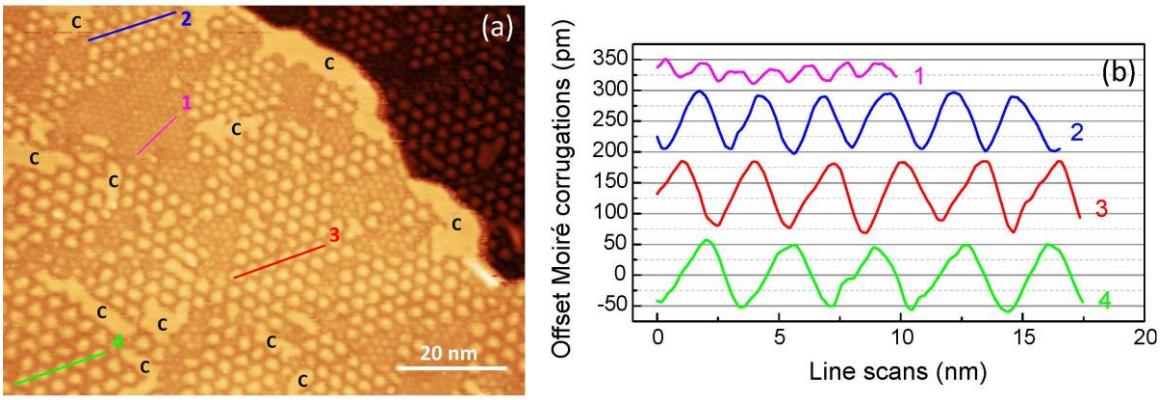

Figure 6-8 (a) Constant-current STM image for a ML of rotated Gr/Ni(111) (+0.2 V, 2.6 nA). Areas marked by "C" illustrate Gr on Ni_2C. (b) Line scans for lines marked with the same numbers in (a).

The monolayer rotated (twisted) Gr has a relatively weak bonding to the supporting Ni(111) surface compared to the epitaxial Gr/Ni(111) [210,212]. Because of the carbon concentration difference in the bulk, further segregated carbon atoms may form Ni_2C or a second layer Gr between the rotated Gr and the nickel surface. A Gr-covered surface with Moiré superlattices of different periodicities is shown in Figure 6-8 (a). There are mainly four types of Moiré patterns. Line scans 1, 2, 3, 4 illustrate periodicities of 1.45 nm, 2.6 nm, 3.04 nm, 3,54 nm, which correspond to rotation angles of 9.8°, 5.4°, 4.6°, 4°, respectively. Between two adjacent grains of dissimilar Moiré periodicities, no distinct boundaries can be found, which differs from the STM observation of beads-like boundaries [218–225] between AB-stacked Moiré regions and AA-stacked non-Moiré regions on graphite. The beads-like boundary is due to the chiral edge states of twisted BL graphite sheets in AB-stacked regions [225], which should not be the case here in Figure 6-8 (a). Once Gr starts to nucleate on Ni(111), the subsequent growth will follow the once-started stacking sequence. In the STM image here, the multiperiodic Moiré patterns are probably due to different rotation angles for different Gr nucleation centers at the very beginning of the growth, such that after the small fragments of Gr get bonded to each other and form a whole sheet, the as-grown patterns are formed. Accordingly, due to the misorientation of the adjacent Gr patches, at the boundary positions, defects or dislocations are likely to exist [226–228].

Moreover, amplitudes of the observed Moiré patterns show significant difference with respect to the periodicity. Smaller periodicity, as profile 1 shows, corresponds to larger rotation angle and demonstrates a much smaller amplitude of 40 pm compared to that of 114 pm for profile 4. This rotation-angle-dependent Moiré pattern corrugation indicates a periodic electronic-interaction tuning effect by modulating the Gr orientation with respect to the supporting substrate and might attract interest for applications in molecule or cluster self-assembly.

The areas marked with "C" are similar to those reported in Ref. [170], which have been interpreted as pure Ni_2C that could be further converted into Gr. However, this interpretation proves to be a misidentification of Gr/Ni_2C in the supplementary material of Ref. [206]. The morphology of Gr/Ni_2C does not have any Moiré pattern with the hexagonal symmetry and is formed from a honeycomb lattice on a quasi-square lattice [206]. Accordingly, here the areas marked with "C" are supposed to be Gr-covered Ni_2C, which originates from bulk carbon segregation. The electronic and structural properties of these regions will be discussed in the following sections.

6.4.2 Bias dependence of apparent corrugation of the rotated graphene superlattice

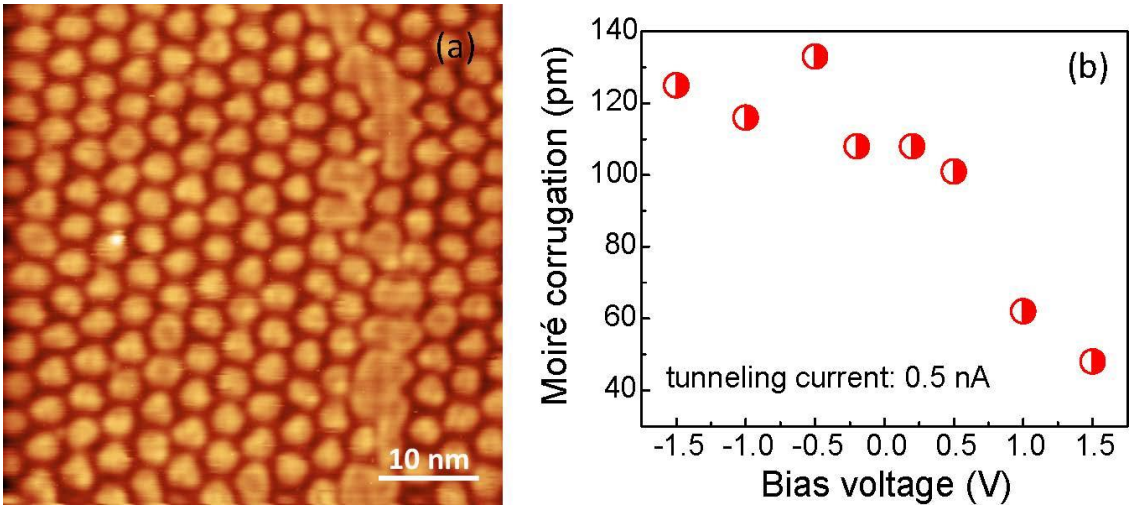

Figure 6-9 (a) Constant-current STM image for ML Gr/Ni(111) (+1.0 V, 0.5 nA). (b) Moiré corrugation for the rotated Gr shown in (a) at different bias voltages.

As mentioned in the last section, the Moiré corrugation varies with the Gr rotation angle. Since the rotated Gr sheet is only physisorbed on the Ni(111) substrate, the electronic interaction between the ML Gr and the nickel surface is relatively weak compared to chemisorbed Gr [182,206,210]. Figure 6-9 (a) shows an STM topography for a ML of rotated Gr/Ni(111). By varying the bias voltage from -1.5 V to +1.5 V, the amplitude of the Moiré corrugation exhibits a decreasing tendency from 125 pm to 48 pm. A similar phenomenon has been reported in the Gr/Ru(0001) system [229,230]. The electronic effect proves to play an important role for compensating the surface Moiré corrugation by 0.16 nm [231,232] for Gr/Ru(0001). Later on, atomically-resolved STM imaging and DFT calculations for the same system revealed that STM images at low bias voltages mainly reflect the geometrical corrugation while at higher voltages, an electronic resonance state has significant influence on the periodic distribution of the LDOS and local work function of Gr [233]. An angle-resolved photoemission spectroscopy (ARPES) study on epitaxial Gr on Ni(111) revealed that the Dirac cone is downward-shifted by 2.84 eV to a higher binding energy with respect to that for the freestanding Gr sheet because of the hybridization of the Gr π orbital and nickel 3*d* states [189]. Although shifted, the Dirac cone remains intact and no gap opening is found at the Dirac energy [189]. The Dirac cone down shift was also discovered elsewhere by about 2.0 eV compared to the quasi-freestanding Gr layer [41]. This small shift indicates a strong *n*-type doping in Gr from dynamical hybridization for Gr on Ni(111) and Co(0001) surfaces [189], which influences the charge transfer from nickel to Gr. As to the rotated Gr on Ni(111), a hybridization of the Gr π band and the nickel 3*d* band could also occur and thus modify the electronic properties of Gr [210]. The dynamic hybridization between nickel 3*d* and Gr exhibits an energy-dependent behavior which might change the doping level in Gr at different energies [189] and have an impact on the charge transfer from metal to Gr [234]. Accordingly, in Figure 6-9 (b), the observed reduction of the Moiré corrugation at higher bias voltages could be due to an electronic effect which might be caused by the varied charge transfer from the metal substrate.

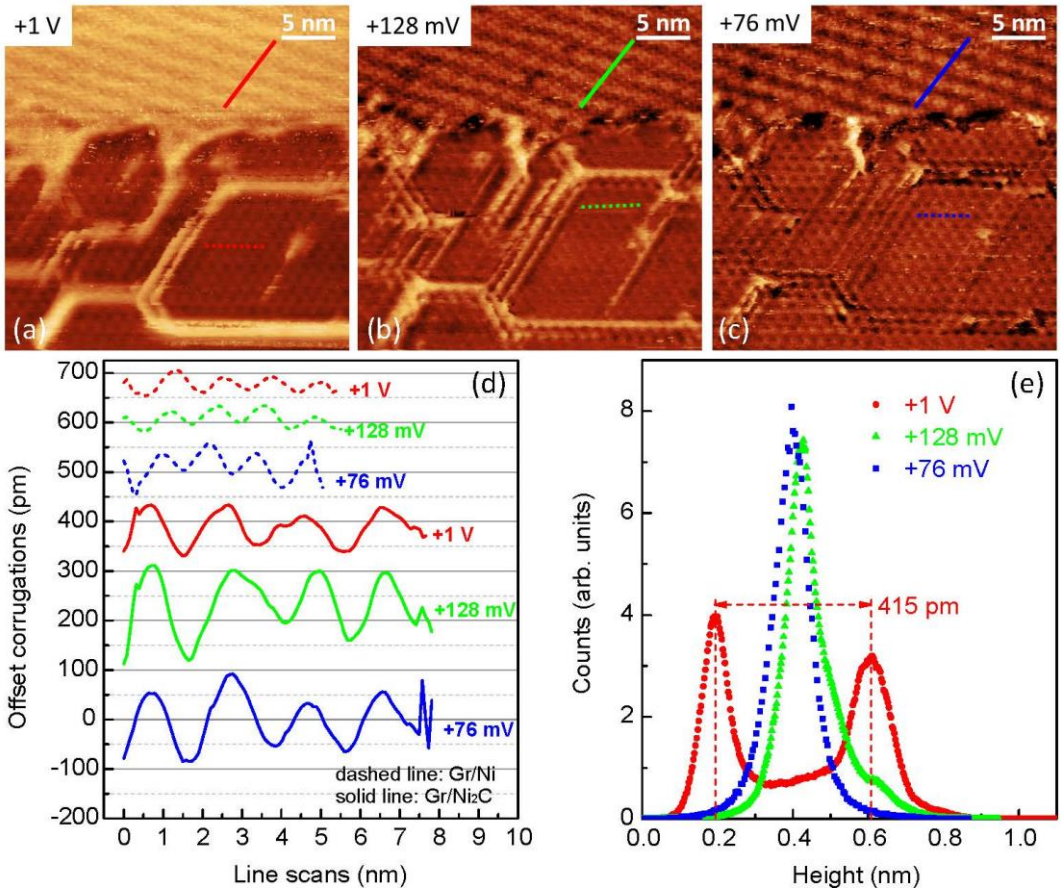

Figure 6-10 (a), (b), (c) Constant-current STM images for rotated ML Gr at +1V, +128 mV, +76 mV, respectively. Feedback current: 2.35 nA. (d) Line scans for lines in (a), (b), (c). (e) Histograms for (a), (b), (c).

STM pictures are not only imaging the structures on the surface, but also screening the underlying structures that also contribute to the surface electron distributions [202]. The upper part of the STM images in Figure 6-10 show the Gr-covered Ni_2C area, while the lower part consists of rotated Gr/Ni(111) with Moiré periodicity of about 1.22 nm. At different bias voltages, the two areas demonstrate distinct corrugation behaviors and in general, the Gr in contact with Ni_2C demonstrates a larger corrugation with a periodicity of 1.95 nm, which is close to the reported value for Gr/Ni_2C [206,213]. For a lower bias voltage of +76 mV, both upper and lower areas demonstrate high corrugations of 175 pm and 90 pm, respectively, while at +1 V, the corrugation is reduced by 78 pm and 37 pm. Moreover, at +128 mV the Gr/Ni(111) turns out to have a similar corrugation as at +1 V, but the Gr/Ni_2C still maintains a similar amplitude as at the lower bias voltage of +76 mV. Histograms for the two different regions in Figure 6-10 (e) show that there is an apparent

step height of about 415 pm between Gr/Ni(111) and Gr/Ni_2C at the bias voltage of +1 V, while this step vanishes close to the Fermi energy. This phenomenon clearly shows that there is an electronic charge inhomogeneity between the two regions. In the areas with Ni_2C underneath the Gr, nickel *d* orbitals bond carbon 2*p* orbitals, which could drastically modify the electronic environment for the Gr sheet and the corresponding doping. Compared to the quasi-freestanding topmost layer of BL Gr or graphite, Gr/Ni_2C might also possess some degree of "free-standing" property with less influence of the 3*d* metal, and the interacting force between Gr and Ni_2C might not necessarily be that weak as Van der Waals interaction between Gr layers. Compared to the intercalation of Gr by metal [40–42,235–249] or nonmetal [43,44,250–254] clusters, the Ni_2C-introduced decoupling of Gr from the contacting surface might be another topic of interest for future studies.

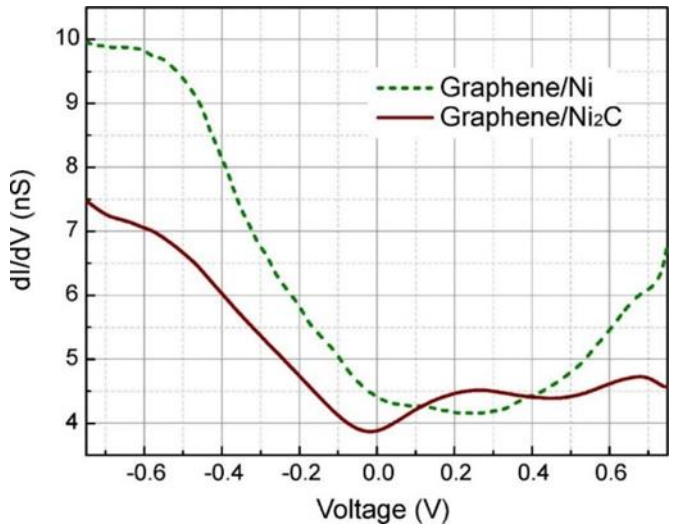

Figure 6-11 STS curves for Gr/Ni(111) (dashed line) and Gr/Ni_2C/Ni(111) (solid line) taken from respective areas in Figure 6-10. Feedback parameters: +0.5 V, 2.35 nA.

When Ni_2C is formed between the nickel surface and the rotated Gr layer, the LDOS for Gr is completely changed, as the STS curves in Figure 6-11 show. Below the Fermi energy, because of the intercalated Ni_2C, the occupied LDOS is reduced compared to that without Ni_2C in between. At the bias voltage of about +0.2 V, the STS curve for Gr/Ni_2C region exhibits a peak. Around this energy the density of unoccupied states is slightly higher than that in Gr/Ni(111). Since the carbon 2*p* orbitals in Ni_2C bond nickel 3*d* orbital, the hybridization between nickel 3*d* and Gr π orbitals might be weakened, which could be one

possible reason for higher density of the unoccupied states at energies near 0.2 eV and lower occupied states of Gr/Ni_2C.

6.4.3 Tunneling-gap and orientation effect on rotated graphene on Ni_2C

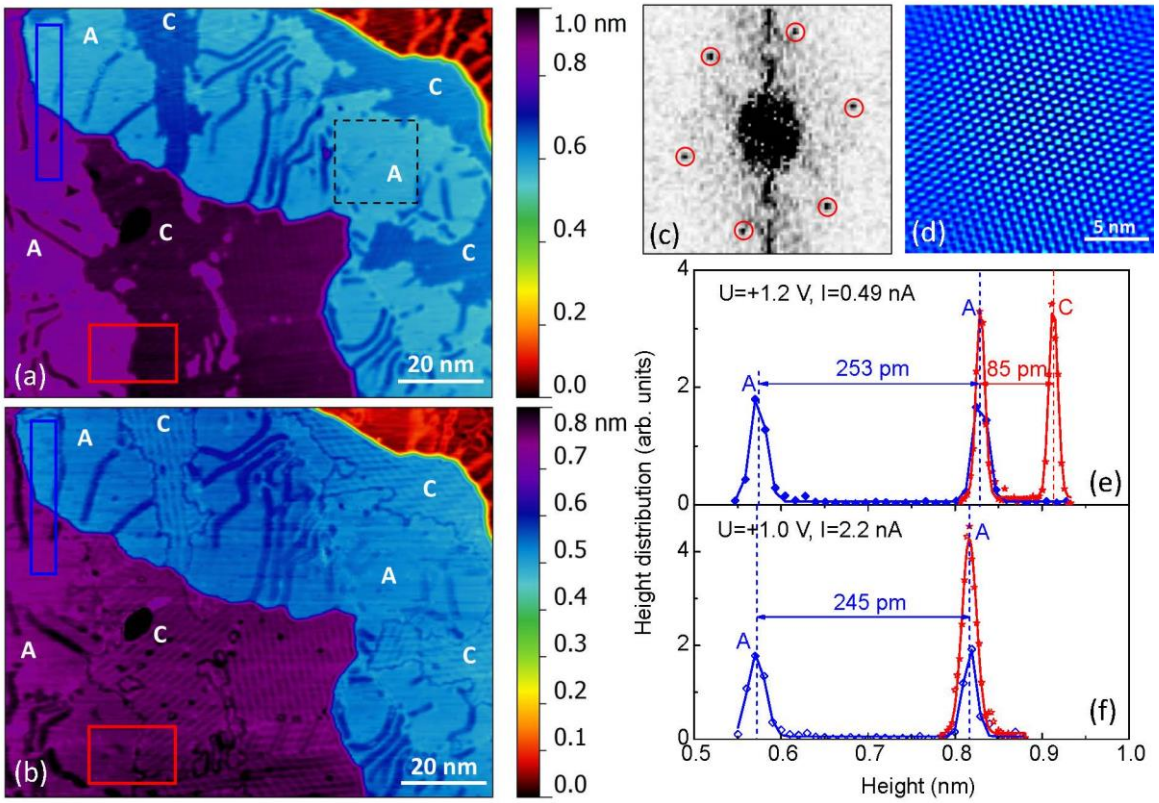

Figure 6-12 (a), (b) Constant-current STM images of a rotated ML Gr. Feedback parameters: (a) +1.2 V, 0.49 nA; (b) +1.0 V, 2.2 nA. Areas marked with "A" and "C" represent Gr/Ni(111) and Gr/Ni_2C/Ni(111), respectively. (c) 2D FFT of part of area A as marked by dashed square in (a) and the corresponding 2D-FFT-filtered [filtered by the selected hexagonal spots marked by red circles in (c)] image (d). (e), (f) histograms for areas marked with blue and red rectangles in (a) and (b).

The electronic environment of rotated Gr in direct contact with Ni(111) differs from that in contact with Ni_2C, as the discussion about the bias-dependence above illustrate. In the STM experiment, the tunneling gap also plays an important role in tuning the electronic properties of the surface. Here STM images in Figure 6-12 (a) and (b) are from almost the same area at similar bias voltages, but the tunneling gap resistance is different [2449 MΩ for (a) and 455 MΩ for (b)]. Three terraces are exposed and on each terrace there are two

different areas which are identified as Gr/Ni(111) (areas marked with "A") and Gr/Ni_2C (areas marked with "C"). The 2D FFT of area A is shown in Figure 6-12 (c) and the corresponding filtered image exhibits a Moiré superlattice with a period of about 0.72 nm, which corresponds to a rotation angle of 19.7° of the Gr sheet. Histograms shown in Figure 6-12 (e) and (f) illustrate that when there is a larger tunneling-gap resistance (2449 MΩ), area C demonstrates to be 85 pm higher than area A, while the apparent height difference vanishes when the tunneling-gap resistance is reduced to 455 MΩ. Nevertheless, the tunneling-gap resistance has a much smaller influence on the height difference between areas with only Gr/Ni(111) configuration on two adjacent terraces, which is close to the interlayer distance of the fcc Ni(111) single crystal. The tunneling-gap-resistance-change-caused disappearance of the height difference between areas A and C further indicates that the interaction between Gr and Ni_2C can be drastically tuned electrically by the tunneling electrodes. Moreover, in Figure 6-12 (b) the tunneling-gap resistance is quite close to that in Figure 6-10 (a), but the latter exhibits a large height difference of 415 pm between areas of Gr/Ni(111) and of Gr/Ni_2C, while the former does not. The two seem to contradict each other, but when considering the rotation angle of the two Gr sheets, the difference is obvious. As already known, the Moiré periodicity for Gr/Ni(111) in Figure 6-10 (a) is 1.22 nm, which corresponds to a rotation angle of 11.6°, while the rotation angle in Figure 6-12 (b) is 19.7°. After the formation of a rotated single-layer Gr, the subsequently formed Ni_2C underneath [182] should not change the original orientation of Gr. Therefore, with similar gap resistance, the reason for the difference between Figure 6-10 (a) and Figure 6-12 (b) should be the different orientation angle of Gr with respect to the Ni(111) substrate. Different orientation angles exist for the twisted-BL-Gr Moiré patterns because the topmost Gr layer is quasi-freestanding and the rotation angle is independent of the interlayer potential [214]. But here the Gr/Ni_2C demonstrate rotation-angle-dependent electronic properties, reflecting an orientation-dependent interaction between Gr and Ni_2C. Both Gr/Ni_2C areas in Figure 6-10 and Figure 6-12 demonstrate a common feature, that is, the step height between Gr/Ni(111) and Gr/Ni_2C vanishes after reducing the tunneling-gap resistance, which could be because with a smaller gap resistance, the tunneling electrons mainly reflect the geometrical structure of the surface, and with a larger gap resistance the electronic structure is dominating.

6.5 Tuning the electronic properties of rotated graphene on Ni_2C with oxygen

Gr on Ni_2C exhibits distinct electronic property difference compared with ML Gr/Ni(111) as discussed in section 6.4. In this section, oxygen influence of the electronic properties of BL Gr observed together with single layer Gr/Ni_2C are discussed. Gr/Ni_2C in this section was prepared under condition (3).

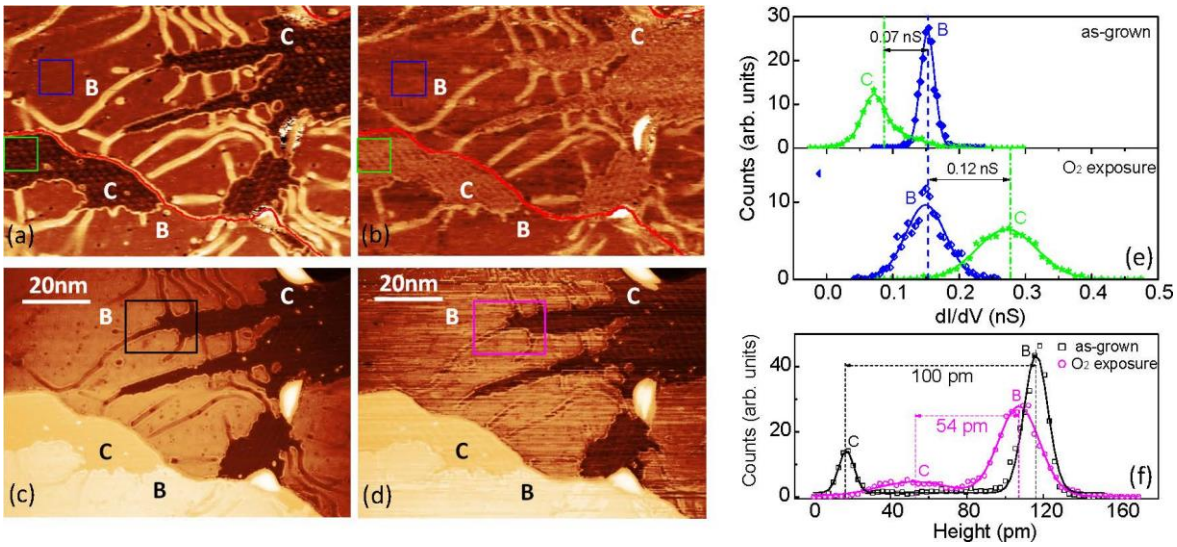

Figure 6-13 (a), (b) Constant-current STM differential conductance maps for pristine Gr and Gr exposed by 1050 L oxygen. (c), (d) Simultaneously recorded topographies for (a), (b). The scanning area is from the same position as shown in Figure 6-7 (d). Feedback parameters: +1.0 V, 0.5 nA. Areas marked with "B" and "C" represent BL Gr/Ni(111) and ML Gr/Ni_2C/Ni(111), respectively. (e) Top and bottom are histograms for the areas marked by blue and green squares in (a) and (b). (f) Histograms for areas marked with black and pink rectangles in (c) and (d). Red lines in (a) and (b) illustrate terrace borders. Vertical dashed lines represent averaged values for the statistic areas.

The STM images shown in Figure 6-13 are from a similar area as those shown in Figure 6-7 (b) and display the coexistence of BL Gr/Ni(111) and ML Gr/Ni_2C. In the bottom panel of Figure 6-13, (c) and (d) are topographies for the same area before and after 1050 L oxygen dosing at room temperature, in the top panel, (a) and (b) are simultaneously recorded *dI/dV* maps. To analyze quantitatively, histograms in Figure 6-13 (e) show the

differential conductance change before and after oxygen exposure for area B [BL Gr/Ni(111)] and area C [ML Gr/Ni_2C/Ni(111)]. The differential conductance in area B is 0.07 nS higher than that in area C for the as-grown surface, while the contrast reverses after oxygen exposure and the differential conductance for Gr-covered Ni_2C area is 0.19 nS higher than before. Nevertheless, the BL Gr/Ni(111) area stays unchanged, which is consistent to a previous study on the Gr passivation of the Ni(111) surface [165] and the unchanged differential conductance also implies similar tip conditions after oxygen exposure. Moreover, histograms for the corresponding topographies also demonstrate a relative height reduction of 46 pm between areas B and C by the oxygen influence, as seen in Figure 6-13 (f).

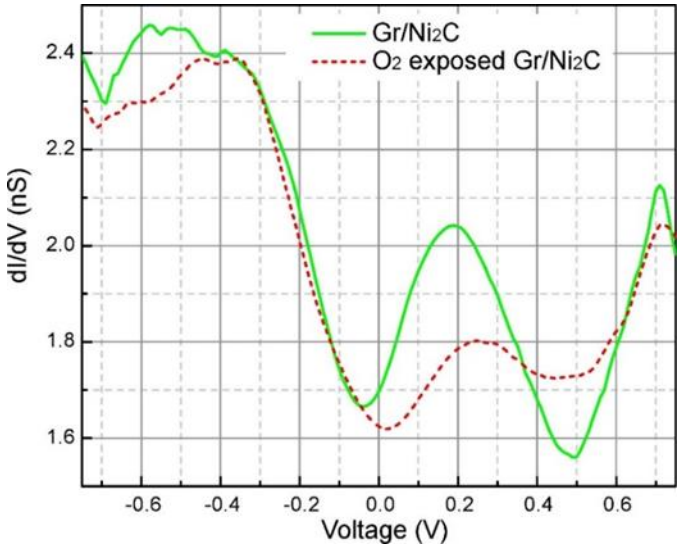

Figure 6-14 STS of pristine (solid line) and 160 L oxygen exposed (dashed line) Gr/Ni_2C/Ni(111). Feedback parameters: +0.5 V, 1.8 nA.

The STS curves for the Gr/Ni_2C area shown in Figure 6-14 indeed illustrate a distinguished electronic modification after a small amount of oxygen dosage. In the spectra here, a similar peak at +0.2 V as the one shown before in Figure 6-11 is reduced after dosing oxygen, indicating a decrease in the unoccupied states, whereas the valley at +0.5 V is higher than before. Considering together the higher contrast level of the Gr/Ni_2C region in Figure 6-13 (b) (bias voltage: +1.0 V), it seems that above the Fermi energy, there is a *dI/dV* contrast oscillation with energy before and after oxygen exposure, as seen in Figure 6-14. The STS curves also illustrate that oxygen mainly influences the unoccupied states but has little

influence on the occupied states near the Fermi level. This electronic modification of Gr/Ni_2C by oxygen suggests that due to the existence of Ni_2C between Gr and the nickel substrate, the Gr passivation effect fails. One possible scenario could be the intercalation of oxygen between Gr and Ni_2C, and the subsequent oxidation of Ni_2C under the Gr layer changes the electronic contacting environment. According to previous studies on the oxygen intercalation between Gr and the metal surface, the intercalation normally occurs at temperatures higher than room temperature [44,250,251,253–255]. Therefore, it seems that this scenario is not very likely, but the possibility cannot be ruled out. Another scenario could be that due to the formation of Ni_2C, there are some electronic defects introduced in the topmost Gr layer, which locally modify the energy barrier of the Gr surface and trap oxygen at these defect sites [256]. Since Ni_2C exhibits a periodic structure [182,206], if such Ni_2C-introduced defects in the topmost Gr layer exist, the Gr layer may exhibits some periodic defects and these defect sites may act as a quantum dot array, which would facilitate the application in Gr-based electronic devices.

6.6 Sub-monolayer Mn on graphene on Ni_2C

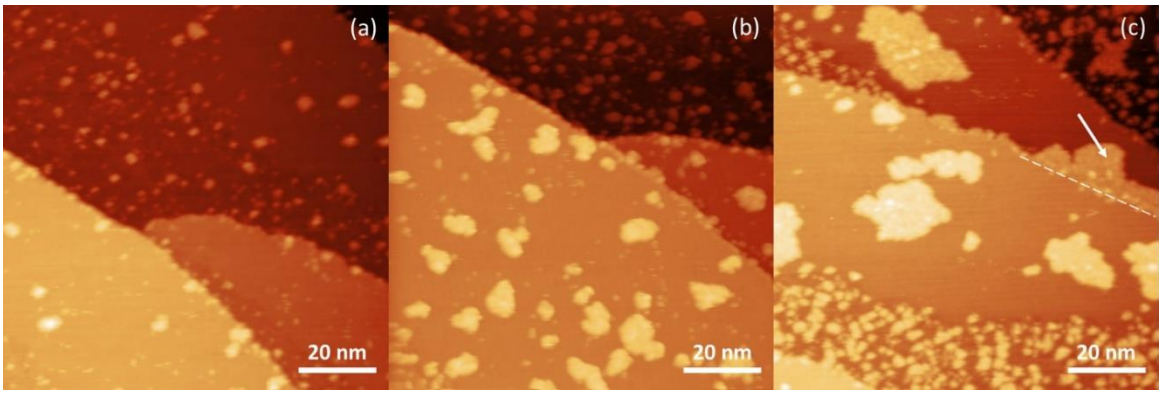

Figure 6-15 Constant-current STM topography images of room-temperature deposited Mn on ML Gr/Ni_2C/Ni(111) at thicknesses of 0.1 ML (a), 0.2 ML (b), 0.4 ML (c). Feedback parameters: (a) +1.0 V, 2.0 nA; (b) +1.0 V, 1.8 nA; (c) +0.5 V, 2.1 nA. The dashed white line indicates the Gr edge.

Mn was deposited on 900 K-prepared Gr at room temperature and STM images in Figure 6-15 show Mn coverages of 0.1 ML (a), 0.2 ML (b) and 0.4 ML (c), respectively. At the beginning of the growth, Mn atoms form small clusters and some atoms start to decorate the step edges. When the coverage increases, large Mn patches are formed without any

regular shape on Gr/Ni_2C, but on the Gr/Ni(111) region, only small islands are seen. The areas with Gr/Ni_2C are identified by higher-resolution STM scanning and will be shown later. In Figure 6-15 (c), the area marked by an arrow corresponds to a patch of Mn on Gr/Ni_2C, which is attached to a higher step edge. According to the surface morphology of Mn deposited on Gr/Ni_2C shown in Figure 6-15, it can be seen that Mn exhibits a 2D growth mode in this sub ML range.

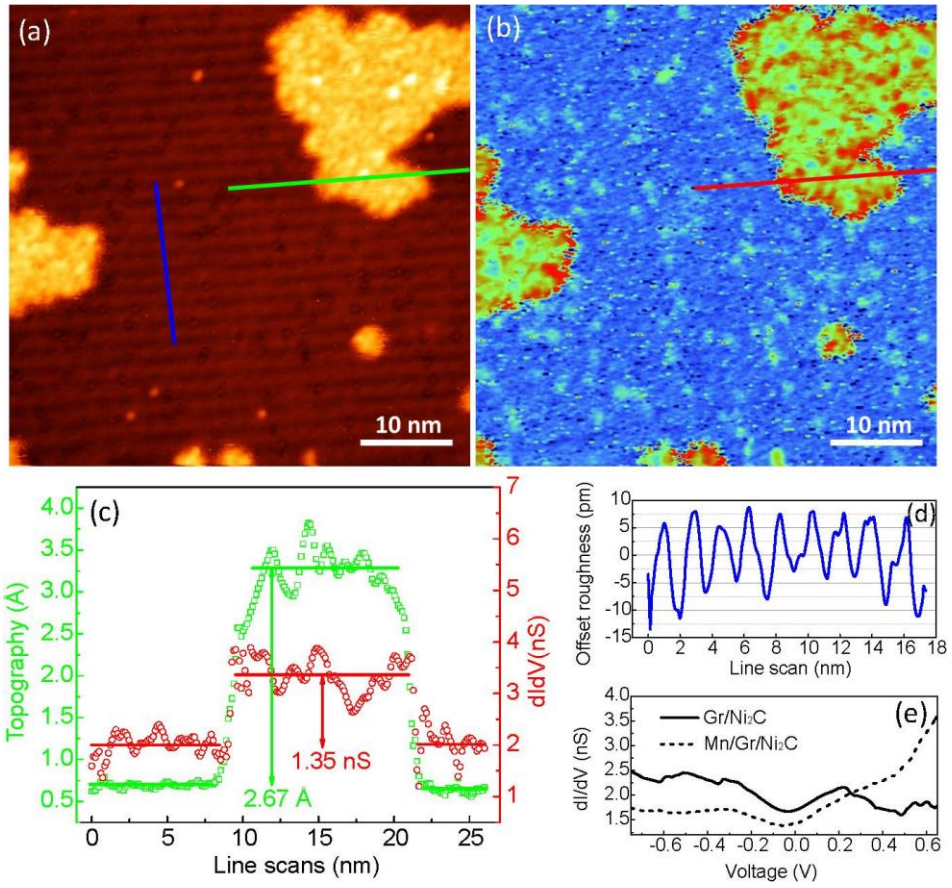

Figure 6-16 (a) Constant-current STM topography for 0.4 ML Mn on Gr/Ni_2C/Ni(111), and the simultaneously recorded dI/dV map (b). Feedback parameters: +0.5 V, 2.2 nA. (c) Line scans across Mn island in both (a) (green open squares) and (b) (red open circles). (d) Line scan for Gr/Ni_2C/Ni(111), as marked by the blue line in (a). (e) Area-averaged STS curves for Gr/Ni_2C/Ni(111) (solid line) and Mn/Gr/Ni_2C/Ni(111) (dashed line). Feedback parameters: +0.5 V, 1.9 nA.

In the upper panel of Figure 6-16, zoomed-in STM images with higher resolution are shown. Figure 6-16 (a) illustrates the topography of Mn patches deposited on Gr/Ni_2C/Ni(111) areas and Figure 6-16 (b) is the simultaneously recorded differential conductance map. The

Gr/Ni_2C template can be identified by the stripe-like corrugation that has been reported already elsewhere [182,206] with a periodicity of 1.87 nm, known from the line scan in Figure 6-16 (d), which corresponds to the blue line in Figure 6-16 (a). According to the surface line profile across the Mn island in Figure 6-16 (a), the height of the Mn island on such template is 2.67 Å, which is close to the value of the interlayer distance of the fcc Ni(111) substrate and indicates a close-packed stacking structure of Mn atoms inside the island. The same line profile at the same position in the *dI/dV* map illustrates a contrast of 1.35 nS between Mn and the Gr/Ni_2C surface. The differential conductance of the Mn island turns out to be larger than of the Gr/Ni_2C surface at the bias voltage of +0.5 V at which the *dI/dV* map was acquired. This result is consistent with the STS curves shown in Figure 6-16 (e). Other than the Mn-uncovered Gr/Ni_2C area in Figure 6-16 (a), the corresponding *dI/dV* map does not show any stripe-like pattern. The corrugation observed in the Gr/Ni_2C area of Figure 6-16 (a) might be from the geometric structure, while the absence of such corrugation in the differential conductance map is an indication of an electronic homogeneity on the Gr surface. The contrast between Mn island and the Gr/Ni_2C area shown in Figure 6-16 (b) could originate from the chemical difference. Moreover, since here a spin-polarized Fe ring-shaped probe with an in-plane magnetic sensitivity [88,118] is used for the STM measurement and Gr on nickel leads to perfect spin filters [27,189], it is likely that the observed differential conductance contrast between Gr/Ni_2C and the Mn surface also contains magnetic information. The STS curve for Gr/Ni_2C shown in Figure 6-16 (e) demonstrates a similar peak at +0.2 V as discussed before in Figure 6-11and Figure 6-14, and the contrast reversal occurs at around +0.25 V. To separate magnetic contrast from chemical contrast, the current technique used in the experiments described in this thesis is not sufficient and other ways, such as in-situ switching of the scanning probe magnetization direction by modulating the current applied in a magnetic coil wound around the probe [75,81,257,258] or external magnetic field switching of the probe if the sample remains unaffected [55] could be effective.

6.7 Summary and outlook

In this chapter, the growth of Gr on Ni(111) was studied comprehensively and the preparation conditions, such as temperature, hydrocarbon gas dosing rate, or dosing time,

may influence drastically the Gr quality. A summary of different preparation conditions related to figures in this chapter is listed in the following table.

Table 6-1 Summary of Gr preparation conditions

Temperature	Propylene dosage	Annealing	Surface structure	Figures
800−840 K	600-1800 L	800−840 K, 4−10 min	mostly: (1×1) Gr	6-3
			occasionally: rotated Gr	6-4
900 K	1×10^{-5} mbar, 5 min (3000 L)	no	surface carbides	6-5(a)
		920 K, 20 min	mostly: (1×1) Gr	6-5(c), 6-6(a)&(b)
			occasionally: rotated Gr, Gr/Ni_2C	6-6(c)&(d), 6-8, 6-9, 6-10, 6-11, 6-12
	2.5×10^{-6} mbar, 10 min (1500 L)	no	rotated Gr	6-5(d), 6-14
	2.5×10^{-6} mbar, 20 min (3000 L)	no	mostly: (1×1) Gr	6-5(f)
			occasionally: BL Gr, Gr/Ni_2C	6-7, 6-13

The Gr growth on Ni(111) is quite different from that on Cu(111) [180,259]. Because of the strong hybridization between 3*d* nickel and Gr electronic states, the growth cannot be well controlled and the wafer-level quality is not easy to achieve for the requirement of industrial applications. Gr preparation under condition (1) favors the formation of epitaxial (1×1) Gr with strong chemical bonding with the Ni(111) substrate, while under condition (2) and (3), the percentage of rotated Gr is increased, although the epitaxial Gr still covers most of the surface. Surface carbides are stable at temperatures below 840 K and after the surface is saturated with a carbide layer, the Gr growth will be blocked, nevertheless, allowing long enough annealing time at temperatures above 800 K facilitates the conversion of carbides into Gr. At 900 K, the carbide cannot saturate the surface, instead, carbon firstly diffuses into the bulk and resegregates once Gr nucleation starts on the surface. Once the Gr sheet terminates the surface, whether the later-on resegregated carbon will form further structures underneath the Gr layer or not depends on the bonding force between Gr and the substrate. Due to the strong chemisorption, carbon-related structures are not favored under epitaxial Gr/Ni(111). In contrast, the bonding between physisorbed Gr and the nickel surface is much weaker, which facilitates further carbon structure

formation. The type of carbon-segregation-formed structure underneath the rotated Gr depends on the bulk carbon concentration: lower concentration leads to Ni_2C and higher concentration will form a second layer Gr. Focusing on special regions on 900-K-prepared Gr, both Ni_2C and a second Gr layer are observed underneath the rotated ML Gr. The Gr/Ni_2C areas exhibit quite different electronic properties compared to Gr/Ni(111) and the resegregated carbon atoms which form the Ni_2C drastically modify the electronic environment of the Gr layer. The bias-dependence of Moiré corrugations of Gr on both Ni_2C and Ni(111) indicates a tuning of the doping level in Gr by the material contacting the Gr from below. Moreover, Gr on Ni_2C proves not to protect the Ni_2C underlayer from oxidation, which is probably due to Ni_2C-introduced surface defects (either structurally or electronically) which could act as quantum traps for adsorbed oxygen. Mn deposition on the Gr/Ni_2C surface demonstrates a 2D growth mode in the sub ML range. The spectroscopic contrast indicates a distinct electronic difference between the metal and Gr covered areas, which might also contain spin-polarized information this experiment is not able to exclude.

In the future, except for the unique electronic properties of Gr/Ni_2C/Ni(111), studies on the spintronic properties for this system and other 3*d* metals on Gr may also attract great interest because at the symmetry-broken interface, magnetic materials can display single-handed or homochiral spin structures which arise from spin-orbit scattering of electrons in an inversion-asymmetry-broken crystal field [50–52,55].

7 Conclusion

In this thesis, low dimensional epitaxial Mn films were deposited onto different substrates, such as Co/Cu(001), Cu(001), Ni(111), and Gr/Ni_2C/Ni(111). Using surface-sensitive techniques, the structural, electronic, and magnetic properties of these Mn films have been investigated under UHV conditions.

The Sp-STM technique facilitates studying the spectroscopic contrast of the e-fct Mn surface on Co/Cu(001) on different lengthscales. The differential conductance is different for each thickness of the Mn layer up to 6 ML. This thickness-dependent large-scale spectroscopy contrast between successive Mn-layer thicknesses becomes weaker for increasing Mn thickness and proves to be mainly of electronic origin. Co segregation is likely the origin of the layer-dependent electronic properties. However, an uncompensated layered AFM spin component cannot be ruled out. On the atomic scale, there exists a geometric superstructure with a (12×2) periodicity in two types of mutually orthogonal domains on the Mn surface. The simultaneously observed differential conductance maps reveal a noncollinearity of the Mn surface spin structure at room temperature. Simple models of Mn surface spin structures can simulate the experimental data and present possible spin configurations of the atomic-scale AFM spin structure. Co segregation may also influence the size of the reconstructed domains. The spin structure of Mn is attributed to competing AFM exchange interactions in the frustrated and reconstructed Mn layer. The large-scale layerwise contrast is interpreted to be independent of the contrast from the atomic-scale spin structure. These two types of spectroscopy contrast on different scales are related to the lateral resolution of the image and tip-sample distances. Additionally, oxygen plays an important role in tuning the layerwise contrast, indicating a modification of Mn LDOS by oxygen, possibly accompanied with a change of the Mn magnetic moment.

On the Cu(001) substrate, room-temperature-deposited Mn films of different thicknesses have been investigated. In the sub-ML thickness range, different phases of surface MnCu alloy have been observed, such as *c*(2×2) (island coverage of 0.2 ML), *p*(2×1) and *p*(1×2) (island coverage of 0.7 ML). When the Mn coverage exceeds 1 ML, the growth mode changes into the layer-plus-island growth and the surface roughness increases. The ordered MnCu surface alloy cannot structurally stabilize the subsequently grown Mn film and Cu atoms might be immiscible with Mn in the thick disordered adlayer, such that a 2D structure can hardly be achieved at room temperature for thick Mn films on Cu(001). In order to obtain a thick 2D-Mn film, an oxidized Cu interface and a nanostructured Co seeding layer have been intentionally established prior to Mn deposition. The oxygen surfactant effect is not favored for Mn deposition on the oxygen-"missing-row"-reconstructed surface, which could be due to a larger binding energy between Mn and O than between Mn and Cu. However, an oxygen-assisted 2D growth of Mn is obvious. Sub-ML nanostructured Co islands can better define the surface roughness and do not introduce surface contamination during and after the deposition, such that a better-defined 2D-grown Mn film is achieved.

On the (111) surface of fcc Ni, Mn has been deposited at three different temperatures, namely, room temperature (300 K), low temperature (200 K), and high temperature (560 K). At room temperature, Mn exhibits a layer-by-layer growth up to 5.3 ML and two phase transitions occur after completion of the first ML and at 4.5 ML thickness. After the first phase transition, no regular lattice can be observed, while after the second phase transition, the layer-by-layer growth starts to transit into layer-plus-island growth. In the layer-by-layer-growth thickness range, the size of Mn islands increases with the layer number. Atomic-resolution imaging of sub-ML Mn/Ni(111) reveals a laterally distorted Mn lattice, while the LEED study suggests a relatively smaller distortion in the Mn wetting layer than in the Mn islands. Disordered interfacial alloying could also exist, leading to the observed diffuse LEED background, but no further evidence for this is found. At low temperature, a 1 ML Mn film exhibits a metastable lattice distortion as schematically shown in Figure 5-4 (c) and the corresponding LEED pattern taken at 180 K illustrates an electron-energy dependence of the superstructure symmetry, varying between three-fold (113 eV) and six-fold (145 eV). Both three- and six-fold superstructures become blurred when increasing the temperature to 300 K, indicating a less distorted lattice at 300 K and a temperature-dependent metastable arrangement of the Mn adlayer prepared at 200 K. The 300-K LEED

pattern of 1 ML Mn/Ni(111) with a stronger diffuse background indicates some disorder at room temperature, either from a small fraction of weak lattice distortion, or a disordered alloy, or a coexistence of both. The (1×1) LEED pattern of the 560-K-grown-ML Mn indicates weak or no lateral lattice distortion, as well as a possibly existing (1×1) interfacial alloy.

On both Ni(111) and Cu(001), a thick Mn film exhibits layer-plus-island-growth at 170 K. Mn/Ni(111) shows a $\left(\sqrt{3}\times\sqrt{3}\right)R30°$ reconstruction, while Mn/Cu(001) does not exhibit any regular crystalline lattice according to the absence of LEED diffraction spots. The $\left(\sqrt{3}\times\sqrt{3}\right)R30°$ reconstruction for thick Mn/Ni(111) exhibits no obvious temperature dependence up to 300 K and a stable lattice structure should be present. The simulated real-space lattice demonstrates no incommensurate lattice distortion in the overlayer, and the stable phase for thick Mn/Ni(111) differs from the metastable lattice of the Mn wetting layer on Ni(111).

Mn deposition on the Gr/Ni_2C surface leads to a 2D growth mode in the sub-ML range. The spectroscopic STS contrast indicates a difference in the electronic structure between the metal and Gr-covered areas, which might also contain spin-polarized information this experiment is not able to exclude.

Besides ultrathin Mn films, the growth of Gr on Ni(111) was studied under different preparation conditions: (1) 800−840 K, 600−1800 L propylene, 4−10 min subsequent annealing at dosing temperature; (2) 900 K, propylene at 1×10^{-5} mbar for 5 min (3000 L), 20 min subsequent annealing at 920 K; (3) 900 K, propylene at 2.5×10^{-6} mbar for 10−20 min (1500−3000 L), no subsequent annealing. Temperature, hydrocarbon gas dosing rate, and dosing time may influence the Gr quality drastically. Because of the strong hybridization between 3*d* nickel and Gr electronic states, the growth cannot be well controlled and wafer-level quality is not easy to achieve for the requirement of industrial applications. A preparation under condition (1) favors the formation of epitaxial (1×1) Gr with strong chemical bonding with the Ni(111) substrate, while under condition (2) and (3), the percentage of rotated Gr is increased, although the epitaxial unrotated Gr still covers most of the surface. Surface carbides are stable at temperatures below 840 K and after the surface is saturated with a carbide layer, the Gr growth is blocked. Nevertheless, allowing long enough annealing time at temperatures above 800 K facilitates the conversion of

carbides into Gr. At 900 K, the carbide cannot cover the surface, instead, carbon firstly diffuses into the bulk and resegregates when Gr nucleation starts on the surface. After the Gr sheet terminates the surface, it depends on the bonding force between Gr and the substrate whether the later-on resegregated carbon will form further structures underneath the Gr layer. Due to the strong chemisorption, carbon-related structures are not favored under the epitaxial Gr/Ni(111). In contrast, the bonding between physisorbed rotated Gr and the nickel surface is much weaker, which facilitates further carbon structure formation. The type of carbon-segregation-formed structure underneath the rotated Gr depends on the bulk carbon concentration: lower concentration leads to Ni_2C and higher concentration will form a second layer of Gr. Focusing on special regions of rotated Gr prepared under condition (2), both Ni_2C and a second Gr layer have been observed underneath the rotated ML Gr. The Gr/Ni_2C areas exhibit quite different electronic properties compared to Gr/Ni(111). The resegregated carbon atoms that form the Ni_2C drastically modify the electronic environment of the Gr layer. The bias dependence of Moiré corrugations of Gr on both Ni_2C and Ni(111) indicates a tuning of the doping level in Gr by the material contacting the Gr from below. Moreover, Gr on Ni_2C prepared under condition (3) proves not to protect the Ni_2C underlayer from oxidation, which is probably due to Ni_2C-introduced surface defects (either structurally or electronically) which could act as quantum traps for adsorbed oxygen.

All in all, low-dimensional quantum films demonstrate unique surface properties which can be influenced by many factors such as the substrate type, intermixing, temperature, adsorbates, interface between the film and substrate, thickness, and so on. To understand these properties related to the surface, STM provides a straightforward way and even allows atomic-level investigations. The spin-polarized functionalization of the scanning probe enables further studies of surface spin configurations of magnetic materials, which is a promising way of interpreting spintronic phenomena on the atomic scale.

Bibliography

[1] Baibich M N, Broto J M, Fert A, Van Dau F N, Petroff F, Etienne P, Creuzet G, Friederich A and Chazelas J 1988 Giant Magnetoresistance of (001)Fe/(001)Cr Magnetic Superlattices *Phys. Rev. Lett.* **61** 2472–5

[2] Binasch G, Grünberg P, Saurenbach F and Zinn W 1989 Enhanced magnetoresistance in layered magnetic structures with antiferromagnetic interlayer exchange *Phys. Rev. B* **39** 4828–30

[3] Meiklejohn W H and Bean C P 1957 New Magnetic Anisotropy *Phys. Rev.* **105** 904–13

[4] Schlenker C and Buder R 1971 Ferromagnetic-antiferromagnetic coupling: NiFe thin films deposited on monocrystalline CoO substrates *Czechoslov. J. Phys. B* **21** 506–9

[5] Lenz K, Zander S and Kuch W 2007 Magnetic Proximity Effects in Antiferromagnet/Ferromagnet Bilayers: The Impact on the Néel Temperature *Phys. Rev. Lett.* **98** 237201

[6] Kuch W, Chelaru L I, Offi F, Wang J, Kotsugi M and Kirschner J 2006 Tuning the magnetic coupling across ultrathin antiferromagnetic films by controlling atomic-scale roughness *Nat. Mater.* **5** 128–33

[7] Slonczewski J C 1989 Conductance and exchange coupling of two ferromagnets separated by a tunneling barrier *Phys. Rev. B* **39** 6995–7002

[8] Berger L 1996 Emission of spin waves by a magnetic multilayer traversed by a current *Phys. Rev. B* **54** 9353–8

[9] Brataas A, Kent A D and Ohno H 2012 Current-induced torques in magnetic materials *Nat. Mater.* **11** 372–81

[10] Heinrich B and Bland J A C 2005 *Ultrathin Magnetic Structures IV - Applications of Nanomagnetism | Springer* (Springer-Verlag Berlin Heidelberg)

[11] Ralph D C, Cui Y-T, Liu L Q, Moriyama T, Wang C and Buhrman R A 2011 Spin-transfer torque in nanoscale magnetic devices *Philos. Trans. R. Soc. Math. Phys. Eng. Sci.* **369** 3617–30

[12] Cui Y-T, Finocchio G, Wang C, Katine J A, Buhrman R A and Ralph D C 2010 Single-Shot Time-Domain Studies of Spin-Torque-Driven Switching in Magnetic Tunnel Junctions *Phys. Rev. Lett.* **104** 097201

[13] Cui Y-T, Sankey J C, Wang C, Thadani K V, Li Z-P, Buhrman R A and Ralph D C 2008 Resonant spin-transfer-driven switching of magnetic devices assisted by microwave current pulses *Phys. Rev. B* **77** 214440

[14] Gomonay E V and Loktev V M 2014 Spintronics of antiferromagnetic systems (Review Article) *Low Temp. Phys.* **40** 17–35

[15] Boehm H P, Clauss A, Fischer G O and Hofmann U 1962 Das Adsorptionsverhalten sehr dünner Kohlenstoff-Folien *Z. Für Anorg. Allg. Chem.* **316** 119–27

[16] Rutherford R B and Dudman R L 2003 Ultra-Thin Flexible Expanded Graphite Heating Element

[17] Evans J W, Thiel P A and Bartelt M C 2006 Morphological evolution during epitaxial thin film growth: Formation of 2D islands and 3D mounds *Surf. Sci. Rep.* **61** 1–128

[18] Venables J A, Spiller G D T and Hanbucken M 1984 Nucleation and growth of thin films *Rep. Prog. Phys.* **47** 399

[19] Lee C, Wei X, Kysar J W and Hone J 2008 Measurement of the Elastic Properties and Intrinsic Strength of Monolayer Graphene *Science* **321** 385–8

[20] Chen J-H, Jang C, Xiao S, Ishigami M and Fuhrer M S 2008 Intrinsic and extrinsic performance limits of graphene devices on SiO2 *Nat. Nanotechnol.* **3** 206–9

[21] Bonaccorso F, Sun Z, Hasan T and Ferrari A C 2010 Graphene photonics and optoelectronics *Nat. Photonics* **4** 611–22

[22] Tombros N, Jozsa C, Popinciuc M, Jonkman H T and van Wees B J 2007 Electronic spin transport and spin precession in single graphene layers at room temperature *Nature* **448** 571–4

[23] Karpan V M, Giovannetti G, Khomyakov P A, Talanana M, Starikov A A, Zwierzycki M, van den Brink J, Brocks G and Kelly P J 2007 Graphite and Graphene as Perfect Spin Filters *Phys. Rev. Lett.* **99** 176602

[24] Giovannetti G, Khomyakov P A, Brocks G, Karpan V M, van den Brink J and Kelly P J 2008 Doping Graphene with Metal Contacts *Phys. Rev. Lett.* **101** 026803

[25] Özyilmaz B, Jarillo-Herrero P, Efetov D and Kim P 2007 Electronic transport in locally gated graphene nanoconstrictions *Appl. Phys. Lett.* **91** 192107

[26] Zheng Y, Ni G-X, Toh C-T, Zeng M-G, Chen S-T, Yao K and Özyilmaz B 2009 Gate-controlled nonvolatile graphene-ferroelectric memory *Appl. Phys. Lett.* **94** 163505

[27] Karpan V M, Khomyakov P A, Starikov A A, Giovannetti G, Zwierzycki M, Talanana M, Brocks G, van den Brink J and Kelly P J 2008 Theoretical prediction of perfect spin filtering at interfaces between close-packed surfaces of Ni or Co and graphite or graphene *Phys. Rev. B* **78** 195419

[28] Lakshmi S, Roche S and Cuniberti G 2009 Spin-valve effect in zigzag graphene nanoribbons by defect engineering *Phys. Rev. B* **80** 193404

[29] Iqbal M Z, Iqbal M W, Lee J H, Kim Y S, Chun S-H and Eom J 2013 Spin valve effect of NiFe/graphene/NiFe junctions *Nano Res.* **6** 373–80

[30] Honda S, Yamamura A, Hiraiwa T, Sato R, Inoue J and Itoh H 2010 Magnetoresistance in ferromagnetic-metal/graphene/ferromagnetic-metal lateral junctions *Phys. Rev. B* **82** 033402

[31] Geim A K and Novoselov K S 2007 The rise of graphene *Nat. Mater.* **6** 183–91

[32] Lüth H 2010 *Solid Surfaces, Interfaces and Thin Films (5th Edition)* (Springer Berlin Heidelberg)

[33] Elinson M I, Volkov V A, Lutskij V N and Pinsker T N 1972 Quantum size effect and perspectives of its practical application *Thin Solid Films* **12** 383–97

[34] Krishnan R M and Meyer III F O 1974 Quantum size effect in thin films *Thin Solid Films* **23** 7–13

[35] Zhang B, Wu C-B and Kuch W 2014 Tailoring interlayer coupling and coercivity in Co/Mn/Co trilayers by controlling the interface roughness *J. Appl. Phys.* **115** 233915

[36] Cooper D R, D'Anjou B, Ghattamaneni N, Harack B, Hilke M, Horth A, Majlis N, Massicotte M, Vandsburger L, Whiteway E and Yu V 2012 Experimental Review of Graphene *Int. Sch. Res. Not.* **2012** e501686

[37] Nagashima A, Tejima N and Oshima C 1994 Electronic states of the pristine and alkali-metal-intercalated monolayer graphite/Ni(111) systems *Phys. Rev. B* **50** 17487–95

[38] Shikin A M, Rybkin A G, Marchenko D, Rybkina A A, Scholz M R, Rader O and Varykhalov A 2013 Induced spin–orbit splitting in graphene: the role of atomic number of the intercalated metal and π–d hybridization *New J. Phys.* **15** 013016

[39] Varykhalov A, Sánchez-Barriga J, Shikin A M, Biswas C, Vescovo E, Rybkin A, Marchenko D and Rader O 2008 Electronic and Magnetic Properties of Quasifreestanding Graphene on Ni *Phys. Rev. Lett.* **101** 157601

[40] Hasegawa M, Nishidate K, Hosokai T and Yoshimoto N 2013 Electronic-structure modification of graphene on Ni(111) surface by the intercalation of a noble metal *Phys. Rev. B* **87** 085439

[41] Varykhalov A, Sánchez-Barriga J, Shikin A M, Biswas C, Vescovo E, Rybkin A, Marchenko D and Rader O 2008 Electronic and Magnetic Properties of Quasifreestanding Graphene on Ni *Phys. Rev. Lett.* **101** 157601

[42] Ligato N, Cupolillo A and Caputi L S 2013 Study of the intercalation of graphene on Ni(111) with Cs atoms: Towards the quasi-free graphene *Thin Solid Films* **543** 59–62

[43] Wong S L, Huang H, Wang Y, Cao L, Qi D, Santoso I, Chen W and Wee A T S 2011 Quasi-Free-Standing Epitaxial Graphene on SiC (0001) by Fluorine Intercalation from a Molecular Source *ACS Nano* **5** 7662–8

[44] Grånäs E, Knudsen J, Schröder U A, Gerber T, Busse C, Arman M A, Schulte K, Andersen J N and Michely T 2012 Oxygen Intercalation under Graphene on Ir(111): Energetics, Kinetics, and the Role of Graphene Edges *ACS Nano* **6** 9951–63

[45] Zhao W, Kozlov S M, Höfert O, Gotterbarm K, Lorenz M P A, Viñes F, Papp C, Görling A and Steinrück H-P 2011 Graphene on Ni(111): Coexistence of Different Surface Structures *J. Phys. Chem. Lett.* **2** 759–64

[46] Skomski R 2008 *Simple Models of Magnetism* (OUP Oxford)

[47] Heisenberg W 1928 Zur Theorie des Ferromagnetismus *Z. Für Phys.* **49** 619–36

[48] Bland J A C and Heinrich B 1994 *Ultrathin Magnetic Structures I - An Introduction to the Electronic, Magnetic | Springer* (Springer Berlin Heidelberg)

[49] Néel L 1954 Anisotropie magnétique superficielle et surstructures d'orientation *J. Phys. Radium* **15** 225–39

[50] Moriya T 1960 Anisotropic Superexchange Interaction and Weak Ferromagnetism *Phys. Rev.* **120** 91–8

[51] Dzyaloshinsky I 1958 A thermodynamic theory of "weak" ferromagnetism of antiferromagnetics *J. Phys. Chem. Solids* **4** 241–55

[52] Dzialoshinskii I 1957 Thermodynamic Theory of Weak Ferromagnetism in Antiferromagnetic Substances *Sov. Phys. Jetp-Ussr* **5** 1259–72

[53] Phark S-H, Fischer J A, Corbetta M, Sander D, Nakamura K and Kirschner J 2014 Reduced-dimensionality-induced helimagnetism in iron nanoislands *Nat. Commun.* **5** 5183

[54] Keffer F 1962 Moriya Interaction and the Problem of the Spin Arrangements in β MnS *Phys. Rev.* **126** 896–900

[55] Bode M, Heide M, Bergmann K von, Ferriani P, Heinze S, Bihlmayer G, Kubetzka A, Pietzsch O, Blügel S and Wiesendanger R 2007 Chiral magnetic order at surfaces driven by inversion asymmetry *Nature* **447** 190–3

[56] Ferriani P, von Bergmann K, Vedmedenko E Y, Heinze S, Bode M, Heide M, Bihlmayer G, Blügel S and Wiesendanger R 2008 Atomic-Scale Spin Spiral with a Unique Rotational Sense: Mn Monolayer on W(001) *Phys. Rev. Lett.* **101** 027201

[57] Kuch W, Schäfer R, Fischer P and Hillebrecht F U 2015 *Magnetic Microscopy of Layered Structures* | *Springer* (Springer Berlin Heidelberg)

[58] Freeland J W, Kodama R H, Vedpathak M, Erwin S C, Keavney D J, Winarski R, Ryan P and Rosenberg R A 2004 Induced Ge spin polarization at the Fe/Ge interface *Phys. Rev. B* **70** 033201

[59] Scherz A, Wende H, Poulopoulos P, Lindner J, Baberschke K, Blomquist P, Wäppling R, Wilhelm F and Brookes N B 2001 Induced V and reduced Fe moments at the interface of Fe/V(001) superlattices *Phys. Rev. B* **64** 180407

[60] Samant M G, Stöhr J, Parkin S S P, Held G A, Hermsmeier B D, Herman F, Van Schilfgaarde M, Duda L-C, Mancini D C, Wassdahl N and Nakajima R 1994 Induced spin polarization in Cu spacer layers in Co/Cu multilayers *Phys. Rev. Lett.* **72** 1112–5

[61] Esaki L 1958 New Phenomenon in Narrow Germanium $p-n$ Junctions *Phys. Rev.* **109** 603–4

[62] Esaki L 1974 Long journey into tunneling *Rev. Mod. Phys.* **46** 237–44

[63] Giaever I 1960 Electron Tunneling Between Two Superconductors *Phys. Rev. Lett.* **5** 464–6

[64] Giaever I 1960 Energy Gap in Superconductors Measured by Electron Tunneling *Phys. Rev. Lett.* **5** 147–8

[65] Josephson B D 1962 Possible new effects in superconductive tunnelling *Phys. Lett.* **1** 251–3

[66] Josephson B D 1974 The discovery of tunnelling supercurrents *Rev. Mod. Phys.* **46** 251–4

[67] Young R D 1966 Field Emission Ultramicrometer *Rev. Sci. Instrum.* **37** 275–8

[68] Young R, Ward J and Scire F 1971 Observation of Metal-Vacuum-Metal Tunneling, Field Emission, and the Transition Region *Phys. Rev. Lett.* **27** 922–4

[69] Binnig G, Rohrer H, Gerber C and Weibel E 1982 Tunneling through a controllable vacuum gap *Appl. Phys. Lett.* **40** 178–80

[70] Binnig G, Rohrer H, Gerber C and Weibel E 1982 Surface Studies by Scanning Tunneling Microscopy *Phys. Rev. Lett.* **49** 57–61

[71] Güntherodt H-J and Wiesendanger R 1994 *Scanning Tunneling Microscopy I-General Principles and Applications to Clean and Absorbate-Covered Surfaces* | *Springer* vol 20 (Springer Berlin Heidelberg)

[72] Bardeen J 1961 Tunnelling from a Many-Particle Point of View *Phys. Rev. Lett.* **6** 57–9

[73] Tersoff J and Hamann D 1985 Theory of the scanning tunneling microscope *Phys. Rev. B* **31** 805–13

[74] Tersoff J and Hamann D 1983 Theory and Application for the Scanning Tunneling Microscope *Phys. Rev. Lett.* **50** 1998–2001

[75] Bode M 2003 Spin-polarized scanning tunnelling microscopy *Rep. Prog. Phys.* **66** 523–82

[76] Wulfhekel W and Kirschner J 2007 Spin-Polarized Scanning Tunneling Microscopy of Magnetic Structures and Antiferromagnetic Thin Films *Annu. Rev. Mater. Res.* **37** 69–91

[77] Slonczewski J C 1989 Conductance and exchange coupling of two ferromagnets separated by a tunneling barrier *Phys. Rev. B* **39** 6995–7002

[78] Julliere M 1975 Tunneling between ferromagnetic films *Phys. Lett. A* **54** 225–6

[79] Miyazaki T and Tezuka N 1995 Giant Magnetic Tunneling Effect in Fe/Al2o3/Fe Junction *J. Magn. Magn. Mater.* **139** L231–4

[80] Bode M, Getzlaff M and Wiesendanger R 1998 Spin-Polarized Vacuum Tunneling into the Exchange-Split Surface State of Gd(0001) *Phys. Rev. Lett.* **81** 4256–9

[81] Wulfhekel W and Kirschner J 1999 Spin-polarized scanning tunneling microscopy on ferromagnets *Appl. Phys. Lett.* **75** 1944–6

[82] Seah M P and Dench W A 1979 Quantitative electron spectroscopy of surfaces: A standard data base for electron inelastic mean free paths in solids *Surf. Interface Anal.* **1** 2–11

[83] Wu C-B 2004 *Capping effect on Cu overlayer on Co/FeMn/Cu(001) exchange bias system* Master thesis (Taipei: Department of Physics, National Taiwan University)

[84] Abrudan R M 2007 *Growth, Structure and Magnetic Properties of Single Crystalline Fe/CoO/Ag(001) Bilayers* (Berlin: Freie Universität Berlin, Germany)

[85] http://www.scientaomicron.com/en/products/uhv-stm-1/instrument-concept\line

[86] Schmid A K and Kirschner J 1992 In situ observation of epitaxial growth of Co thin films on Cu(100) *Ultramicroscopy* **42–44, Part 1** 483–9

[87] Cerda J R, Andres P L de, Cebollada A, Miranda R, Navas E, Schuster P, Schneider C M and Kirschner J 1993 Epitaxial growth of cobalt films on Cu(100): a crystallographic LEED determination *J. Phys. Condens. Matter* **5** 2055

[88] Wu C-B, Song J and Kuch W 2012 Spin-polarized scanning tunneling microscopy study of Mn/Co/Cu(001) using a bulk Fe ring probe *Appl. Phys. Lett.* **101** 012404

[89] Kohlhepp J T and de Jonge W J M 2006 Stabilization of Metastable Expanded Face-Centered-Tetragonal Manganese *Phys. Rev. Lett.* **96** 237201

[90] Hafner J and Spišák D 2005 Ab initio investigation of the magnetism of tetragonal Mn: Bulk, surface, ultrathin films, and multilayers *Phys. Rev. B* **72** 144420

[91] Heinze S, Bode M, Kubetzka A, Pietzsch O, Nie X, Blügel S and Wiesendanger R 2000 Real-Space Imaging of Two-Dimensional Antiferromagnetism on the Atomic Scale *Science* **288** 1805–8

[92] Spišák D and Hafner J 2000 Ultrathin Mn films on Cu(111) substrates: Frustrated antiferromagnetic order *Phys. Rev. B* **61** 12728–31

[93] Wang J, Kuch W, Chelaru L I, Offi F and Kotsugi M 2005 Influence of exchange bias coupling on the single-crystalline FeMn ultrathin film *Appl. Phys. Lett.* **86** 122504

[94] Loth S, Baumann S, Lutz C P, Eigler D M and Heinrich A J 2012 Bistability in Atomic-Scale Antiferromagnets *Science* **335** 196–9

[95] Khan M Y, Wu C-B, Erkovan M and Kuch W 2013 Probing antiferromagnetism in NiMn/Ni/(Co)/Cu3Au(001) single-crystalline epitaxial thin films *J. Appl. Phys.* **113** 023913

[96] Hafner J and Hobbs D 2003 Understanding the complex metallic element Mn. II. Geometric frustration in β-Mn, phase stability, and phase transitions *Phys. Rev. B* **68** 014408

[97] Zelený M, Natterer F D, Biedermann A and Hafner J 2010 Ultrathin Mn layers on Rh(001): Investigations using scanning tunneling microscopy and density functional calculations *Phys. Rev. B* **82** 165422

[98] van der Kraan R G P and van Kempen H 1995 Growth of Mn on Cu(100) studied by STM: the c(2 × 2) and pgg(4 × 2) ordered surface alloys *Surf. Sci.* **338** 19–30

[99] Wuttig M, Knight C C, Flores T and Gauthier Y 1993 LEED structure determination of two ordered surface alloys: Cu(100)-c(2 × 2)Mn and Ni(100)-c(2 × 2)Mn *Surf. Sci.* **292** 189–95

[100] Dedkov Y S, Voloshina E N and Fonin M 2006 Observation of surface state on ultrathin fcc γ-Mn(1 1 1) layer *Surf. Sci.* **600** 4328–31

[101] Gao C L, Schlickum U, Wulfhekel W and Kirschner J 2007 Mapping the Surface Spin Structure of Large Unit Cells: Reconstructed Mn Films on Fe(001) *Phys. Rev. Lett.* **98** 107203

[102] Kohlhepp J T 2007 Exchange interaction studies using epitaxially stabilized expanded fct-Mn(0 0 1) *J. Phys. Appl. Phys.* **40** 1300

[103] Wiesendanger R, Shvets I V, Bürgler D, Tarrach G, Güntherodt H J, Coey J M D and Gräser S 1992 Topographic and Magnetic-Sensitive Scanning Tunneling Microscope Study of Magnetite *Science* **255** 583–6

[104] Wiesendanger R 2009 Spin mapping at the nanoscale and atomic scale *Rev. Mod. Phys.* **81** 1495–550

[105] Yoshida Y, Schröder S, Ferriani P, Serrate D, Kubetzka A, von Bergmann K, Heinze S and Wiesendanger R 2012 Conical Spin-Spiral State in an Ultrathin Film Driven by Higher-Order Spin Interactions *Phys. Rev. Lett.* **108** 087205

[106] Hsu P-J, Lu C-I, Chu Y-H, Wang B-Y, Wu C-B, Chen L-J, Wong S-S and Lin M-T 2012 Layered antiferromagnetic spin structures of expanded face-centered-tetragonal Mn(001) as an origin of exchange bias coupling to the magnetic Co layer *Phys. Rev. B* **85** 174434

[107] Kohlhepp J T, Wieldraaijer H and de Jonge W J M 2006 Exchange anisotropy as a probe of antiferromagnetism in expanded face-centered-tetragonal Mn(001) layers *Appl. Phys. Lett.* **89** 032507–032507 – 3

[108] Kohlhepp J T, Wieldraaijer H and de Jonge W J M 2007 Onset of Magnetic Interface Exchange Interactions in Epitaxially Grown Mn/Co(001) *J. Mater. Res.* **22** 569–72

[109] O'Brien W L and Tonner B P 1994 Surface-enhanced magnetic moment and ferromagnetic ordering of Mn ultrathin films on fcc Co(001) *Phys. Rev. B* **50** 2963–9

[110] Noguera A, Bouarab S, Mokrani A, Demangeat C and Dreyssé H 1996 Very thin Mn films on fcc Co(001) *J. Magn. Magn. Mater.* **156** 21–2

[111] Yonamoto Y, Yokoyama T, Amemiya K, Matsumura D and Ohta T 2001 Magnetism of an ultrathin Mn film on Co(100) and the effect of oxidation studied by x-ray magnetic circular dichroism *Phys. Rev. B* **63** 214406

[112] Wang B, You L, Ren P, Yin X, Peng Y, Xia B, Wang L, Yu X, Mui Poh S, Yang P, Yuan G, Chen L, Rusydi A and Wang J 2013 Oxygen-driven anisotropic transport in ultra-thin manganite films *Nat. Commun.* **4**

[113] Wuttig M, Gauthier Y and Blügel S 1993 Magnetically driven buckling and stability of ordered surface alloys: Cu(100)c(2×2)Mn *Phys. Rev. Lett.* **70** 3619–22

[114] Dittschar A, Kuch W, Zharnikov M and Schneider C M 2000 Interrelation of morphology, structure, and magnetism in FexCo1−x/Cu(1 0 0) epitaxial alloy films *J. Magn. Magn. Mater.* **212** 307–22

[115] Müller S, Bayer P, Reischl C, Heinz K, Feldmann B, Zillgen H and Wuttig M 1995 Structural Instability of Ferromagnetic fcc Fe Films on Cu(100) *Phys. Rev. Lett.* **74** 765–8

[116] Bergmann K von, Kubetzka A, Pietzsch O and Wiesendanger R 2014 Interface-induced chiral domain walls, spin spirals and skyrmions revealed by spin-polarized scanning tunneling microscopy *J. Phys. Condens. Matter* **26** 394002

[117] von Bergmann K, Menzel M, Serrate D, Yoshida Y, Schröder S, Ferriani P, Kubetzka A, Wiesendanger R and Heinze S 2012 Tunneling anisotropic magnetoresistance on the atomic scale *Phys. Rev. B* **86** 134422

[118] Song J, Wu C-B, Zhang B, Xu J and Kuch W 2015 Layer-dependent properties and noncollinear spin structure of epitaxial antiferromagnetic Mn films on Co/Cu(001) *Phys. Rev. B* **91** 214406

[119] Müller S, Bayer P, Reischl C, Heinz K, Feldmann B, Zillgen H and Wuttig M 1995 Structural Instability of Ferromagnetic fcc Fe Films on Cu(100) *Phys. Rev. Lett.* **74** 765–8

[120] Huang F, Kief M T, Mankey G J and Willis R F 1994 Magnetism in the few-monolayers limit: A surface magneto-optic Kerr-effect study of the magnetic behavior of ultrathin films of Co, Ni, and Co-Ni alloys on Cu(100) and Cu(111) *Phys. Rev. B* **49** 3962–71

[121] Gallego S, Soria F and Muñoz M C 2003 Two-dimensional effects at the Fermi level of the c(2×2)-MnCu/Cu(0 0 1) surface alloy *Surf. Sci.* **524** 164–72

[122] Park Y, Adenwalla S, Felcher G P and Bader S D 1995 Superparamagnetic relaxation of Fe deposited on MgO(001) *Phys. Rev. B* **52** 12779–83

[123] Bovensiepen U, Poulopoulos P, Platow W, Farle M and Baberschke K 1999 Sudden jump of the Curie temperature at the coalescence of Co islands on Cu(0 0 1) *J. Magn. Magn. Mater.* **192** L386–90

[124] Allmers T and Donath M 2009 Growth and morphology of thin Fe films on flat and vicinal Au(111): a comparative study *New J. Phys.* **11** 103049

[125] Wuttig M, Feldmann B and Flores T 1995 The correlation between structure and magnetism for ultrathin metal films and surface alloys *Surf. Sci.* **331–333, Part A** 659–72

[126] Flores T, Hansen M and Wuttig M 1992 Structure and growth of Mn on Cu(100) *Surf. Sci.* **279** 251–64

[127] Gauthier Y, Poensgen M and Wuttig M 1994 LEED structure determination of the c(8 × 2)Mn phase on Cu(100) *Surf. Sci.* **303** 36–44

[128] Gallego S, Soria F and Muñoz M C 2003 Two-dimensional effects at the Fermi level of the c(2×2)-MnCu/Cu(0 0 1) surface alloy *Surf. Sci.* **524** 164–72

[129] Tian D, Begley A M and Jona F 1992 New metastable phase of Mn by epitaxy on Cu{111} *Surf. Sci.* **273** L393–8

[130] Wu R and Freeman A J 1995 Predicted c(2×2) buckling reconstruction of monolayer Mn on Fe(001) and its importance to the interfacial magnetic ordering *Phys. Rev. B* **51** 17131–4

[131] Rader O, Mizokawa T, Fujimori A and Kimura A 2001 Structure and electron correlation of Mn on Ni(110) *Phys. Rev. B* **64** 165414

[132] Scarselli M, Dragone L, Sgarlata A, Fanfoni M, Di Castro V and Zanoni R 2003 Mn/Pt(1 1 1) interface investigated at the first stages of formation via AES and STM *Surf. Sci.* **545** L774–8

[133] Bode M, Heinze S, Kubetzka A, Pietzsch O, Hennefarth M, Getzlaff M, Wiesendanger R, Nie X, Bihlmayer G and Blügel S 2002 Structural, electronic, and magnetic properties of a Mn monolayer on W(110) *Phys. Rev. B* **66** 014425

[134] Flores T, Junghans S and Wuttig M 1997 Atomic mechanisms of the formation of an ordered surface alloy: an STM investigation of MnCu(100) *Surf. Sci.* **371** 14–29

[135] Pan W, Popescu R, Meyerheim H L, Sander D, Robach O, Ferrer S, Lin M-T and Kirschner J 2005 Stress and structure of c(2×2) and p2gg(4×2) Mn⁄Cu(001) surface alloys *Phys. Rev. B* **71** 174439

[136] Flores T, Junghans S and Wuttig M 1997 Atomic mechanisms for the diffusion of Mn atoms incorporated in the Cu(100) surface: an STM study *Surf. Sci.* **371** 1–13

[137] Schiller F and Laubschat C 2004 Evidence for magnetic behaviour of the c(2×2)Mn/Cu(0 0 1) and Mn/Au(0 0 1) structures *J. Magn. Magn. Mater.* **272–276, Supplement** E239–40

[138] Blügel S 1996 Magnetically stabilized surface alloys *Appl. Phys. A* **63** 595–604

[139] O'Brien W L and Tonner B P 1995 Magnetic properties of Mn/Cu(001) and Mn/Ni(001) c(2×2) surface alloys *Phys. Rev. B* **51** 617–20

[140] Eder M, Hafner J and Moroni E . 1999 Structure and magnetic properties of thin Mn/Cu(001) and CuMn/Cu(100) films *Surf. Sci.* **423** L244–9

[141] Jr W F E, Jacob I, Rudd J M, Cochran J F and Heinrich B 1990 X-ray photoelectron and Auger electron forward-scattering studies of lattice expansions and contractions in epitaxial films *J. Vac. Sci. Technol. A* **8** 1582–6

[142] Staranski I and Krastanow L 1938 Abhandlungen der Mathematisch-Naturwissenschaftlichen Klasse IIb *Akad. Wiss. Wien* **146** 797–810

[143] Tölkes C, Struck R, David R, Zeppenfeld P and Comsa G 1998 Surfactant-Induced Layer-by-Layer Growth on a Highly Anisotropic Substrate: Co/Cu(110) *Phys. Rev. Lett.* **80** 2877–80

[144] Ling W L, Takeuchi O, Ogletree D F, Qiu Z Q and Salmeron M 2000 STM studies on the growth of monolayers: Co on Cu(110) with one half monolayer of preadsorbed oxygen *Surf. Sci.* **450** 227–41

[145] Nath K G, Haruyama Y and Kinoshita T 2001 Surface superstructure formation, electronic structure modification and magnetic stability of Co films on oxygen-rich Cu(0 0 1): confirmation of oxygen-surfactant effect *Surf. Sci.* **486** 185–93

[146] Sorg C, Ponpandian N, Bernien M, Baberschke K, Wende H and Wu R Q 2006 Induced magnetism of oxygen in surfactant-grown Fe, Co, and Ni monolayers *Phys. Rev. B* **73** 064409

[147] Krüger P, Taguchi M and Meza-Aguilar S 2000 Magnetism of 3d transition-metal monolayers on Cu(111) and Ag(111) *Phys. Rev. B* **61** 15277–83

[148] Wuttig M, Flores T and Knight C C 1993 Structure and growth of Mn on Ni(100) *Phys. Rev. B* **48** 12082–92

[149] Deng-Feng L, Hai-Yan X, Xiao-Tao Z, Hui-Ning D and Fei G 2010 Structural, electronic and magnetic properties of the Mn-Ni(110) c(2x2) surface alloy *Chin. Phys. B* **19** 087102

[150] Dedkov Y S, Voloshina E N and Fonin M 2006 Observation of surface state on ultrathin fcc γ-Mn(1 1 1) layer *Surf. Sci.* **600** 4328–31

[151] Choi B-C, Bode P J and Bland J A C 1998 Formation of a two-dimensional c(2×2) Mn-Co(001) ferromagnetic surface alloy on Cu(001) *Phys. Rev. B* **58** 5166–8

[152] Schneider J, Rosenhahn A and Wandelt K 1999 STM measurements on alloy formation during submonolayer growth of Mn on Cu(111) *Appl. Surf. Sci.* **142** 68–74

[153] Rader O, Mizokawa T, Fujimori A and Kimura A 2001 Structure and electron correlation of Mn on Ni(110) *Phys. Rev. B* **64** 165414

[154] Schieffer P, Hanf M C, Krembel C and Gewinner G 2000 Formation of c(2×2) Mn–Ag superficial bilayer alloys on Ag(001): role of thermally activated surface atomic exchange and ordering *Surf. Sci.* **446** 175–86

[155] Walker T G and Hopster H 1993 Magnetism of Mn layers on Fe(100) *Phys. Rev. B* **48** 3563–6

[156] Rader O, Pampuch C, Gudat W, Carbone A D C and Eberhardt W 1999 Parallel, antiparallel and no magnetic coupling in submonolayer Mn on Fe(110) *EPL Europhys. Lett.* **46** 231

[157] Vang R T, Honkala K, Dahl S, Vestergaard E K, Schnadt J, Lægsgaard E, Clausen B S, Nørskov J K and Besenbacher F 2006 Ethylene dissociation on flat and stepped Ni(1 1 1): A combined STM and DFT study *Surf. Sci.* **600** 66–77

[158] Chambon C, Creuze J, Coati A, Sauvage-Simkin M and Garreau Y 2009 Tilted and nontilted Ag overlayer on a Ni(111) substrate: Structure and energetics *Phys. Rev. B* **79** 125412

[159] Mróz S, Jankowski Z and Nowicki M 2000 Growth and isothermal desorption of ultrathin silver layers on the Ni(111) face at the substrate temperature from 180 to 900 K *Surf. Sci.* **454–456** 702–6

[160] Feinstein L G, Blanc E and Dufayard D 1970 LEED study of the epitaxy of silver on nickel (111) *Surf. Sci.* **19** 269–82

[161] Bauer E 1967 Multiple scattering versus superstructures in low energy electron diffraction *Surf. Sci.* **7** 351–64

[162] http://www.fhi-berlin.mpg.de/KHsoftware/LEEDpat/

[163] Andersen J N, Lundgren E, Nyholm R and Qvarford M 1993 Alkali metal adsorption on Al(111) *Surf. Sci.* **289** 307–34

[164] Dahal A and Batzill M 2014 Graphene–nickel interfaces: a review *Nanoscale* **6** 2548–62

[165] Dedkov Y S, Fonin M and Laubschat C 2008 A possible source of spin-polarized electrons: The inert graphene/Ni(111) system *Appl. Phys. Lett.* **92** 052506

[166] Bianchini F, Patera L L, Peressi M, Africh C and Comelli G 2014 Atomic Scale Identification of Coexisting Graphene Structures on Ni(111) *J. Phys. Chem. Lett.* **5** 467–73

[167] Eizenberg M and Blakely J M 1979 Carbon monolayer phase condensation on Ni(111) *Surf. Sci.* **82** 228–36

[168] Bignardi L, Haarlammert T, Winter C, Montagnese M, van Loosdrecht P H M, Voloshina E, Rudolf P and Zacharias H 2014 Dual character of excited charge carriers in graphene on Ni(111) *Phys. Rev. B* **89** 075405

[169] Generalov A V and Dedkov Y S 2012 EELS study of the epitaxial graphene/Ni(1 1 1) and graphene/Au/Ni(1 1 1) systems *Carbon* **50** 183–91

[170] Lahiri J, Miller T, Adamska L, Oleynik I I and Batzill M 2011 Graphene Growth on Ni(111) by Transformation of a Surface Carbide *Nano Lett.* **11** 518–22

[171] Yu Q, Lian J, Siriponglert S, Li H, Chen Y P and Pei S-S 2008 Graphene segregated on Ni surfaces and transferred to insulators *Appl. Phys. Lett.* **93** 113103

[172] Addou R, Dahal A, Sutter P and Batzill M 2012 Monolayer graphene growth on Ni(111) by low temperature chemical vapor deposition *Appl. Phys. Lett.* **100** 021601

[173] Entani S, Kurahashi M, Sun X and Yamauchi Y 2013 Spin polarization of single-layer graphene epitaxially grown on Ni(1 1 1) thin film *Carbon* **61** 134–9

[174] Gong S J, Li Z Y, Yang Z Q, Gong C, Duan C-G and Chu J H 2011 Spintronic properties of graphene films grown on Ni(111) substrate *J. Appl. Phys.* **110** 043704

[175] Wintterlin J and Bocquet M-L 2009 Graphene on metal surfaces *Surf. Sci.* **603** 1841–52

[176] Wofford J M, Starodub E, Walter A L, Nie S, Bostwick A, Bartelt N C, Thürmer K, Rotenberg E, McCarty K F and Dubon O D 2012 Extraordinary epitaxial alignment of graphene islands on Au(111) *New J. Phys.* **14** 053008

[177] Voloshina E N, Fertitta E, Garhofer A, Mittendorfer F, Fonin M, Thissen A and Dedkov Y S 2013 Electronic structure and imaging contrast of graphene moire on metals *Sci. Rep.* **3**

[178] Stojanov P, Voloshina E, Dedkov Y, Schmitt S, Haenke T and Thissen A 2014 Graphene on Rh(111): Combined DFT, STM, and NC-AFM Studies *Procedia Eng.* **93** 8–16

[179] Sutter P W, Flege J-I and Sutter E A 2008 Epitaxial graphene on ruthenium *Nat. Mater.* **7** 406–11

[180] Nie S, Wu W, Xing S, Yu Q, Bao J, Pei S and McCarty K F 2012 Growth from below: bilayer graphene on copper by chemical vapor deposition *New J. Phys.* **14** 093028

[181] Addou R, Dahal A, Sutter P and Batzill M 2012 Monolayer graphene growth on Ni(111) by low temperature chemical vapor deposition *Appl. Phys. Lett.* **100** 021601

[182] Patera L L, Africh C, Weatherup R S, Blume R, Bhardwaj S, Castellarin-Cudia C, Knop-Gericke A, Schloegl R, Comelli G, Hofmann S and Cepek C 2013 In Situ Observations of the Atomistic Mechanisms of Ni Catalyzed Low Temperature Graphene Growth *ACS Nano* **7** 7901–12

[183] Ma T, Ren W, Zhang X, Liu Z, Gao Y, Yin L-C, Ma X-L, Ding F and Cheng H-M 2013 Edge-controlled growth and kinetics of single-crystal graphene domains by chemical vapor deposition *Proc. Natl. Acad. Sci.* **110** 20386–91

[184] Zhang Y, Gao T, Xie S, Dai B, Fu L, Gao Y, Chen Y, Liu M and Liu Z 2012 Different growth behaviors of ambient pressure chemical vapor deposition graphene on Ni(111) and Ni films: A scanning tunneling microscopy study *Nano Res.* **5** 402–11

[185] Jiao M, Qian H, Page A, Li K, Wang Y, Wu Z, Irle S and Morokuma K 2014 Graphene Nucleation from Amorphous Nickel Carbides: QM/MD Studies on the Role of Subsurface Carbon Density *J. Phys. Chem. C* **118** 11078–84

[186] Lahiri J, Miller T S, Ross A J, Adamska L, Oleynik I I and Batzill M 2011 Graphene growth and stability at nickel surfaces *New J. Phys.* **13** 025001

[187] Kelly B 1972 Thermal-Expansion Coefficient of Graphite Parallel to Basal Planes *Carbon* **10** 429 – &

[188] Nix F C and MacNair D 1941 The Thermal Expansion of Pure Metals: Copper, Gold, Aluminum, Nickel, and Iron *Phys. Rev.* **60** 597–605

[189] Varykhalov A, Marchenko D, Sánchez-Barriga J, Scholz M R, Verberck B, Trauzettel B, Wehling T O, Carbone C and Rader O 2012 Intact Dirac Cones at Broken Sublattice Symmetry: Photoemission Study of Graphene on Ni and Co *Phys. Rev. X* **2** 041017

[190] Shibuta Y and Elliott J A 2012 Interaction between graphene and nickel(1 1 1) surfaces with commensurate and incommensurate orientational relationships *Chem. Phys. Lett.* **538** 112–7

[191] Dedkov Y S and Fonin M 2010 Electronic and magnetic properties of the graphene–ferromagnet interface *New J. Phys.* **12** 125004

[192] Abtew T, Shih B-C, Banerjee S and Zhang P 2013 Graphene–ferromagnet interfaces: hybridization, magnetization and charge transfer *Nanoscale* **5** 1902–9

[193] Dedkov Y S, Shikin A M, Adamchuk V K, Molodtsov S L, Laubschat C, Bauer A and Kaindl G 2001 Intercalation of copper underneath a monolayer of graphite on Ni(111) *Phys. Rev. B* **64** 035405

[194] Dedkov Y S, Fonin M, Rüdiger U and Laubschat C 2008 Rashba Effect in the Graphene/Ni(111) System *Phys. Rev. Lett.* **100** 107602

[195] Pong W-T and Durkan C 2005 A review and outlook for an anomaly of scanning tunnelling microscopy (STM): superlattices on graphite *J. Phys. Appl. Phys.* **38** R329

[196] Osing J and Shvets I V 1998 Bulk defects in graphite observed with a scanning tunnelling microscope *Surf. Sci.* **417** 145–50

[197] Garbarz J, Lacaze E, Faivre G, Gauthier S and Schott M 1992 Dislocation networks in graphite: a scanning tunnelling microscopy study *Philos. Mag. A* **65** 853–61

[198] Albrecht T R, Mizes H A, Nogami J, Park S and Quate C F 1988 Observation of tilt boundaries in graphite by scanning tunneling microscopy and associated multiple tip effects *Appl. Phys. Lett.* **52** 362–4

[199] Kuwabara M, Clarke D R and Smith D A 1990 Anomalous superperiodicity in scanning tunneling microscope images of graphite *Appl. Phys. Lett.* **56** 2396–8

[200] Buckley J E, Wragg J L, White H W, Bruckdorfer A and Worcester D L 1991 Large-scale periodic features associated with surface boundaries in scanning tunneling microscope images of graphite *J. Vac. Sci. Technol. B* **9** 1079–82

[201] Kuwabara M, Clarke D R and Smith D A 1990 Anomalous superperiodicity in scanning tunneling microscope images of graphite *Appl. Phys. Lett.* **56** 2396–8

[202] Liu C Y, Chang H and Bard A J 1991 Large scale hexagonal domainlike structures superimposed on the atomic corrugation of a graphite surface observed by scanning tunneling microscopy *Langmuir* **7** 1138–42

[203] Green T and Weigle J 1948 Theorie Du Moire *Helvetica Phys. Acta* **21** 217–217

[204] Oster G 1968 Moire Patterns in Physics *Endeavour* **27** 60–4

[205] Murata Y, Petrova V, Kappes B B, Ebnonnasir A, Petrov I, Xie Y-H, Ciobanu C V and Kodambaka S 2010 Moiré Superstructures of Graphene on Faceted Nickel Islands *ACS Nano* **4** 6509–14

[206] Jacobson P, Stöger B, Garhofer A, Parkinson G S, Schmid M, Caudillo R, Mittendorfer F, Redinger J and Diebold U 2012 Nickel Carbide as a Source of Grain Rotation in Epitaxial Graphene *ACS Nano* **6** 3564–72

[207] Zhao R, Zhang Y, Gao T, Gao Y, Liu N, Fu L and Liu Z 2011 Scanning tunneling microscope observations of non-AB stacking of graphene on Ni films *Nano Res.* **4** 712–21

[208] Amidror I 2003 Unified approach for the explanation of stochastic and periodic Moire´s *J. Electron. Imaging* **12** 669–81

[209] Bernal J D 1924 The Structure of Graphite *Proc. R. Soc. Lond. Math. Phys. Eng. Sci.* **106** 749–73

[210] Olsen T, Yan J, Mortensen J J and Thygesen K S 2011 Dispersive and Covalent Interactions between Graphene and Metal Surfaces from the Random Phase Approximation *Phys. Rev. Lett.* **107** 156401

[211] Iwasaki T, Zakharov A A, Eelbo T, Waśniowska M, Wiesendanger R, Smet J H and Starke U 2014 Formation and structural analysis of twisted bilayer graphene on Ni(111) thin films *Surf. Sci.* **625** 44–9

[212] Dahal A, Addou R, Sutter P and Batzill M 2012 Graphene monolayer rotation on Ni(111) facilitates bilayer graphene growth *Appl. Phys. Lett.* **100** 241602

[213] Klink C, Stensgaard I, Besenbacher F and Lægsgaard E 1995 An STM study of carbon-induced structures on Ni(111): evidence for a carbidic-phase clock reconstruction *Surf. Sci.* **342** 250–60

[214] Jiang J-W, Wang B-S and Rabczuk T 2013 Why twisting angles are diverse in graphene Moiré patterns? *J. Appl. Phys.* **113** 194304

[215] Latil S, Meunier V and Henrard L 2007 Massless fermions in multilayer graphitic systems with misoriented layers: \textit{Ab initio} calculations and experimental fingerprints *Phys. Rev. B* **76** 201402

[216] Partoens B and Peeters F M 2006 From graphene to graphite: Electronic structure around the K point *Phys. Rev. B* **74** 075404

[217] Gibson J S, Uddin J, Cundari T R, Bodiford N K and Wilson A K 2010 First-principle study of structure and stability of nickel carbides *J. Phys. Condens. Matter* **22** 445503

[218] Rong Z Y and Kuiper P 1993 Electronic effects in scanning tunneling microscopy: Moiré pattern on a graphite surface *Phys. Rev. B* **48** 17427–31

[219] Bernhardt T M, Kaiser B and Rademann K 1998 Formation of superperiodic patterns on highly oriented pyrolytic graphite by manipulation of nanosized graphite sheets with the STM tip *Surf. Sci.* **408** 86–94

[220] Xhie J, Sattler K, Ge M and Venkateswaran N 1993 Giant and supergiant lattices on graphite *Phys. Rev. B* **47** 15835–41

[221] Biró L P and Lambin P 2013 Grain boundaries in graphene grown by chemical vapor deposition *New J. Phys.* **15** 035024

[222] Sun H-L, Shen Q-T, Jia J-F, Zhang Q-Z and Xue Q-K 2003 Scanning tunneling microscopy study of superlattice domain boundaries on graphite surface *Surf. Sci.* **542** 94–100

[223] Oden P I, Thundat T, Nagahara L A, Lindsay S M, Adams G B and Sankey O F 1991 Superperiodic features observed on graphite under solution with scanning tunneling microscopy *Surf. Sci.* **254** L454–9

[224] Batzill M 2012 The surface science of graphene: Metal interfaces, CVD synthesis, nanoribbons, chemical modifications, and defects *Surf. Sci. Rep.* **67** 83–115

[225] Morell E S, Vargas P, Häberle P, Hevia S A and Chico L 2015 Edge states of moiré structures in graphite *Phys. Rev. B* **91** 035441

[226] Biró L P and Lambin P 2013 Grain boundaries in graphene grown by chemical vapor deposition *New J. Phys.* **15** 035024

[227] Červenka J and Flipse C F J 2009 Structural and electronic properties of grain boundaries in graphite: Planes of periodically distributed point defects *Phys. Rev. B* **79** 195429

[228] Warner J H, Rümmeli M H, Gemming T, Büchner B and Briggs G A D 2009 Direct Imaging of Rotational Stacking Faults in Few Layer Graphene *Nano Lett.* **9** 102–6

[229] Vázquez de Parga A L, Calleja F, Borca B, Passeggi M C G, Hinarejos J J, Guinea F and Miranda R 2008 Periodically Rippled Graphene: Growth and Spatially Resolved Electronic Structure *Phys. Rev. Lett.* **100** 056807

[230] Borca B, Barja S, Garnica M, Hinarejos J J, Vázquez de Parga A L, Miranda R and Guinea F 2010 Periodically modulated geometric and electronic structure of graphene on Ru(0 0 0 1) *Semicond. Sci. Technol.* **25** 034001

[231] Jiang D, Du M-H and Dai S 2009 First principles study of the graphene/Ru(0001) interface *J. Chem. Phys.* **130** 074705

[232] Wang B, Bocquet M-L, Marchini S, Günther S and Wintterlin J 2008 Chemical origin of a graphene moiré overlayer on Ru(0001) *Phys. Chem. Chem. Phys.* **10** 3530–4

[233] Feng W, Lei S, Li Q and Zhao A 2011 Periodically Modulated Electronic Properties of the Epitaxial Monolayer Graphene on Ru(0001) *J. Phys. Chem. C* **115** 24858–64

[234] Grüneis A and Vyalikh D V 2008 Tunable hybridization between electronic states of graphene and a metal surface *Phys. Rev. B* **77** 193401

[235] Generalov A V, Voloshina E N and Dedkov Y S 2013 Structural and electronic properties of graphene-based junctions for spin-filtering: The graphene/Al/Ni(1 1 1) intercalation-like system *Appl. Surf. Sci.* **267** 8–11

[236] Sánchez-Barriga J, Varykhalov A, Scholz M R, Rader O, Marchenko D, Rybkin A, Shikin A M and Vescovo E 2010 Chemical vapour deposition of graphene on Ni(111) and Co(0001) and intercalation with Au to study Dirac-cone formation and Rashba splitting *Diam. Relat. Mater.* **19** 734–41

[237] Kang M H, Jung S C and Park J W 2010 Density functional study of the Au-intercalated graphene/Ni(111) surface *Phys. Rev. B* **82** 085409

[238] Generalov A V and Dedkov Y S 2012 EELS study of the epitaxial graphene/Ni(1 1 1) and graphene/Au/Ni(1 1 1) systems *Carbon* **50** 183–91

[239] Bertoni G, Calmels L, Altibelli A and Serin V 2005 First-principles calculation of the electronic structure and EELS spectra at the graphene/Ni(111) interface *Phys. Rev. B* **71** 075402

[240] Shikin A M, Prudnikova G V, Adamchuk V K, Moresco F and Rieder K-H 2000 Surface intercalation of gold underneath a graphite monolayer on Ni(111) studied by angle-resolved photoemission and high-resolution electron-energy-loss spectroscopy *Phys. Rev. B* **62** 13202–8

[241] Grüneis A 2013 Synthesis and electronic properties of chemically functionalized graphene on metal surfaces *J. Phys. Condens. Matter* **25** 043001

[242] Kwon S G and Kang M H 2012 Effects of Cu intercalation on the graphene/Ni(111) surface: Density-functional calculations *J. Korean Phys. Soc.* **61** 589–93

[243] Anon Electronic and Magnetic Properties of the Graphene/Eu/Ni(111) Hybrid System : Zeitschrift für Naturforschung A

[244] Sun X, Pratt A and Yamauchi Y 2010 First-principles study of the structural and magnetic properties of graphene on a Fe/Ni(1 1 1) surface *J. Phys. Appl. Phys.* **43** 385002

[245] Kelty S P and Lieber C M 1989 Scanning tunneling microscopy investigations of the electronic structure of potassium-graphite intercalation compounds *J. Phys. Chem.* **93** 5983–5

[246] Grüneis A and Vyalikh D V 2008 Tunable hybridization between electronic states of graphene and a metal surface *Phys. Rev. B* **77** 193401

[247] Park Y S, Park J H, Hwang H N, Laishram T S, Kim K S, Kang M H and Hwang C C 2014 Quasi-Free-Standing Graphene Monolayer on a Ni Crystal through Spontaneous Na Intercalation *Phys. Rev. X* **4** 031016

[248] Adamska L, Addou R, Batzill M and Oleynik I I 2012 Atomic and electronic structure of graphene/Sn-Ni(111) and graphene/Sn-Cu(111) surface alloy interfaces *Appl. Phys. Lett.* **101** 051602

[249] Addou R, Dahal A and Batzill M 2012 Graphene on ordered Ni-alloy surfaces formed by metal (Sn, Al) intercalation between graphene/Ni(111) *Surf. Sci.* **606** 1108–12

[250] Zhang W-B and Chen C 2015 Tuning metal–graphene interaction by non-metal intercalation: a case study of the graphene/oxygen/Ni (1 1 1) system *J. Phys. Appl. Phys.* **48** 015308

[251] Grüneis A 2013 Synthesis and electronic properties of chemically functionalized graphene on metal surfaces *J. Phys. Condens. Matter* **25** 043001

[252] Riedl C, Coletti C, Iwasaki T, Zakharov A A and Starke U 2009 Quasi-Free-Standing Epitaxial Graphene on SiC Obtained by Hydrogen Intercalation *Phys. Rev. Lett.* **103** 246804

[253] Zhang H, Fu Q, Cui Y, Tan D and Bao X 2009 Growth Mechanism of Graphene on Ru(0001) and O2 Adsorption on the Graphene/Ru(0001) Surface *J. Phys. Chem. C* **113** 8296–301

[254] Larciprete R, Ulstrup S, Lacovig P, Dalmiglio M, Bianchi M, Mazzola F, Hornekær L, Orlando F, Baraldi A, Hofmann P and Lizzit S 2012 Oxygen Switching of the Epitaxial Graphene–Metal Interaction *ACS Nano* **6** 9551–8

[255] Sutter P, Sadowski J T and Sutter E A 2010 Chemistry under Cover: Tuning Metal−Graphene Interaction by Reactive Intercalation *J. Am. Chem. Soc.* **132** 8175–9

[256] Mehmood F, Pachter R, Lu W and Boeckl J J 2013 Adsorption and Diffusion of Oxygen on Single-Layer Graphene with Topological Defects *J. Phys. Chem. C* **117** 10366–74

[257] Schlickum U, Wulfhekel W and Kirschner J 2003 Spin-polarized scanning tunneling microscope for imaging the in-plane magnetization *Appl. Phys. Lett.* **83** 2016–8

[258] Wulfhekel W and Gao C L 2010 Investigation of non-collinear spin states with scanning tunneling microscopy *J. Phys. Condens. Matter* **22** 084021

[259] Zhao P, Kim S, Chen X, Einarsson E, Wang M, Song Y, Wang H, Chiashi S, Xiang R and Maruyama S 2014 Equilibrium Chemical Vapor Deposition Growth of Bernal-Stacked Bilayer Graphene *ACS Nano* **8** 11631–8

List of abbreviations

0D	zero dimension/dimensionality/dimensional
2D	two dimension/dimensionality/dimensional
3D	three dimension/dimensionality/dimensional
Å	Angstrom
AC	alternating current
AFM	antiferromagnet/antiferromagnetic
Ag	silver
Ar	argon
ARPES	angle-resolved photoemission spectroscopy
BL	bilayer
CCD	charge-coupled device
CD	compact disc
Co	cobalt
Cr	chromium
Cu	copper
CVD	chemical vapor deposition
DC	direct current
DFT	density functional theory
DMI	Dzyaloshinskii-Moriya interaction
e-fct	expanded face-centered tetragonal
eV	electronvolt

fcc	face-centered cubic
Fe	iron
FFT	fast Fourier transform
FM	ferromagnet/ferromagnetic
GMR	giant magnetoresistance
Gr	graphene
hcp	hexagonal close packing
IMFP	inelastic mean free path
ITO	indium tin oxide
keV	kiloelectronvolt
kHz	kilohertz
L	Langmuir
LDOS	local density of states
LEED	low-energy electron diffraction
MΩ	megaohm
MBE	molecular beam epitaxy
MEED	medium-energy electron diffraction
min	minute
ML	monolayer
Mn	manganese
MnO	manganese oxide
MOKE	magneto-optica Kerr effect
MoS_2	molybdenum disulfide
MRAM	magnetoresistive random-access memory
mV	millivolt
nA	nanoampere

NASA	National Aeronautics and Space Administration
$NbSe_2$	niobium selenide
Ni	nickel
Ni_2C	nickel carbide
nm	nanometer
nS	nanosiemens
O	oxygen
℃	degree Celsius
Oe	oersted
pm	picometer
RHEED	reflection high-energy electron diffraction
Ru	ruthenium
$SmCo_5$	samarium cobalt
Sp-STM	spin-polarized scanning tunneling microscope/microscopy
Sp-STS	spin-polarized scanning tunneling spectroscopy
STM	scanning tunneling microscope/microscopy
STS	scanning tunneling spectroscopy
STT	spin transfer torque
T	tesla
TaS_2	tantalum sulfide
$TaSe_2$	tantalum diselenide
TMR	tunnel magnetoresistance
TSP	titanium sublimation pump
UHV	ultrahigh vacuum
V	volt
WKB	Wentzel-Kramers-Brillouin

WSe_2	tungsten diselenide
XAS	x-ray absorption spectroscopy
XMCD	x-ray magnetic circular dichroism
XMLD	x-ray magnetic linear dichroism
Y	Yttrium

List of publications

Jiaming Song, Chii-Bin Wu, Bin Zhang, Jianli Xu, Wolfgang Kuch. *Layer-dependent properties and non-collinear spin structure of epitaxial antiferromagnetic Mn films on Co/Cu(001)*. Physical Review B **91** 214406 (2015)

Chii-Bin Wu, Jiaming Song, Wolfgang Kuch. *Spin-polarized scanning tunneling microscopy study of Mn/Co/Cu(001) using a bulk Fe ring probe*. Applied Physics Letter **101** 012404 (2012)

Jiaming Song, Matthias Bernien, Chii-Bin Wu, Wolfgang Kuch. *Electronic-property modification of rotated graphene on Ni(111) by nickel carbide intercalation*. Manuscript in preparation (2015)

List of conference contributions

Jiaming Song, Chii-Bin Wu, Bin Zhang, Wolfgang Kuch. Talk: *Exploring the spectroscopic contrast in spin-polarized scanning tunneling microscopy of the antiferromagnetic e-fct Mn surface: From sub-micrometer to Ångstrom length scales*. DPG Spring Meeting, 15.–20.03.2015, Berlin, Germany

Jiaming Song, Chii-Bin Wu, Wolfgang Kuch. Poster: *Non-collinear spin texture of fct-Mn on Co/Cu(001) at room temperature*. Scanning Probe Microscopy DIPC Week: A Tribute to Heinrich Rohrer, 05.–12.09.2014, San Sebastian, Spain

Jiaming Song, Chii-Bin Wu, Wolfgang Kuch. Talk: *STM and LEED Studies on the Interfacial Alloying and Oxygen Surfactant Effects of Mn on Cu(001)*. DPG Spring Meeting, 30.03.–04.04.2014, Dresden, Germany

Jiaming Song, Chii-Bin Wu, Wolfgang Kuch. Poster: *STM study of oxygen adsorbate-induced dI/dV contrast tuning in fct-Mn films*. 5th International Workshop on Advanced Scanning Probe Microscopy Techniques, 24.–25.02.2014, Karlsruhe, Germany

Jiaming Song, Chii-Bin Wu, Wolfgang Kuch. Poster: *Optimization of the differential conductance contrast in spinpolarized room-temperature scanning tunneling microscopy of e-fct Mn on Co/Cu(001)*. DPG Spring Meeting, 10.–15.03.2013, Regensburg, Germany

Jiaming Song, Chii-Bin Wu, Wolfgang Kuch. Poster: *Layerwise Antiferromagnetic Spin Structure of Mn/Co/Cu(001) Probed by Spin-polarized Scanning Tunneling Microscopy with Bulk Fe Ring Probe*. The 21th International Colloquium on Magnetic Films and Surfaces, 24.–28.09.2012, Shanghai, China

Chii-Bin Wu, Jiaming Song, Wolfgang Kuch. Talk: *The thickness-dependent spin structure of Mn on Co/Cu(001) studied by spin-polarized scanning tunneling microscopy with bulk Fe ring probes*. International Conference on Nanoscience + Technology, 23.–27.07.2012, Paris, France

Chii-Bin Wu, Jiaming Song, Wolfgang Kuch. Talk: *The spin structure of Mn on Co/Cu(001) studied by spin polarized STM with bulk Cr tips and bulk Fe ring probes*. DPG Spring Meeting, 25.–30.03.2012, Berlin, Germany

Acknowledgments

Foremost, I would like express my sincere gratitude to **Prof. Dr. Wolfgang Kuch**, my PhD advisor, for his continuous support during my four years time pursuing a PhD degree at Freie Universität Berlin. I have benefited so much from discussions with him. From him, I have learned how to manage time efficiently, how to do science objectively, and how to balance life and work. His patience and kindness for guiding each of the PhD students in the group impressed me a lot. I appreciate his meticulous review of my PhD thesis and paper. The insightful comments and suggestions inspired me to think deeper and to write better.

Besides my advisor, I also appreciate **Prof. Dr. Leonhard Grill** for being my second advisor and offering me the opportunity for discussing with him about my thesis.

My sincere thanks also go to **Prof. Dr. Chii-Bin Wu**, whom I have learned Sp-STM when he was a post-doc in AG Kuch. As a beginner in the lab, I was lucky to be able to work with him together for the first 15 months of my PhD period. He taught me how to make lab notes briefly and efficiently, how to troubleshoot problems of lab equipments reasonably, how to carry out experiments independently, and how to analyze data scientifically. He gave me lots of benifical suggestions and was always ready to help. I think I own him a lot.

I have to thank **Dr. Matthias Bernien** for his warm-hearted help whenever asked. He could always give good suggestions and help to solve problems effectively. He helped me a lot in my graphene project. I want to thank **Dr. Bin Zhang** for helping set up the electromagnet of the MOKE system. His spirit of never giving up in a difficult situation impressed me a lot. I will treasure memories about the time when we helped each other in Berlin. I would say thanks to **Dr. Yin-Ming Chang** for working together in AG Kuch. His optimism and fortitude are so admirable. I will miss the delicious food cooked by this Taiwanese. I have to thank **Yasser Shokr** for helping set up an electric motor on the manipulator of the chamber, which saved a lot of strength in the following experiments.

I want to thank **Dr. Julia Kurde**, **Dr. Babara Sandow**, **Dr. Victoria L. Mazalova**, **Dr. Christain Felix Hermanns, Dr. Alex Krüger**, **Fabian Nickel**, **Oliver Sandig**, **Dr. Yaqoob Khan, Lucas Arruda, Dr. Andrew Britton,** and **Lalminthang Kipgen** for sharing the happy time in AG Kuch. I thank **Risalat Khan, Dr. Jianli Xu**, and **Till Kolster**

for doing experiments with me. The time we worked together in the STM lab are precious memories in my mind.

I appreciate **Ms. Marion Badow** for helping me with reimbursement of conferences, ordering products, and sharing happinesses of the life. I also thank **Uwe Lipowski** for the technical support. His smart design of the MOKE optical stage helped me a lot.

I want to express my sincere thanks to all the members of AG Kuch.

I appreciate beneficial discussions with **Prof. Dr. Katharina J. Franke** before submitting the manuscript of my first paper. I thank **Dr. Kun Zhang** at Universität Göttingen for sending me interesting papers about the ion beam sputtering. It was really interesting meeting each other at DPG conference every year. I thank **Dr. Marco Smerieri** at IMEM-CNR, U.O.S. Genova for sending me the graphene papers.

I also want to thank **Michael Kregielski** and **Detlef Müller** at Feinwerktechnik, **Martin Rust** and **Wolfgang Schimank** at Fachabteilung Elektronik, and **Cihan Dede** at Materiallager for their help during my PhD project.

Thanks to all my friends in Berlin!

I appreciate financial support from China Scholarship Council for my four years' stay in Berlin.

I want to express the gratitude to **my parents**, for their constant support, full understanding, and endless love. I appreciate **my mother-in-law** for treating me as her own daughter. I thank **Jialiang Song** for growing up together with me and giving me a happy childhood. Thank **Huan Zhao** for sharing her happiness together with me.

Finally, I would like to thank my dearest husband **Dr. Xin Zhao**. Thanks for being the one indispensable in my life.